**The Thesis Committee for Michelle Ann Fox**
**Certifies that this is the approved version of the following thesis:**

# Probing Topographical Influences on Biofilm Formation using Dynamic-Mask Multiphoton Lithography

**APPROVED BY**
**SUPERVISING COMMITTEE:**

**Supervisor:**

Jason B. Shear

Marvin Whiteley

# Probing Topographical Influences on Biofilm Formation using Dynamic-Mask Multiphoton Lithography

**by**

**Michelle Ann Fox, B.S.; B.Music; M.Music**

**Thesis**

Presented to the Faculty of the Graduate School of

The University of Texas at Austin

in Partial Fulfillment

of the Requirements

for the Degree of

**Master of Arts**

**The University of Texas at Austin**

**May 2011**

# Dedication

To my parents, John G. Fox, Gerry J. Gogel, and the late Kimberly A. Gogel

# Acknowledgements

I wish to sincerely thank Jason Shear, my advisor, for his encouragement, guidance, and support. I would like to thank Marvin Whiteley for his support and for imparting some of his knowledge of microbiology. I warmly thank the analytical faculty and enjoyed their conversations. I thank all former members of the Shear group, whose tremendous creativity and innovation paved the way for me to engage in very exciting research. Specifically, I owe many thanks to Rex Nielson and Bryan Kaehr whose dynamic research efforts largely drew me down to Texas. Rex Nielson also helped me get started with research in this group, and I thank him for that. I thank Samira Moorjani and Stephanie Seidlits, former group members, for their helpful conversations and friendship. I owe much gratitude to Eric Ritschdorff, Eric Spivey, Jodi Connell, Todd Hoppe, Maryam Ali, and Derek Hernandez, current group members, for their friendships and all their help. I wish to sincerely acknowledge Eric Spivey for his atomic force microscopy data, which is included in Chapter 3. I owe many thanks to Jodi Connell for taking such diligent care of the maintenance and alignment of the back Zeiss rig. I have enjoyed getting to know the newest group members, Mike Robinson and Sarah Stuart. I owe special thanks to Aimee Wessel for patiently teaching me microbiology culturing techniques. She is also warmly acknowledged for her role in some of the experiments in the early part of Chapter 2. I thank Matt Ramsey for his helpful conversations; I especially thank him for suggesting the experiment with fluorescent beads in Chapter 3. I also thank other members of the Whiteley lab for their help these past few years. I thank the chemistry department for a recruitment fellowship. Finally, I wish to thank my dear family and friends in Iowa, Texas, and throughout the United States. You have supported

and loved me through both happy and difficult times, and I could not have completed this work without you.

May 6, 2011

# Abstract

## Probing Topographical Influences on Biofilm Formation using Dynamic-Mask Multiphoton Lithography

Michelle Ann Fox, M. A.

The University of Texas at Austin, 2011

Supervisor: Jason B. Shear

It has only been within recent decades that the complexity and heterogeneity of the biofilm mode of bacterial existence has been widely appreciated. Biofilms have persisted for billions of years as social communities of cells aggregated and attached on surfaces, and today they are both necessary and harmful within the human body and our surrounding environment. They show extremely high antibiotic resistance relative to planktonic cells and are sources of persistent infections. Biofilms are also the most common cause of failure for indwelling biomedical devices and implants. As a result, research efforts and commercial developments are focusing on creating better biomaterials that prevent bacterial attachment to surfaces leading to biofilm formation. While chemical methods to combat bacterial infections have been around for over a century in the form of antimicrobials, relatively little is known about how topographical

methods can prevent bacterial attachment to surfaces. The reason for this is that micro- and nano-scale fabrication technologies (which are needed to produce topographies on size scales that might be expected to influence bacterial attachment) are fairly recent developments.

In this thesis work, microscale topographies were developed for probing and influencing bacterial attachment to surfaces using dynamic-mask multiphoton lithography. Multiphoton lithography is an inherently three-dimensional fabrication technique. When combined with the dynamic-mask-based technology developed in the Shear laboratory, it allows for rapid prototyping of 3D structures of arbitrary complexity with submicron resolution in the radial dimension.

A variety of topographical approaches for influencing bacterial attachment of *Pseudomonas aeruginosa* cells were explored within this work. *P. aeruginosa* was selected as a model organism for biofilm formation and because it is commonly isolated from infections associated with biomedical implant devices. Topographical approaches included the design of topographies based on microscale surfaces of naturally-antifouling leaves and mathematical functions, pillars, and surfaces containing various sizes and geometries of holes. Challenges relating to an imaging artifact caused by light scattering induced by the surfaces shed light on issues associated with assessing bacterial attachment levels on microscale topographical surfaces. Finally, future directions for this work are presented with ideas that extend into the nanoscale regime.

# Table of Contents

# List of Figures

# Chapter 1: Approaches for Inhibiting Biofilm Formation

## 1.1 INTRODUCTION

While the complex and heterogeneous nature of bacteria attached to surfaces has only been realized within recent decades, surface-associated bacteria were first observed by van Leeuwenhoek in the 17th century. Van Leeuwenhoek published sketches and descriptions of aggregates of cocci cells (spherical-shaped bacteria) extracted from the "scurf" of his teeth [1].* When the era of modern microbiology began in the 19th century, major advances were made not by the study of surface-associated (sessile) bacteria, but by the study of planktonic (free-swimming or drifting) cultures. Important advances included methodologies for identifying specific microbes as pathogens for disease and developing preventative measures, such as vaccines [2, 3, 4].

As the field of microbiology advanced with studies of planktonic bacteria, the characteristics and importance of sessile bacteria were eloquently described by Heinrici in 1933 [5]. After submersing a glass slide in his laboratory aquarium for one week, Heinrici was surprised to discover that, in addition to algae, a layer of bacteria with various microcolonies and morphologies was attached firmly to the glass. By considering his observations and also noting that unpolluted freshwaters contained the majority of microbial mass on the bottom mud surfaces, Heinrici was led to the following conclusion:

> "It is quite evident that for the most part the water bacteria are not free-floating organisms, but grow upon submerged surfaces; they are of the *benthos* rather than the *plancton*."

* Van Leeuwenhoek was also the first to observe planktonic bacteria, which he described as "animalcules" in 1677.

Today, the surface-associated bacteria observed by Heinrici are called "biofilms" -- persistent and ubiquitous communities of bacteria in the natural environment of ancient earth, the natural and built environments of modern civilization, and even in the human body itself [6].

The defining characteristics of surface biofilms are the association of cell aggregates to a surface and high resistance to antibiotics [6-8]. Biofilm cells frequently secrete and encase themselves within a protective matrix known as extracellular polymeric substance (EPS), which consists of nucleic acids (including DNA and RNA), proteins, and polysaccharides [9]. Far from being a simple clump of aggregated cells, biofilms are complex and highly-organized communities, with structural and chemical heterogeneities revealed by modern imaging techniques [10-12]. For example, the use of confocal laser scanning microscopy has shown that biofilms consist of microcolonies separated by water channels for nutrient and waste exchange [10]. Heterogeneities in gene expression and metabolic activity throughout biofilms allow subpopulations of cells to survive in adverse environmental conditions, such as antibiotic dosing [12].

Sessile, biofilm cell populations are persistent sources of infection, requiring 10 to 1000 times the dosage of antibiotics needed to kill planktonic cells [7]. They are associated with the majority of nosocomial infections, including those caused by indwelling biomedical devices and implants [7, 13]. In response to device-related infections, there has been a large body of research and development on chemical methods, particularly antimicrobials, for preventing bacterial colonization of surfaces. However, antimicrobial-selection of resistant bacterial strains, such as methicillin-resistant *Staphylococcus aureus*, remains an ever-present danger. Further challenges related to chemical method approaches include potential human toxicities/allergies, the

need for broad-spectrum effectiveness, and the *in vivo* delivery of therapeutic dosage levels.

An alternative and potentially complementary approach for inhibiting bacterial colonization of surfaces is the use of topography. The research conducted for this thesis focused on developing and testing topographies for inhibiting and influencing bacterial attachment and biofilm formation. Topographies were fabricated with dynamic-mask multiphoton lithography [14], a technology developed in the Shear group that allows for rapid prototyping of high-resolution features on size-scales similar to bacteria. Essential to this work was the collaboration of Marvin Whiteley, a microbiologist and expert on *Pseudomonas aeruginosa*, and his group.

*P. aeruginosa*, an opportunistic pathogen, forms biofilms that are especially devastating for patients with cystic fibrosis, in whom chronic and lethal infections occur in the alveoli of the lungs [15, 16]. *P. aeruginosa* was selected for testing with the topographies developed in this work, since it has been studied extensively as a model organism for biofilm formation of Gram-negative bacteria. The lifecycle of a *P. aeruginosa* biofilm initiates with the attachment of individual cells to a surface, followed by microcolony formation, development into a mature biofilm, and dispersal of mature biofilm cells back into a planktonic mode of existence [17]. The final step of biofilm formation is an important mechanism in the spread of infections [6]. Disruption at any point in the lifecycle of a biofilm is likely to be advantageous in the design of antifouling surfaces. However, the most powerful disruption would prevent biofilm formation at the stage of initial attachment of cells to a surface.

## 1.2 Existing Methods for Inhibiting Biofilm Formation

### 1.2.1 Chemical Methods

Chemical methods for preventing bacterial attachment to implants and other biomedical devices have spurred a vast body of research and commercial development over the past several decades. Research efforts have focused on a wide variety of antimicrobial agents and strategies for using these agents to prevent device-related infections (DRIs). Antimicrobial agents for preventing DRIs include antibiotics, silver ions, quaternary ammonium ions, cationic peptides, nitric oxide, antibodies, and naturally-derived plant extracts [18, 19]. Various strategies exist for employing antimicrobial agents in biomedical devices, including immobilization to polymer surfaces, polymerization of biocidal monomers, and impregnation of polymers for antimicrobial-release [20].

Nonfouling surface coatings, such as polyethylene glycol and zwitterionic polymers, are alternative or complementary approaches to the use of antimicrobials [21]. In addition to reducing microbial attachment, they possess general antifouling properties towards proteins and other biomolecules. However, they are not always stable *in vivo* and may still allow implant surfaces to be conditioned with a film of proteins and small organic molecules from plasma. The conditioning film can then prevent interactions between the antifouling surface and microbes [19]. For this reason, a common approach is to load antimicrobials into either the bulk material or surface coating of the device for controlled-release [19, 22, 23].

One of the earliest examples, developed in the 1970s, of controlled-drug release for preventing bacterial infection was a PMMA (polymethyl methacrylate) bone cement, loaded with antibiotics, used for joint replacements. Following joint replacement

surgery, the antibiotic was released slowly from the PMMA matrix to combat bacterial infections at the site of the implant [22].

Delivering antibiotics from the implant device, rather than systemically, allows for local administration of therapeutic dosage levels [23]. Another important functionality of controlled-release biomedical devices involves the release kinetics [19, 22, 23]. Bacteria are introduced to devices either exogenously (e.g., from clothing, the atmosphere, or patient's skin) or endogenously from organisms circulating in the bloodstream [22, 24]. Consequently, different types of infections occur throughout the lifetime of a biomedical device.† Therapeutic release of antimicrobials is thus required beyond the initial post-implantation/insertion period to protect against later-stage infections. The release profile of an antimicrobial drug from a polymer depends on several factors, including the chemical properties of the drug and polymer and the distribution of the drug in the polymer matrix [19]. A wide variety of biocompatible polymers and also biodegradable polymers, which deliver potentially larger antimicrobial doses, have been explored for both immobilization and controlled-release strategies [20, 22].

Antibiotics are common antimicrobial agents for controlled-release devices, but they tend to be specific against a small number of bacterial strains and to produce antimicrobial resistance. To prevent antimicrobial resistance, combinations of antibiotics are often used, such as minocycline/rifampcin (MR) catheters. Antiseptics are alternatives to antibiotics that are generally believed to be less susceptible to causing antimicrobial resistance. Chlorhexidine/silver sulfadiazine (CSS) catheters are

† One example relates to prosthetic-valve endocarditis, a condition caused by infected heart valves. Early-stage infections (less than 60 days post-implantation) are generally caused by *Staphylococcus epidermidis*, *Staphylococcus aureus*, and *Gram-negative bacteria*. Late-stage infections (occurring greater than 60 days post-implantation) are generally caused by *Streptococci spp*. and *S. epidermidis*. Early-stage infections are also associated with higher mortality rates [25].

combination antiseptic devices that are frequently compared to MR catheters in clinical trials. Both have been shown to reduce catheter-related bloodstream infections relative to uncoated catheters. [23, 26]

CSS catheters are an example of a device with silver ions as antimicrobial agents. The antimicrobial properties of silver have been utilized since antiquity for storage containers and for the treatment of diseases, wounds, and burns [18, 27]. Today, silver in various forms – as metallic silver, silver salts, silver powder, and silver nanoparticles -- is the subject of considerable research and commercial development for catheters, wound dressings and bandages, and other biomedical products and devices [27-29].

The first silver coatings tested were metallic silver and silver salts, which were effective *in vitro* but much less effective *in vivo*, producing poor clinical results [27, 28]. Reasons cited for the ineffectiveness of metallic silver and silver salt coatings included masking of the coatings by biomolecules from plasma, poor *in vivo* durability, and low levels of silver ion release. For silver to work as an antimicrobial it must be ionized as $Ag^+$, rather than in its elemental form. Subsequent work has focused on maximizing silver ion release by impregnation of polymers with silver powder (microscale particles) and silver nanoparticles [27-29]. As an active releasing agent, silver ions work by disrupting bacterial cell membranes through coordination with thiol, hydroxyl, and amine functional groups in proteins and other biomolecules [19, 29]. The greatest advantages of silver ions include its broad-spectrum effectiveness and low susceptibility for selection of resistant strains.‡ While silver ions in low doses are generally considered to be nontoxic to human cells, there is growing concern over the safety of silver nanoparticles, which have been shown to be toxic to several mammalian cell lines [27].

‡ Silver-resistant strains have been isolated clinically (*Enterobacteriaceae spp*.) and also from silver mines (*Pseudomonas stutzeri*) [30].

Like silver ions, quaternary ammonium compounds (QACs) are broad-spectrum antimicrobials that work by disruption of bacterial cell membranes [18, 31, 32]. Possible mechanisms for membrane disruption include ion exchange between positively-charged QACs and structurally-important cations within the cell membrane for Gram-negative bacteria and membrane insertion of the QACs across the cell wall for disruption of the cytoplasmic membrane for Gram-positive bacteria [31, 32]. QACs have been used as disinfectants for several decades and attracted considerable interest as coatings for biomedical devices. However, QACs are known to select bacterially-resistant strains [33].

Another class of cationic antimicrobials is cationic peptides, which are produced as part of the innate immune response by all organisms. They are about 10 to 50 amino acids in length and fold into amphiphilic structures that are ideal for interacting with bacterial cell membranes. Cationic peptides interact electrostatically with anionic cell surfaces – the lipopolysaccharide outer membrane for Gram-negative bacteria and anionic acids on the cell walls of Gram-positive bacteria. After crossing the outer membrane or cell wall, the peptide is inserted into the cytoplasmic membrane, causing cell death by either membrane disruption or internal targeting of cytoplasmic substituents. Cationic peptides can be effective against Gram-positive and Gram-negative bacteria, fungi, and viruses. [34, 35]

Nitric oxide is another antimicrobial agent that is part of the innate immune response. In response to infection, nitric oxide is produced by macrophages and causes oxidative stress in bacteria, leading to membrane disruption and damage of DNA, proteins, and other biomolecules [19]. Marxer et al. developed a sol-gel with tunable release profiles of nitric oxide [36].

Naturally-derived plant extracts, such as furanones, are also being explored for coating implant devices. Unlike the antimicrobials discussed so far, furanones are non-bactericidal, which makes them less prone to selecting resistant strains. Derived from Australian marine algae, furanones prevent biofilm formation by inhibiting bacterial cell communication behaviors, such as quorum sensing and swarming motility. [18]

Over the past several decades a wide variety of chemical methods have been developed for reducing bacterial infections associated with implant devices. Antibiotics have been the most widely used antimicrobials in the past century, but they tend to select resistant strains and to be effective against only a narrow spectrum of microbes. Alternatively, broad-spectrum antimicrobials are being explored to combat antimicrobial resistance. The design of antimicrobial biomedical devices is a complex research problem involving considerations such as antimicrobial development, polymer research, manufacturing methods and costs, and potential toxicities to humans. With the wide range of biomedical devices and implants in use today, it may be that different types of devices require different chemical methods for treatment depending on the function and location of the device in the human body. Ultimately, the development of new biomaterials is a dynamic process with many interrelated factors to be considered beyond bacterial infection, such as the promotion of healthy tissue development around the device.

### 1.2.2 Topographical Methods

In contrast to chemical methods, there has been comparatively little development of topographical methods for preventing bacterial colonization of surfaces. This is not surprising considering the relatively short time span in which surface-associated bacteria have been studied compared to planktonic cultures. Furthermore, the study of planktonic

cultures led to the development of antibiotics as early as the late 19$^{th}$ century, while the engineering of micro- and nano-scale surfaces (i.e., on a size scale that might be expected to influence bacterial attachment) has been enabled only recently by technological developments.

Further challenges involve developing relevant assays for assessing bacterial attachment levels to topographical surfaces. For example, scanning electron microscopy (SEM) is an excellent method for obtaining high-resolution images, but it requires sample fixation and dehydration steps that may alter the numbers of bacteria attached to surfaces. Consequently, SEM may be best used as a complementary approach to methods that assess bacterial attachment under hydrated conditions in which bacteria are alive and actively attached to surfaces. Even with hydrated conditions, it is challenging to define what constitutes bacterial attachment to surfaces. Additionally, there are numerous variables related to the bacterial environment that influence attachment levels, such as nutrient conditions and availability, temperature, oxygen levels, and flow conditions (i.e., static versus flowing aqueous environments).

Most studies exploring the influence of topography on bacterial attachment have examined the effects of surface roughness, rather than the effects of defined and regular topographical features. In 1994, Tebbs et al. conducted one of the earliest examples of a study on bacterial attachment in response to surface roughness [37]. They measured and calculated Ra values, which are surface roughness measures based on mean deviations from the mean profile line, of five commercial polyurethane catheters. They found that *Staphylococcus epidermidis* (spherical Gram-positive cells with 1-μm diameters) adherence was greater on catheters with Ra values from 1.3 to 6.4 μm relative to Ra values of 0.2 to 0.9 μm.

In other studies, stainless steel and polymer surfaces were purposefully roughened by methods such as grinding and polishing to study bacterial attachment on surfaces roughened to size scales similar to bacteria [38, 39]. Flint et al. found that stainless steel surfaces roughened to Ra values between 0.5 and 3.3 μm did not produce differential attachment levels of streptococci cells (spherical Gram-positive cells about 1-μm in diameter) [38]. By contrast, Taylor et al. reported significantly higher levels of *P. aeruginosa* and *S. epidermidis* attachment on PMMA (polymethyl methacrylate) roughened to 1.2 μm relative to Ra values of 0.04 and 1.9 to 7.9 μm [39]. (There were no significant differences in attachment levels between 0.04 and 1.9 to 7.9 μm).

While the previous studies examined bacterial attachment to surfaces roughened on the micro-scale, other studies have examined the influence of surfaces roughened on the nano-scale [40-42]. In a recent study, Mitik-Dineva et al. examined attachment of *E. coli*, *P. aeruginosa*, and *Staphylococcus aureus* to glass surfaces with Rz values of 5 and 12 nm, where Rz is the mean displacement from the mean profile line of the five highest peaks and valleys along a measurement profile. [40]. The authors found a two-fold reduction in attachment for *E. coli* and *P. aeruginosa* and significant reduction for *S. aureus* attachment on glass with roughness of 12 nm relative to 5 nm. Additionally, cell dimensions of *E. coli* and *P. aeruginosa* were larger on glass with a surface roughness of 5 nm relative to 12 nm.

In another intriguing study, Rizzello et al. imaged *E. coli* cells attached to nanostructured gold (Ra = 30 to 100 nm) with atomic force microscopy [41]. In response to the nanostructured surfaces, cells lost type 1 fimbriae. Type 1 fimbriae are appendages (3 to 10 nm in diameter and up to several microns long) made of proteins that are densely distributed on bacterial cell membranes for attachment to surfaces, including host cells

[43]. The authors further reported differential genetic profiles and protein expression patterns related to fimbrial production, stress processes, and defense mechanisms.

Nanostructured titanium surfaces had significant effects on the attachment levels of *S. aureus*, *S. epidermidis*, and *P. aeruginosa* [42]. Relative to conventional titanium, nanoroughened titanium with features around 100 nm caused decreased attachment. Interestingly, other nanotextured surfaces increased bacterial attachment.

Compared to studies of the effects of surface roughness, few studies exist examining the effects of regular, defined topographical surfaces on bacterial attachment. Diaz et al. used atomic force microscopy to image *P. fluorescens* attached to gold surfaces with 0.12-µm-deep and 0.75-µm-wide trenches separated by 0.55-µm-wide rows [44]. They showed that cells aligned preferentially in trenches and that cell lengths were shorter on a surface with trenches relative to a flat gold surface. They also noted that longer cells attached across trenches and that cells had lower densities of aggregation on the surface with trenches relative to the control surface. Hochbaum et al. used arrays of posts (~ 300 nm in diameter) to induce specific attachment orientations and patterns of *P. aeruginosa* cells [45]

Only one commercial product, Sharklet AF™ [46], has been developed using topographical features for the specific purpose of preventing bacterial colonization. Sharklet AF™ is made of PDMS (polydimethylsiloxane) and consists of 2-µm-wide rectangular features with lengths of 4, 8, 12, and 16 µm arranged in a diamond-like pattern inspired by the naturally-antifouling properties of Galapagos sharkskin [47].§ Feature heights are 3-µm-tall and spaced apart by 2 µm. In a study on *S. aureus* attachment by electron microscopy, the authors reported that biofilms were inhibited

§ It should be noted that Galapagos sharkskin has diamond-like features that span 200 µm in length with ridges separated by 50 µm, a size-scale that is much larger than Sharklet AF™.

from growing on Sharklet AF™ for 21 days [47]. The authors hypothesized that the feature resolution was not high enough to inhibit attachment of individual organisms but that the overall design was effective in reducing biofilm formation.

To date, studies of topographical influences on bacterial attachment are very limited. Those that do exist have not probed topographies in a systematic way (e.g., by varying feature sizes and spaces between features). This has largely been due to limitations of existing fabrication methods, in which rapid-prototyping of topographical surfaces has not been possible. By contrast, dynamic-mask-directed multiphoton lithography, a technology developed in the Shear group, enables rapid-prototyping of three-dimensional surfaces of arbitrary geometry and complexity with submicrometer resolution [14]. Surfaces can be fabricated from a variety of proteins and polymers [48, 49], which can be functionalized to produce surfaces of different chemistries [50]. While beyond the scope of this work, multiphoton lithography could be used to design surfaces that integrate chemical and topographical methods for inhibiting biofilm formation.

## 1.3 MULTIPHOTON FABRICATION

### 1.3.1 Multiphoton Excitation

Beginning in the early 1990s, the advent of pulsed femtosecond lasers has enabled diverse research applications involving multiphoton excitation [51]. Applications have included fluorescence imaging deep into biological tissue, deep-UV imaging of native chromophores in biological molecules [52], separations of transient photochemical products [53], and high-resolution photolithography [54]. Advantages of multiphoton excitation (MPE) over single-photon excitation (1PE) include the use of relatively low-energy photons and three-dimensional confinement of absorption to subfemtoliter voxels with high numerical aperture objectives [55].

In MPE, two or more photons with combined energies that equal an electronic energy gap of a molecule are absorbed nearly simultaneously. This process requires a molecule to undergo a nonresonant transition to a transient virtual state followed by absorption of a second photon within a short time scale. The time-energy form of the Heisenberg uncertainty principle, $\Delta E \approx h/\Delta t$, describes how two or more photons can be in resonance over a superposition of molecular states for very short time scales [52, 56], ~ 1 fs for visible light. This means that high laser peak intensities (photons $cm^{-2}$ $s^{-1}$) of appropriate wavelengths will increase the probability that a molecule will absorb two or more photons within a femtosecond timescale.

To further understand why high peak intensities enhance multiphoton excitation, it is useful to make an analogy between MPE and a chemical reaction as in the following equation [55]:

$$M + n(h\nu) \leftrightarrow M^* \qquad 1.1$$

where M represents the ground-state molecule, n equals the number of photons absorbed by M, $h\nu$ is the photon energy, and M* is the excited-state molecule. The rate of formation of the excited-state molecule can then be expressed as:

$$d[M^*]/dt = k[h\nu][M] = \sigma_n I^n[M] \qquad 1.2$$

where k is the forward rate constant, $\sigma_n$ is the absorption cross-section, and I is the instantaneous intensity of the excitation light. The units of $\sigma_n$ ($cm^{2n}(s/photon)^{n-1}$) depend on the number of photons absorbed. Two-photon cross-sections are often given in units of 1 Göppert-Mayer (where 1 GM = $10^{-50}$ $cm^4$ s $photon^{-1}$), in honor of Maria Göppert-Mayer, who proposed the theory of molecular two-photon absorption in her dissertation published in 1931 [52, 57].

Equation 1.2 shows that there is a nonlinear dependence for MPE on the instantaneous intensity of the excitation light, as opposed to a linear dependence for 1PE.

For a laser beam focused into a sample, the total number of excitation events will be the same for all planes perpendicular to the optical axis in 1PE. In MPE, however, the total number of excitation events will increase towards the beam waist, where intensities are highest. This allows MPE (and thus fluorescence emission, photochemistry, photolithography, etc.) to be localized within a sample to a three-dimensional voxel.

While it is possible to use continuous-output lasers for multiphoton excitation, especially for molecules with large 2PE and 3PE cross-sections, extremely high average powers are needed to achieve excitation rates similar to those obtained with pulsed lasers [52]. The use of pulsed lasers with high repetition rates allows excitation light to be focused not only spatially, with high-numerical aperture (NA) optics, but also temporally. The combined effects of spatial and temporal localization result in high instantaneous intensities achieved with relatively low average power outputs. For example, by focusing a 10-mW beam output through high-NA optics, the average intensity at the focal point increases to ~ $10^{7}$ J $s^{-1}$ $cm^{-2}$, as calculated by dividing the power over a beam area of ~ $10^{-9}$ $cm^{2}$ [51]. By using a pulsed laser source, such as a titanium sapphire laser with an 80 MHz repetition rate and 100-fs pulse widths, the instantaneous intensity at the beam waist increases to ~ $10^{12}$ J $s^{-1}$ $cm^{-2}$.

By focusing excitation light both spatially and temporally, MPE rates increase by many orders of magnitude, thus making what is a low-probability event under other excitation conditions a powerful method for 3D-localization. It is the 3D-localization of MPE events that makes multiphoton lithography an inherently 3D photofabrication technique.

### 1.3.2 Introduction to Multiphoton Lithography

Multiphoton lithography is a direct-write fabrication technique for producing three-dimensional microstructures with resolutions under 100 nm in some instances [49, 59]. Since fabrication is localized in three dimensions to subfemtoliter voxels, multiphoton lithography is an inherently 3D fabrication process that requires scanning a focused laser beam within a fabrication solution to promote photopolymerization of polymers or photocrosslinking of proteins. Applications include microelectromechanical systems (MEMS), photonic crystals, and biologically-compatible structures [49, 59]. A wide range of polymers and proteins can be used for fabrication with multiphoton lithography. Photocrosslinking of protein-residue side chains, such as tyrosine, has been shown to occur by direct free radical and oxygen-dependent processes [60].

Within the Shear group, multiphoton lithography has been used as a versatile technology for creating biologically-relevant structures. In the area of microbiology, smart microarchitectural designs of protein microchambers were used to confine small populations of *E. coli* cells [54, 58] and to generate microfluidic currents driven by directed bacterial motility [60]. Connell et al. grew up clonal populations of *P. aeruginosa* in picoliter-sized microchambers to probe intriguing questions about bacterial group behaviors and antibiotic-resistance [62]. The Shear group has also used protein structures to guide neuronal cell growth [63, 64]. For example, peptide-modified protein structures fabricated in 3D hydrogels directed growth of neuronal cells along a helical pathway in work that has applications in tissue regeneration [64]. In the area of biosensors, catalytically-active structures can be fabricated by a variety of approaches -- through direct crosslinking of enzymes or functionalization of surfaces by using biotin/avidin binding or electrostatic interactions of proteins with different isoelectric points [65-67].

While the biological applications of multiphoton lithography have been diverse within the Shear group, one overarching theme has been to produce three-dimensional micro-environments for studying cellular behavior. In this thesis work, dynamic-mask-based multiphoton lithography was used to study bacterial attachment behaviors in response to defined topographical surfaces.

### 1.3.3 Dynamic-Mask-Based Multiphoton Lithography

The first mask-directed multiphoton lithography technique developed in the Shear group was based on transmission masks [54]. In this approach, a masking object (e.g., a housefly or a printed transparency film) was placed in a focal plane conjugate to the specimen plane, between a confocal scan box and a high NA objective. A collimated laser beam from a titanium sapphire laser was directed into the confocal scan box to create a rectangular raster scanning pattern that was focused onto the transmission film object, most often a negative image on transparency paper. Excitation light was only passed through transparent regions of the mask and focused by the microscope objective into the fabrication solution -- a concentrated aqueous solution of protein and photosensitizer. Crosslinking of protein would occur only in those regions where light was allowed to pass through the transparency film.

A limitation of transparency masks was that they were impractical for fabrication of structures with arbitrary complexity along the optical axis, since alignment of sequential masks was a painstaking process. This limitation was overcome by the development of dynamic-mask-based multiphoton lithography [14]. In dynamic-mask-based multiphoton lithography, a digital micromirror device (DMD) creates reflectance patterns in response to the graphics output from a personal computer. The DMD is an array of aluminum mirrors (800 × 600), with each mirror (16 μm)$^2$, and individually-

controlled by electronics. The mirrors can tilt ±10°; for black-and-white masks, mirrors corresponding to the white regions of a mask tilt so that light is reflected into the fabrication solution, while those corresponding to the black regions tilt so that light is reflected into a beam block. By coordinating the presentation of electronic masks with a motorized z-stepper for turning the fine focus knob of a microscope, 3D structures of arbitrary complexity are fabricated plane-by-plane from coverglass up through the fabrication solution (Figure 1.1).

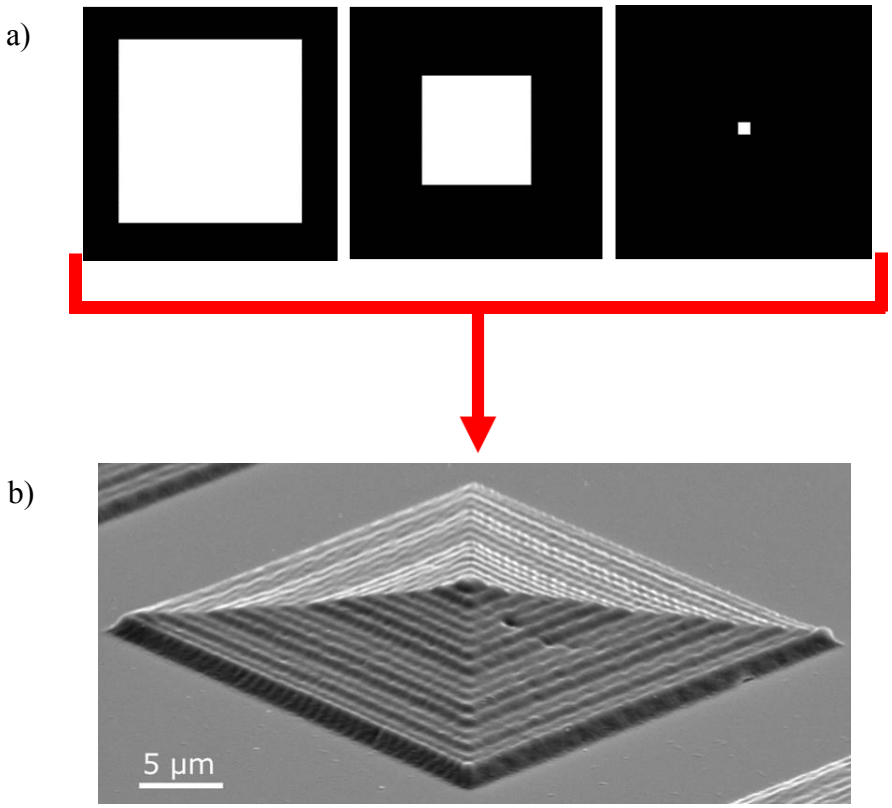


Figure 1.1: DMD-based multiphoton lithography. A few of the binary masks (a) used to fabricate the simple DMD multiphoton lithography structure shown in the scanning electron microscopy (SEM) image (b). The structure was fabricated using bovine serum albumin (BSA) and methylene blue photosensitizer.

### 1.3.4 Experimental Setup

#### *1.3.4.1 Fabrication Methods*

A basic schematic for the experimental setup of microstructure fabrication with DMD multiphoton lithography is shown in Figure 1.2 [62]. For the experiments in this thesis work, a mode-locked titanium sapphire (Ti:S) laser beam (Spectra-Physics, Tsunami) tuned to ~ 740 nm was aligned into a confocal scan box (Biorad, MRC 600). Galvano mirrors housed within the scan box caused the laser beam to scan in a rectangular raster pattern at a rate of ~ 500 lines in 1 to 3 seconds (depending on the setting). A series of lenses focused the raster-scanning beam onto a DMD (Texas Instruments, 0.55SVGA) housed within a partially-dismantled projector (Benq, MP510) with its electronics still intact. The binary output of masks from a personal computer controlled the electronics associated with the individually-addressable mirrors, which created a reflectance pattern. After the DMD, light reflected down the optical path was directed and collimated with lenses into an inverted microscope (Zeiss Axiovert 135) where it overfilled the back aperture of an objective (Zeiss Fluar 100×/1.3 NA oil-immersion). Average laser powers measured at the back aperture of the objective were typically ~ 40-60 mW.

Masks were designed with Microsoft Powerpoint, Adobe Illustrator, Adobe Photoshop, and Delcam Powershape-e. For sequential presentation of masks along the optical axis through solution, LabView software coordinated mask presentation with movement of the fine focus knob of the microscope, which was controlled by a motorized driver (Prior, H122). Vertical step sizes ranged from 0.1 to 0.5 μm, with exclusive use of 0.3-μm step sizes in Chapter 3 and for pillar topographies in Chapter 2. For structures shown in Figures 2.17, 2.18, and 2.19, the step sizes were 0.1 μm. Unless otherwise noted, all other step sizes may be assumed to be 0.5 μm, except for structures shown in

Figures 2.1 and 2.5, which were fabricated without the motorized z-stepper. Fabrication solution was 400 mg $mL^{-1}$ BSA diluted into a solution of 2-10 mM methylene blue (MB) in 20 mM HEPES buffer (pH = 7.4). For experiments in Chapter 3 and several experiments in Chapter 2, the fabrication solution was filtered using a 0.2-µm filter next to a flame just prior to use, and the MB concentration was 7.5-10 mM (prior to filtering). Further fabrication details, such as structure heights and solution concentrations/preparation are given as needed for individual experiments.

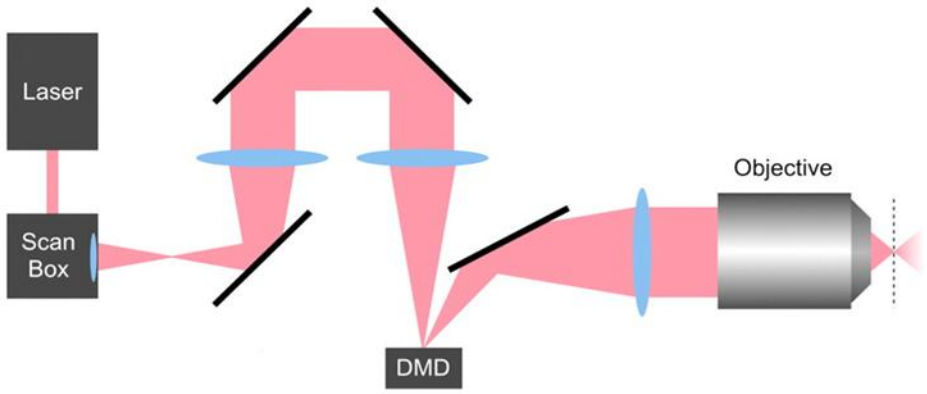


Figure 1.2: Experimental setup for fabrication of microstructures by DMD multiphoton lithography. Reprinted with permission. [61]

### *1.3.4.2 Cell Culture Conditions*

For experiments with *E. coli* RP9535 (ΔcheA), cells were streaked on 1.5% agar (Becton, Dickinson and Company), 1% tryptone broth (Becton, Dickinson and Company), and 0.5% NaCl and grown at 35 °C. Single colonies were used to inoculate overnight cultures in tryptone broth that were grown at 32 °C on a rotary shaker (200 rpm). Overnight cultures were diluted and grown to exponential phase (optical densities at 600 nm ($OD_{600}$) ~ 0.3 to 0.6) for experiments.

The majority of bacterial studies were performed with PA14 and PA14 pMRP9-1 (gfp-expressing) kindly provided by the laboratory of Marvin Whiteley. PA14 pMRP9-1 cells were streaked from freezer stocks on tryptic soy agar (EMD Chemicals) containing 300 μg/mL carbenicillin disodium salt (Fisher BioReagents). For overnight cultures, 1 to 3 single colonies were selected from plates and grown in tryptic soy broth (TSB) (EMD Chemicals or Bio-Link Scientific) containing 150 μg/mL carbenicillin. Overnight cultures (~ 14 to 16 hrs) were shaken on a rotary shaker (200 rpm) at 37 °C and grown to saturation. Overnight cultures were diluted into TSB and grown to exponential phase ($OD_{600}$ ~ 0.1 to 0.5). Cells were then either used directly for experiments or diluted to a specific inoculation density. For all experiments in Chapter 3 and some experiments in Chapter 2, cells in exponential phase were diluted to either 0.01 or 0.1 $OD_{600}$ absorbance readings, as specified in the relevant sections, in 1/3 TSB containing 1 mM glucose. In the case of using 0.1 $OD_{600}$ inoculation densities, overnight cultures were diluted into 1/3 TSB containing 1 mM glucose. The same culture conditions were used for *P. aeruginosa* PA14 without the use of carbenicillin.

#### *1.3.4.3 Flow Cell Assays*

The flow cell system was a once-through continuous culture device that was described previously in further detail [62, 68]. Structures were rinsed with several 20-mL volumes of 20 mM HEPES (pH = 7.4) prior to inoculation with cells. Flow cell and inoculation media was typically 1/3 TSB containing 1 mM glucose. Cells were inoculated at exponential phase or diluted to 0.1 $OD_{600}$. 1.5 to 3 mL of media containing cells was used to inoculate flow cell chambers, and cells were allowed to attach under static conditions for 15 min to over 1 hr prior to initiating flow (50 μL $^{min-1}$) with a peristaltic pump (Watson-Marlow).

#### *1.3.4.4 Static Assays*

Static assays for *E. coli* RP9535 were conducted within Grace BioLab adhesive flow cell devices attached to coverglass. The static assays used for PA14 are described in the relevant experimental sections.

#### *1.3.4.5 Scanning Electron Microscopy*

Samples were typically prepared by immersion in successive solutions as follows: 5% glutaraldehyde (Ted Pella, Redding, CA), 20 mM HEPES (pH = 7.4), 20 mM HEPES (pH = 7.4), deionized water, deionized water, 50% ethanol, 100% ethanol (EtOH), 50% EtOH/50% methanol (MeOH), 100% MeOH, and 100% MeOH. Samples were dried overnight, sputter-coated with Pt/Pd to thicknesses of 5 to 15 nm, and imaged with a Supra 40VP electron microscope (Zeiss).

#### *1.3.4.6 Atomic Force Microscopy*

Atomic force microscopy images were acquired in tapping mode with incidental contact on an MFP-3D-BIO atomic force microscope (Asylum Research).

## 1.4 Conclusion and Preview of Chapters

Dynamic-mask-based multiphoton lithography is a technology for rapidly-prototyping three-dimensional structures of arbitrary complexity with submicron resolution. In the present work, it was used to study *P. aeruginosa* attachment on topographical surfaces to understand how such surfaces can be used to influence (e.g., inhibit or promote) attachment and biofilm formation. Topographical designs were developed in consideration of multiple factors, including those associated with size and dimensions of the topographical features relative to PA14 cells, limiting cell-cell contacts with features of appropriate heights (e.g., pillars and variations on a commercially-

available topography), and the effects of placing dissimilar features together (e.g., lotus leaf-inspired features of various heights).

Chapter 2 explores a variety of topographies for influencing bacterial attachment, including designs based on microscale leaf surfaces and mathematical functions, variations on a commercially-available surface, pillars, and microchamber arrays. The approaches developed in Chapter 3 generally involve smaller feature dimensions, including grooves and submicron holes of various sizes subtracted from a surface. Finally, at the end of Chapter 3, future directions for this work on microscale levels and ideas for extending this work into nanoscale levels are presented.

## 1.5 REFERENCES


[1] R. A. Weiss, "The Leeuwenhoek Lecture 2001. Animal Origins of Human Infectious Disease," *Philosophical Transactions: Biological Sciences* 356, no. 1410, Origins of HIV and the AIDS Epidemic (2001): 955 + 957-977.

[2] G. Drews, "The Roots of Microbiology and the Influence of Ferdinand Cohn on Microbiology of the 19th Century," *FEMS Microbiology Reviews* 24 (2000): 225-249.

[3] C. Gradmann, "Heinrich Hermann Robert Koch," *Encyclopedia of Life Sciences*, John Wiley & Sons (2001).

[4] M. Schwartz, "The Life and Works of Louis Pasteur," *Journal of Applied Microbiology* 91 (2001): 597-601.

[5] A. T. Heinrici, "Studies of Freshwater Bacteria: I. A Direct Microscopic Technique," *Journal of Bacteriology* 25 (1933): 277-286.

[6] L. Hall-Stoodley, J. W. Costeron, and P. Stoodley, "Bacterial Biofilms: From the Natural Environment to Infectious Diseases," *Nature Reviews* 2 (2004): 95-108.

[7] T. C. Mah and G. A. O'Toole, "Mechanisms of Biofilm Resistance to Antimicrobial Agents," *Trends in Microbiology* 9, no. 1 (2001): 34-39.

[8] J. W. Costerton, P. S. Stewart, and E. P. Greenberg, "Bacterial Biofilms: A Common Cause of Persistent Infections," *Science* 284: 1318-1322.

[9] P. Stoodley, K. Sauer, D. G. Davies, and J. W. Costerton, "Biofilms as Complex Differentiated Communities," *The Annual Review of Microbiology* 56 (2002): 187-209.

[10] D. de Beer, P. Stoodley, F. Roe, and Z. Lewandowski, "Effects of Biofilm Structures on Oxygen Distribution and Mass Transport," *Biotechnology and Bioengineering* 43 (1994): 1131-1138.

[11] J. M. Vroom, K. J. DeGrauw, H. C. Gerritsen, D. J. Bradshaw, P. D. Marsh, G. K. Watson, J. J. Birmingham, and C. Allison, "Depth Penetration and Detection of pH Gradients in Biofilms by Two-Photon Excitation Microscopy," *Applied and Environmental Microbiology* 65, no. 8 (1999): 3502-3511.

[12] M. R. Parsek and T. Tolker-Nielsen, "Pattern Formation in *Pseudomonas aerugionsa* Biofilms," *Current Opinion in Microbiology* 11 (2008): 560-566.

[13] K. Lewis, "Persistor Cells, Dormancy and Infectious Disease," *Nature Reviews* 5 (2007): 48-56.

[14] R. Nielson, B. Kaehr, and J. B. Shear, "Microreplication and Design of Biological Architectures using Dynamic-Mask Multiphoton Lithography," *Small* 5, no. 1 (2008): 120-125.

[15] J. Lam, R. Chan, K. Lam, and J. W. Costerton, "Production of Mucoid Microcolonies by *Pseudomonas aeruginosa* within Infected Lungs in Cystic Fibrosis," *Infection and Immunity* 28, no. 2 (1980): 546-556.

[16] P. K. Singh, A. L. Schaefer, M. R. Parsek, T. O. Moninger, M. J. Walsh, and E. P. Greenberg, "Quorum-Sensing Signals Indicate that Cystic Fibrosis Lungs are Infected with Bacterial Biofilms," *Nature* 407 (2000): 762-764.

[17] N. C. Caiazza and G. A. O'Toole, "SadB is Required for the Transition for Reversible to Irreversible Attachment during Biofilm Formation by *Pseudomonas aeruginosa* PA14," *Journal of Bacteriology* 186, no. 14 (2004): 4476-4485.

[18] K. Vasilev, J. Cook, and H. J. Greisser, "Antibacterial Surfaces for Biomedical Devices," *Expert Reviews of Medical Devices* 6, no. 5 (2009): 553-567.

[19] E. M. Hetrick and M. H. Schoenfisch, "Reducing Implant-Related Infections: Active Release Strategies," *Chemical Society Reviews* 35 (2006): 780-789.

[20] E. Kenawy, S. D. Worley, and R. Broughton, "The Chemistry and Application of Antimicrobial Polymers: A State-of-the-Art Review," *Biomacromolecules* 8, no. 5 (2007): 1359-1384.

[21] G. Cheng, H. Xue, Z. Zhang, S. Chen, S. Jiang, "A Switchable Biocompatible Polymer Surface with Self-Sterilizing and Nonfouling Capabilities," Angewandte Chemie International Edition 47 (2008): 8831-8834.

[22] M. Zilberman and J. J. Elsner, "Antibiotic-Eluting Medical Devices for Various Applications," Journal of Controlled Release 130 (2008): 202-215.

[23] P. Wu and D. W. Grainger, "Drug/Device Combinations for Local Drug Therapies and Infection Prophylaxis," *Biomaterials* 27 (2006): 2450-2467.

[24] T. S. J. Elliott, H. A. Moss, S. E. Tebbs, I. C. Wilson, R. S. Bosner, T. R. Graham, L. P. Burke, and M. H. Faroqui, "Novel Approach to Investigate a Source of Microbial Contamination of Central Venous Catheters," *European Journal of Clinical Microbiology and Infectious Diseases* 16 (1997): 210-213.

[25] W. Vongpatanasin, L. D. Hillis, and R. A. Lange, "Prosthetic Heart Valves," *The New England Journal of Medicine* 335, no. 6 (1996): 407-416.

[26] P. Ramritu, K. Halton, P. Collignon, D. Cook, D. Fraenkel, D. Battistutta, M. Whitby, and N. Graves, "A Systematic Review Comparing the Relative Effectiveness of Antimicrobial-Catheters in Intensive Care Units," *American Journal of Infection Control* 36, no. 2 (2008): 104-117.

[27] M. Rai, A. Yadav, and A. Gade, "Silver Nanoparticles as a New Generation of Antimicrobials," *Biotechnology Advances* 27 (2009): 76-83.

[28] F. Furno, K. S. Morley, B. Wong, B. L. Sharp, P. L. Arnold, S. M. Howdle, R. Bayston, P. D. Brown, P. D. Winship,, and H. J. Reid, "Silver Nanoparticles and Polymeric Devices: A New Approach to Prevention of Infection?" *Journal of Antimicrobial Therapy* 54 (2004): 1019-1024.

[29] R. Kumar and H. Münstedt, "Silver Ion Release from Antimicrobial Polyamide/Silver Composites," *Biomaterials* 26 (2005): 2081-2088.

[30] C. Haefeli, C. Franklin, and K. Hardy, "Plasmid-Determined Silver Resistance in *Pseudomonas stutzeri* Isolated from a Silver Mine," Journal of Bacteriology 158, no. 1 (1984): 389-392.

[31] J. C. Tiller, C. Liao, K. Lewis, and A. M. Klibanov, "Designing Surfaces that Kill Bacteria on Contact," *Proceedings of the National Academy of Sciences* 98, no 11 (5981-5985).

[32] R. Kügler, O. Bouloussa, and F. Rondelez, "Evidence of a Charge-Density Threshold for Optimum Efficiency of Biocidal Cationic Surfaces," *Microbiology* 151 (2005): 1341-1348.

[33] R. T. Carson, E. Larson, S. B. Levy, B. M. Marshall, and A. E. Aiello, "Use of Antibacterial Consumer Products Containing Quaternary Ammonium Compounds and Drug Resistance in the Community," *Journal of Antimicrobial Therapy* (2008): 1160-1162.

[34] R. E. W. Hancock, "Cationic Peptides: Effectors in Innate Immunity and Novel Antimicrobials," *Lancet* 1 (2001): 156-164.

[35] R. E. W. Hancock and H. Sahl, "Antimicrobial and Host Defense Peptides as New Anti-Infective Therapeutic Strategies," *Nature Biotechnology* 24, no. 12 (2006): 1551-1557.

[36] S. M. Marxer, A. R. Rothrock, B. J. Nablo, M. E. Robbins, and M. H. Schoenfisch, "Preparation of Nitric Oxide (NO)-Releasing Sol-Gels for Biomaterial Applications," *Chemistry of Materials* 15 (2003): 4193-4199.

[37] S. E. Tebbs, A. Sawyer, T. S. J. Elliott, M. R. C. Path, "Influence of Surface Morphology on In Vitro Bacterial Adherence to Central Venous Catheters," *British Journal of Anesthesia* 72, no 5 (1994): 587-591.

[38] S. H. Flint, J. D. Brooks, and P. J. Bremer, "Properties of the Stainless Steel Substrate, Influencing the Adhesion of Thermo-Resistant *Streptococci*," *Journal of Food Engineering* 43 (2000): 235-242.

[39] R. L. Taylor, J. Verran, G. C. Lees, and A. J. P. Ward, "The Influence of Substratum Topography on Bacterial Adhesion to Polymethyl Methacrylate," *Journal of Materials Science: Materials in Medicine* 9 (1998): 17-22.

[40] N. Mitik-Dineva, J. Wang, V. K. Truong, P. Stoddart, F. Malherbe, R. J. Crawford, and E. P. Ivanova, "*Escherichia coli*, *Pseudomonas aeruginosa*, and *Staphylococcus aureus* Attachment Patterns on Glass Surfaces with Nanoscale Roughness," *Current Microbiology* 58 (2009): 268-273.

[41] L. Rizzello, B. Sorce, S. Sabella, G. Vecchio, A. Galeone, V. Brunetti, R. Cingolani, and P. P. Pompa, "Impact of Nanoscale Topography on Genomics and Proteomics of Adherent Bacteria," *ACS Nano* 5, no 3 (2011): 1865-1876.

[42] S. D. Puckett, E. Taylor, T. Raimondo, and T. J. Webster, "The Relationship Between the Nanostructure of Titanium Surfaces and Bacterial Attachment," *Biomaterials* 31 (2010): 706-713.

[43] J. M. Willey, L. M. Sherwood, and C. J. Woolverton, *Microbiology*, 7th edition (New York: McGraw-Hill, 2008), 66.

[44] C. Díaz, P. L. Schilardi, R. C. Salvarezza, and M. F. L. de Mele, "Nano/Microscale Order Affects the Early Stages of Biofilm Formation on Metal Surfaces," *Langmuir* 23 (2007): 11206-11210.

[45] A. I. Hochbaum and J. Aizenberg, "Bacteria Pattern Spontaneously on Periodic Nanostructure Arrays," Nano Letters 10 (2010): 3717-3721.

[46] http://www.sharklet.com/technology/; retrieved April 4, 2011.

[47] K. K. Chung, J. F. Schumacher, E. M. Sampson, R. A. Burne, P. J. Antonelli, and A. B. Brennan, "Impact of Engineered Surface Microtopography on Biofilm Formation of Staphylococcus aureus," *Biointerphases* 2, no. 2 (2007): 89-94.

[48] E. T. Ritschdorff and J. B. Shear, "Multiphoton Lithography using a High-Repetition Rate Microchip Laser," *Analytical Chemistry* 82 (2010: 8733-8737.

[49] C. N. LaFratta, J. T. Fourkas, T. Baldacchini, and R. A. Farrar, "Multiphoton Fabrication," *Angewandte Chemie International Edition* 46 (2007): 6238-6258.

[50] R. T. Hill and J. B. Shear, "Enzyme-Nanoparticle Functionalization of Three-Dimensional Protein Scaffolds," *Analytical Chemistry* 78, 19 (2006): 7022-7026.

[51] W. R. Zipfel, R. M. Williams, and W. W. Webb, "Nonlinear Magic: Multiphoton Microscopy in the Biosciences," *Nature Biotechnology* 21, no. 11 (2003): 1369-1377.

[52] C. Xu and W. W. Webb, "Multiphoton Excitation of Molecular Fluorophores and Nonlinear Laser Microscopy," in *Topics in Fluorescence Spectroscopy: Nonlinear and Two-Photon Induced Fluorescence*, vol. 5, ed. J. R. Lakowicz (New York: Plenum Press, 1997), 471-540.

[53] E. T. Ritschdorff, M. L. Plenert, and J. B. Shear, "Microsecond Analysis of Transient Molecules using Bi-Directional Capillary Electrophoresis," *Analytical Chemistry* 81, 21 (2009): 8790-8796.

[54] B. Kaehr and J. B. Shear, "Mask-Directed Multiphoton Lithography," *Journal of the American Chemical Society* 129 (2007): 1904-1905.

[55] J. B. Shear, "Multiphoton-Excited Fluorescence in Bioanalytical Chemistry," *Analytical Chemistry* 71, no. 17 (1999): 598A-605A.

[56] P. R. Callis, "The Theory of Two-Photon-Induced Fluorescence Anisotropy," in *Topics in Fluorescence Spectrscopy: Nonlinear and Two-Photon Induced Fluorescence*, vol. 5, ed. J. R. Lakowicz (New York: Plenum Press, 1997).

[57] M. Göppert-Mayer 1931, "Über Elementarakte mit zwei Quantensprüngen," *Annalen der Physik* 9 (1995): 273-295.

[58] B. Kaehr and J. B. Shear, "Multiphoton Fabrication of Chemically Responsive Protein Hydrogels for Microactuation," *Proceedings of the National Academy of Sciences* 105, no. 26 (2008): 8850-8854.

[59] H. Sun and S. Kawata, "Two-Photon Photopolymerization and 3D Lithographic Microfabrication," *Advances in Polymer Science* 170 (2004): 169-273.

[60] J. D. Spikes, H. Shen, P. Kopečková, and J. Kopeček, "Photodynamic Crosslinking of Proteins. III. Kinectics of the FMN- and Rose Bengal-Sensitized Photooxidation and Intermolecular Crosslinking of Model Tyrosine-Containing *N*-(2-Hydroxypropyl)methacrylamide Copolymers," *Photochemistry and Photobiology* 70, 2 (1999): 130-137.

[61] B. Kaehr and J. B. Shear, "High-Throughput Design of Microfluidics Based on Directed Bacterial Motility," *Lab on a Chip* 9 (2009): 2632-2637.

[62] J. L. Connell, A. K. Wessel, M. R. Parsek, A. D. Ellington, M. Whiteley, and J. B. Shear, "Probing Prokaryotic Social Behaviors with Bacterial "Lobster Traps," mBio 1, no. 4 (2010): 202-210.

[63] B. Kaehr, R. Allen, D. J. Javier, J. Currie, and J. B. Shear, "Guiding Neuronal Development with *in situ* Microfabrication," *Proceedings of the National Academy of Sciences* 101, no. 46 (2004): 16104-16108.

[64] S. K. Seidlits, C. E. Schmidt, and J. B. Shear, "High-Resolution Patterning of Hydrogels in Three Dimensions using Direct-Write Photofabrication for Cell Guidance," *Advanced Functional Materials* 19 (2009): 3543-3551.

[65] R. Allen, R. Nielson, D. D. Wise, and J. B. Shear, "Catalytic Three-Dimensional Protein Architectures," *Analytical Chemistry* 77 (2005): 5089-5095.

[66] R. T. Hill and J. B. Shear, "Enzyme-Nanoparticle Functionalization of Three-Dimensional Protein Scaffolds," *Analytical Chemistry* 78 (2006): 7022-7026.

[67] J. L. Lyon, R. T. Hill, J. B. Shear, and K. J. Stevenson, "Direct Electrochemical and Spectroscopic Assessment of Heme Integrity in Multiphoton Photo-Cross-Linked Cytochrome *c* Structures*," Analytical Chemistry* 79 (2007): 2303-2311.

# Chapter 2: Exploration of Topographies for Influencing and Inhibiting Bacterial Attachment and Biofilm Formation

## 2.1 INTRODUCTION

Since so little is known about how topography influences bacterial attachment, this thesis work considers a variety of topographical designs and ideas. Important design parameters to consider may include

1. the size and shape of the organism relative to feature sizes [1],
2. the sizes of extracellular organelles used by organisms for motility and attachment (e.g. fimbriae/pili and flagella) [1],
3. the possibility for cell-cell contact either by direct cell body interactions or interactions between extracellular organelles [2],
4. the possibility for intercellular chemical signaling (i.e. this might be blocked by topographical design),
5. the effects of placing dissimilar features together [3], and
6. surface wettability [1].

Except for a few studies in section 2.2.1, the bacteria used in this work were *P. aeruginosa*, which avidly form biofilms on many biotic and abiotic surfaces [10]. *P. aeruginosa* are motile and rod-shaped with diameters of ~ 0.5 to 0.8 μm and lengths of ~ 1 to 2 μm. They have swimming motility due to a single, polar flagellum and surface-associated motility due to polar type IV pili. Flagella have diameters of ~ 20 nm and can be up to 15 to 20 μm long [4], while type IV pili (or fimbriae) are ~ 6 nm in diameter, up to several μm in length, and can be located at either one or both poles of a cell [1]. Type IV pili are associated with twitching motility on surfaces [5-7], which is manifested as jerky cell movements and is believed to occur by extension and retraction of the pili [8, 9]. Flagella and type IV pili have been shown to be important for motility, surface

attachment, cell-cell interactions, and biofilm formation [10-13]. *P. aeruginosa* also have type 1 pili (or fimbriae) located over their cell bodies for attachment to surfaces, such as host cells [4].

With such a variety of motility behaviors contributing to biofilm formation, it may be that disruption of particular behaviors will inhibit biofilm formation while allowing individual attachment of cells. It may also be important to limit cell-cell contacts, an idea that was behind many of the topographical designs presented in this chapter, such as pillars. This chapter explores a number of topographical ideas, which evolved along with the cell conditions used to test them. That is, designing relevant assays for testing topographical influences on cells is just as important as the topographical designs themselves. Difficulties and limitations associated with various assays led to open-ended conclusions and will be discussed along with the relevant work. One theme that emerges from this chapter is exploration of topographical designs, which was possible by rapid-prototyping with DMD multiphoton lithography.

## 2.2 TOPOGRAPHIES INSPIRED BY SUPERHYDROPHOBIC LEAF SURFACES

The naturally-antifouling properties of superhydrophobic leaf surfaces, such as lotus and taro leaves, are currently being investigated in the area of biomimetic research. Scanning electron microscopy images have revealed multiple topographical layers within the leaf surfaces – including nanoscale, hairlike features on microscale protrusions. It is hypothesized that the combination of micro- and nano-scale topographies, along with the waxy surface chemistry, makes these leaves superhydrophobic (i.e. having contact angles between 150° to 180°) and therefore self-cleaning. The self-cleaning property is called "the Lotus effect" and is being used to develop surfaces that are highly water-repellent. [14-17]

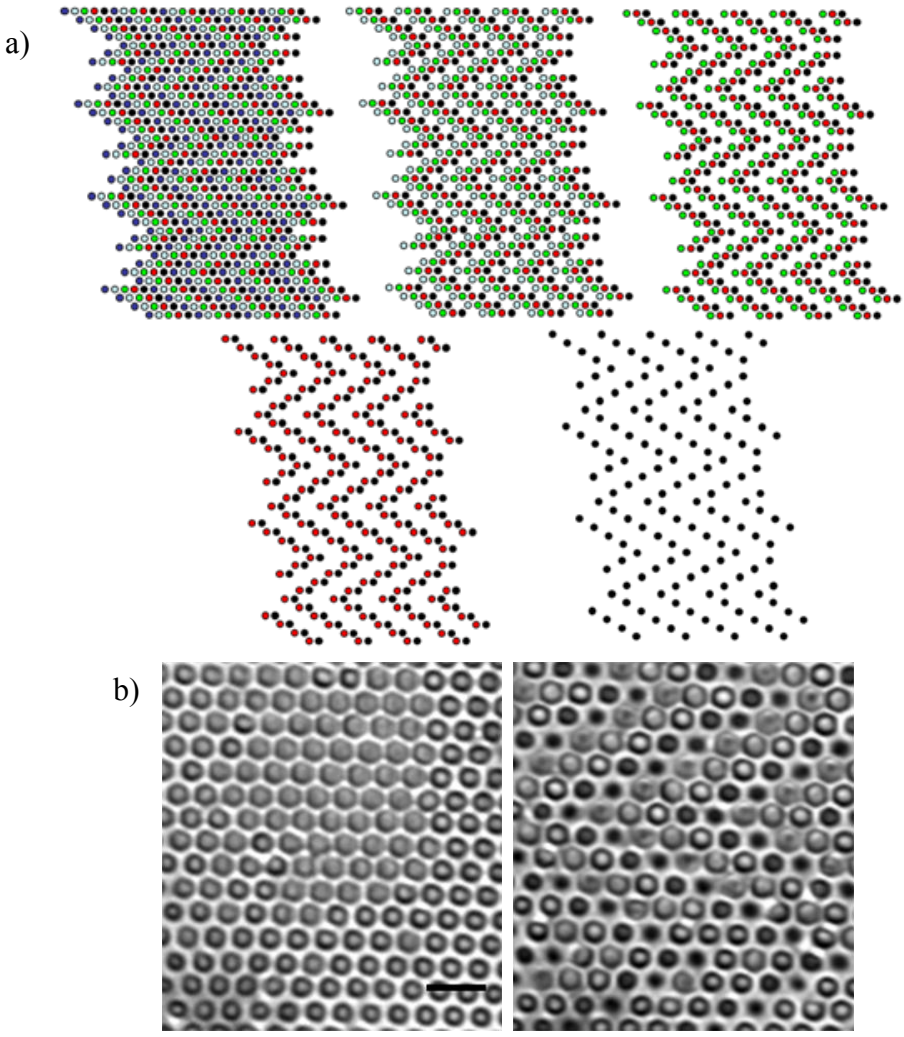


Figure 2.1: Simple lotus leaf-inspired structures. a) Mask design for lotus leaf-inspired features of different heights. In this schematic, different colored circles represent cylinders of different heights. For example, red cylinders were the second tallest features and black cylinders were the tallest features. b) brightfield images of lotus leaf-inspired BSA structures with same height features (left) and different height features (right) after 27.5 hrs static incubation with *E. coli* RP9535. Cells are not visible in this image mostly due to low contrast within the topographical features. Scale bar = 5 μm.

The microscale structure of the lotus leaf has rounded protrusions [14] that inspired topographical designs on size-scales similar to bacteria. Initial structures fabricated with lotus leaf-inspired topographies were simple cylinders with same and differential heights (Figure 2.1). In Figure 2.1, structures were incubated with *E. coli* RP9535 cells (rod-shaped cells of ~ 0.5-μm diameter and ~ 1-μm in length) for 27.5 hrs under static conditions (no flow). Brightfield images provided low contrast of bacterial cells, but cell movement could be discerned between and above features.

Larger cylinders were tested under static conditions (no flow) with PA14 cells to observe cell attachment on top of features wider than cell lengths (Figure 2.2). This experiment was derived from a previous experiment in which features with successively smaller cylinders stacked atop one another collapsed under flow, leaving cylinders in lower layers still intact (data not shown). During that experiment, a cell was observed to spin with its long axis parallel to the top of a cylinder. The cell was not attached to the surface but spun freely on the cylinder top, which appeared to have lips around its rim, for at least several minutes. (*Note: brightfield imaging likely produced an artifact that appeared to be lips around the rim of the cylinder.) Consequently, a hypothesis was made that cells might be prohibited from attaching to cylinders with lips.

In the experiment shown in Figure 2.2, cylinders were fabricated with (Figure 2.2 c and d) and without lips (Figure 2.2 a and b). Contrary to the hypothesis, cells were not observed to spin on the cylinder tops for either type of cylinder. Smaller cylinders closer to the length of a single cell (~1 to 2 μm) may be useful to test, as the cylinders tested were about 5 μm with inner diameters of ~ 3 to 4 μm for the cylinders with lips.

As with the smaller cylinders shown in Figure 2.1, bacteria attached between and on top of features. For the cylinders with lips, cells often swam at fast speeds along the inner rim of cylinders before attachment to cylinder tops. In Figure 2.2, images (b) and

(d) show cell attachment on top of cylinders without and with lips, respectively. From these images and others that are not shown, it appears that more cells attached to the tops of features with lips than to those without lips. However, only two structures were imaged for features without lips and four for features with lips, so more replicates would be needed to assess this result. Compared to *E. coli* RP9535, PA14 cells showed decreased movement on surfaces, which is likely due to how strongly PA14 attaches.

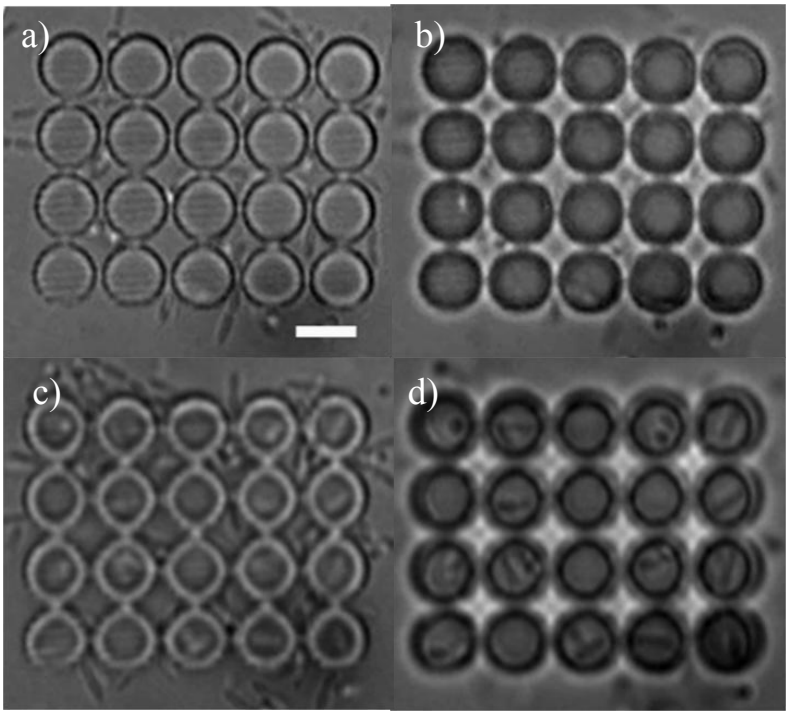


Figure 2.2: PA14 attachment 30 minutes post-inoculation under static conditions to cylinders without lips ((a) and (b)) and with 2-µm-tall lips ((c) and (d)). The left-hand images were taken with the focus near the coverglass and the right-hand images were taken near the top of the cylinders. The cylinders in image (b) appear to have lips, but that is likely an artifact of brightfield imaging. Overall structure heights were ~ 5 to 6 µm with 0.5-µm step sizes. Scale bar = 5 µm.

Cylinders intended to be without lips (i.e. those involving only one mask) appeared to have lips in brightfield images. Both types of cylinders also appeared to have

crosslinked protein between features. To ascertain if these appearances were image artifacts, structures were dehydrated and imaged by scanning electron microscopy (SEM) (Figure 2.3). The SEM images showed cylinders that were sunken in the middle, likely due to the fixation process, but apparently without lips. However, there was crosslinked protein between features, indicating that structure boundaries were incompletely resolved in the fabrication step. The SEM images also showed the raster scanning lines across features.

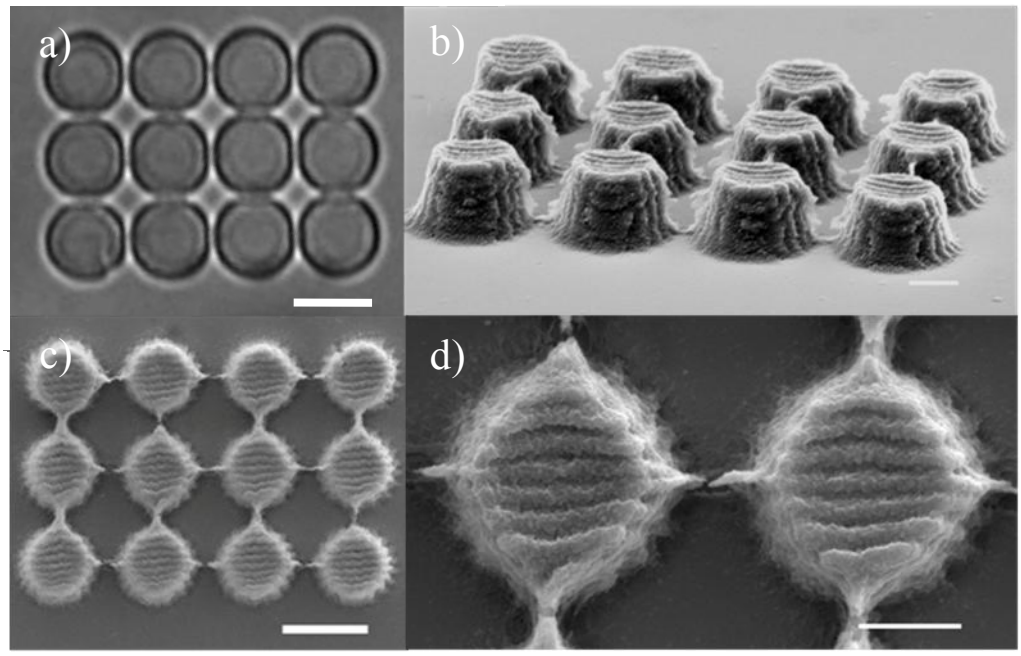


Figure 2.3: Brightfield image (a) and SEM images (b) through (d) of cylinders fabricated without lips. In the brightfield image, the cylinders appear to have lips as well as protein fabricated between cylinders – both features that were not specified by the mask. SEM images of the structures show cylinders that are sunken but apparently without lips. However, there is crosslinked protein between cylinders. Scale bar = 5 μm.

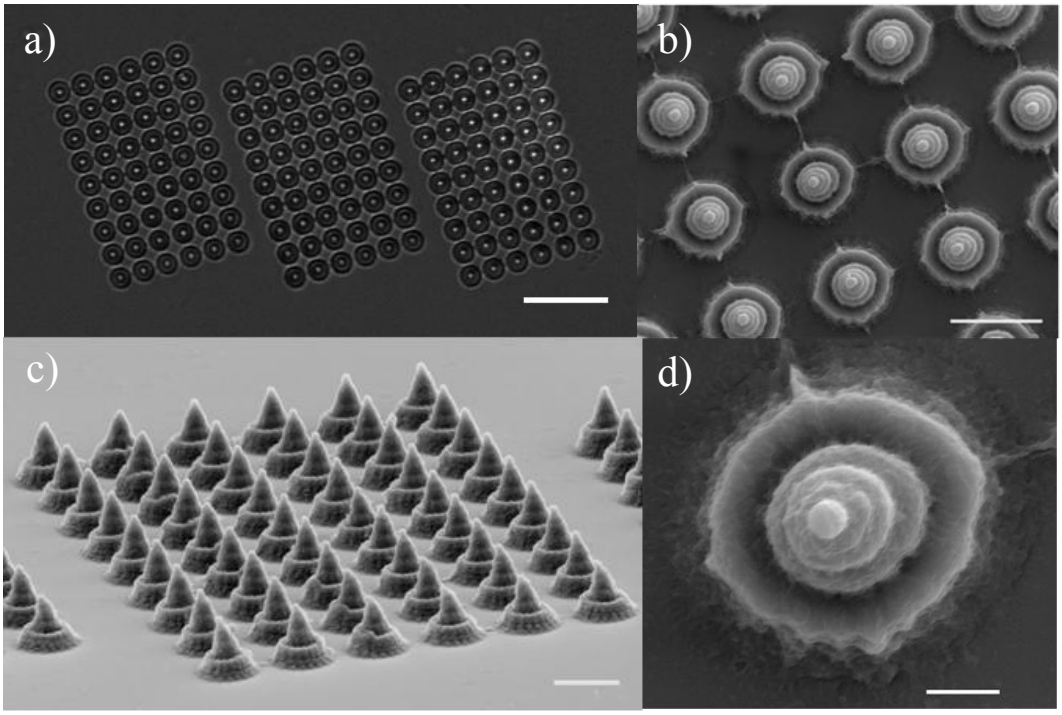


Figure 2.4: Layered lotus-inspired structures fabricated with BSA using masks having successively smaller circles. Brightfield image of structures in buffer (a) and SEM images of dehydrated structures ((b) through (d)). Dehydration caused the structures to shrink. Scale bars = 20 μm for (a), 5 μm for (b) and (c), and 1 μm for (d).

While the previous experiments involved structures with simple cylinders, the microscale topography of the lotus leaf has rounded protrusions atop rounded base features [14], which inspired the topographical design shown in Figure 2.4. These features were tested with PA14 cells, but as in previous experiments involving only brightfield imaging, cells were difficult to discern due to low contrast.

The taro leaf is another superhydrophobic leaf surface that has hexagonal features with raised protrusions in the centers [15]. Figure 2.5 shows a structure with a design based on the microscale topography of the taro leaf. This structure was incubated with *E. coli* RP9535 cells under static (no flow) conditions for 21 hrs. Single or low numbers of

cells were isolated in interstitial spaces between features. The isolation of single cells in interstitial spaces was an unexpected result that generated the experimental idea of microchambers for single or low numbers of bacterial cells (section 2.3).

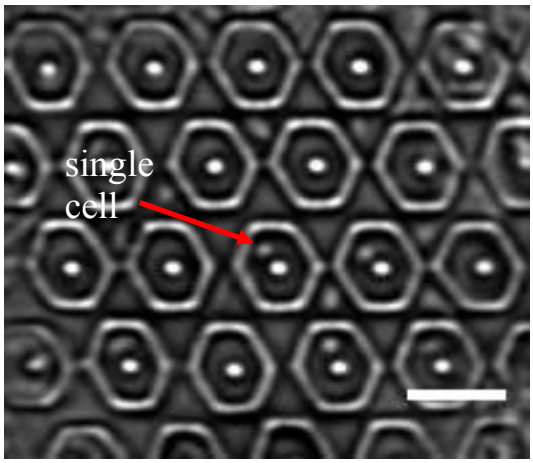


Figure 2.5: Single cells isolated in the interstitial spaces of features inspired by the microscale topography of the taro leaf. *E. coli* RP9535 are rod-shaped with diameters of ~ 0.5 μm and lengths of ~ 1 μm, but many of the cells in this image were attached by one pole so that the cell appeared small and rounded. Alternatively, cells attached by one pole may have been at an angle smaller than 90° with the bottom surface, making them appear larger than the diameter of a single cell. Scale bar = 5 μm.

## 2.3 MICROCHAMBER ARRAYS FOR ISOLATING SINGLE OR LOW NUMBERS OF BACTERIA

Previous work in the Shear group has led to development of microchambers for isolating small numbers of densely-packed bacterial populations [22-24]. The mass transport properties of the cross-linked protein chambers allow exchange of nutrients and waste, and cells were shown to divide at rates similar to those of batch-culture cells [24]. However, chambers had sizes that could typically hold hundreds of cells, and entrances for chambers were parallel to the coverglass surface. By contrast, the isolated cells

observed and imaged within the taro leaf topography led to the idea of entrapping single to low numbers of bacteria beneath an appropriately-designed surface (Figure 2.6). Surfaces were designed with arrays of small apertures that allowed entrance of PA14 cells, which were observed to occupy the apertures (or microchambers) for at least tens of seconds. In these "microchamber arrays," cells occupied chambers singly (Figure 2.6a) and in multiples (Figure 2.6e) and exhibited unusual behaviors. For example, the three cells highlighted in Figure 2.6e rotated together in a pin-wheel fashion for at least tens of seconds. Such arrays could be useful for studying bacterial behaviors under spatial confinement on the size scale of the bacterium, such as cell division and quorum sensing.

While these initial studies were conducted with brightfield imaging, fluorescence experiments would be helpful for identifying bacteria since cells often displayed low contrast. For example, PA14 cells attach strongly to surfaces causing them to remain immobile for long periods of time within the chambers. During observation, a cell would sometimes move within a chamber that had previously appeared to be empty. Spiking in small numbers of cells of a different color into a sample (e.g., 10% cfp-expressing cells into a population of gfp-expressing cells) would be advantageous for assessing how long cells remain in chambers with open entrance apertures.

To enhance cell trapping, entrance apertures were made narrow relative to the microchambers (data not shown), and this idea could be developed further in future experiments. Cell trapping and loading might also be enhanced by changing the geometry of the chambers.

It would also be interesting to combine this idea with temperature-induced swelling for closing off entrance apertures, so that cells would be fully trapped. Connell et al. used temperature-induced swelling to grow up clonal populations of *P. aeruginosa* [24]. In that work, single cells were allowed to swim into chambers at ambient

temperature, and then the temperature was raised to 37° C ("biological" temperature) to swell the entrance closed. Microchamber arrays with single or low numbers of trapped cells, either with or without closed entrance apertures, could enable intriguing experiments involving cell-cell communication, cell division, surface attachment, and antibiotic resistance.

Even without swelling entrances closed, PA14 cells pack densely into microchambers (Figure 2.7) within short time scales – at least as early as 4 hrs. Optimization of cell loading conditions would likely decrease the time needed to fill chambers. The microchambers in Figure 2.7 were ~ 4-μm-tall with semi-transparent roofs (~ 1-μm thick) visible over the entrance arms. Cells were observed to swim into entrance apertures that appeared to be quite small, likely of sizes similar to their diameters. The structures appear tilted because the masks were not corrected for a skew (~ 5°) caused by reflection geometries off the DMD mirrors. PA14 cells showed fast swimming motility adhering to the geometry of their chamber (e.g., cells swam rapidly around the "track" in the letter "O."

As with previous work involving protein microchambers in the Shear group [22, 23], the structures in Figure 2.7 accumulated dense populations of bacteria relative to the large volume of cell media encompassing the structures. Here, chambers with open entrance apertures are shown to accumulate PA14 cells, rather than *E. coli* RP9535 "smooth swimmers" as in previous work. In similar experiments, Park et al. showed that *E. coli* accumulated in confined spaces at the ends of mazes fabricated in silicone elastomer due to chemical attractants secreted by the cells (chemotaxis) [25]. In their work, chamber sizes were 250 μm × 250 μm with entrance apertures 40-μm-wide – dimensions considerably larger than those used in the Shear group.

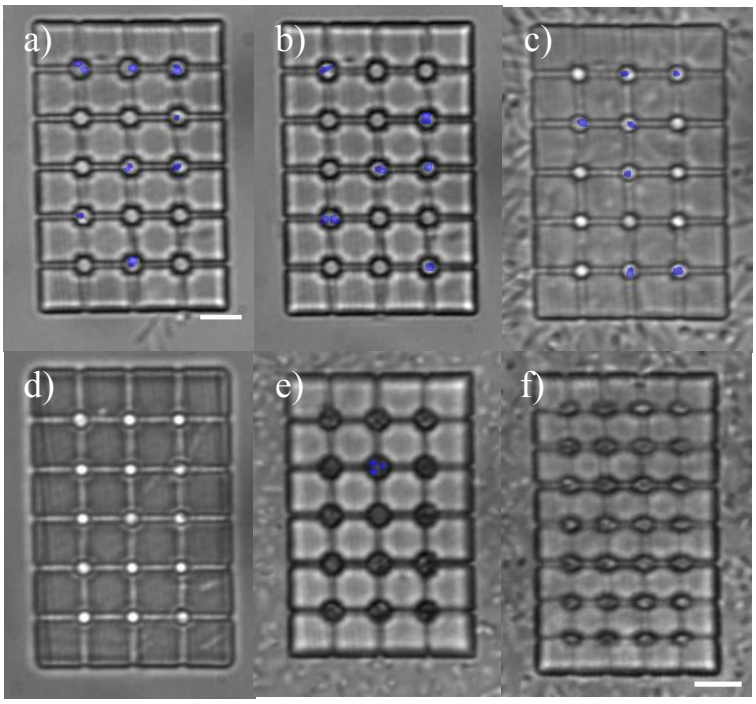


Figure 2.6: Microchamber arrays for isolating single or small numbers of bacteria. The structure shown in (a) was imaged 2 hrs post-inoculation with PA14 under flow. The same structure was imaged 4 hrs (b) and 14 hrs (c) post-inoculation. An image focused on the surface of the structure after 4 hrs (d) shows that cells highlighted in (b) were nestled down in the chambers, which were about 5- to 6-μm-tall. (e) and (f) show microchambers with different geometries; these structures were imaged 18.5 hrs post-inoculation with PA14 under static conditions. Cells with enough contrast to be distinguished from background were highlighted in (a) through (c). The structure in (e) contained multiple cells in each chamber so no attempt was made to highlight cells. However, 3 cells were highlighted in one chamber; these cells rotated in unison, resembling a pin-wheel, throughout a time-lapse movie. Cells were not highlighted in (f) due to poor contrast, but cells are visible as dark spots within chambers. The "grid-lines" connecting chambers were fabricated as tunnels for possible fast exchange (relative to diffusion through the walls) of intercellular signals in future experiments. In one time-lapse movie, a cell was caught at the edge of a chamber, presumably within a gridline, and the cell behaved like a spring with its body -- extending and contracting away from the source of its entrapment. Scale bars = 5 μm ((a) through (e) have the same scale).

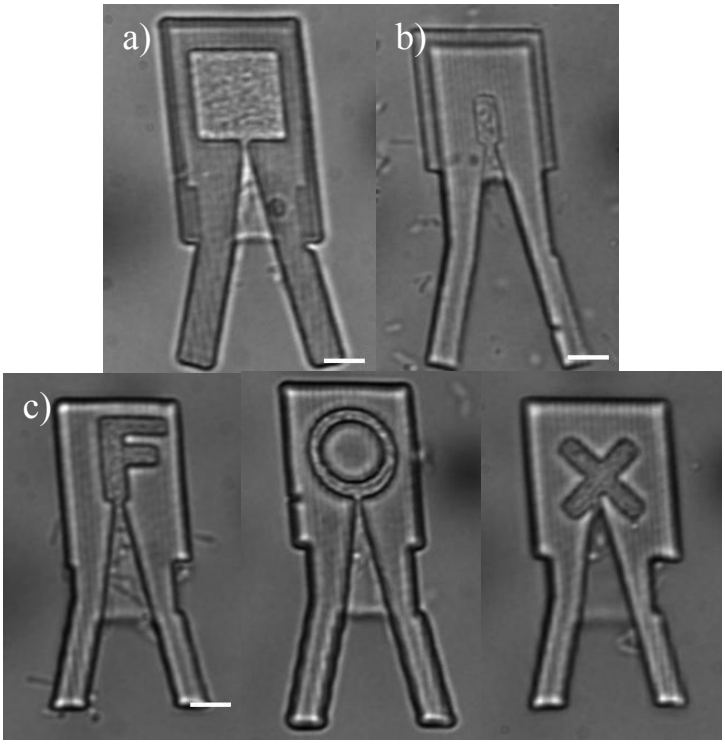


Figure 2.7: Microchambers for isolating small numbers of densely-packed PA14 cells. Even though entrance apertures appeared to be quite small (likely similar to the diameters of cells), PA14 cells filled small chambers of various sizes and geometries to high densities (to the point that cell movement appeared to cease.) (a) and (c) show structures 4 hrs post-inoculation under flow, while (b) shows a structure 14 hrs post-inoculation under static conditions (in this instance within the flow cell setup described in section 1.3.4. Scale bars = 5 μm.

An important result from these studies was the observation that PA14 cells were able to enter small apertures, presumably by their swimming motility. In the design of topographical surfaces for influencing attachment of PA14 cells and most likely other motile cell types, it is important to consider the sizes and geometries of apertures within surfaces. One considerable challenge for rod-shaped, motile bacteria is how to prevent cells from attaching within apertures between features while also preventing attachment of cells across the tops of those features.

## 2.4 VARIATIONS ON SHARKLET STRUCTURES

### 2.4.1 Small-Area Structures

A major advantage of DMD multiphoton lithography is the ability to rapidly-prototype structures with fabrication times of low to sub-minute time scales. (*Note: topographies over larger areas (e.g., Figure 2.11) created by stitching structures together generally require many hours of fabrication.) The advantages of rapid-prototyping for this work include the ability to test out many different structural designs with and without cells and, most importantly, to produce systematic variations in topography.

In this section, an experiment is described involving systematic variations of the Sharklet topography. Sharklet™ is a commercial antifouling topography developed by Brennan et al. that was described near the end of section 1.2.2 [18]. In the work by Brennan et al., the rectangular Sharklet features were spaced 2-μm apart, which allowed *S. aureus* cells (spherical cells with diameters of ~ 1 μm) to attach between features. Since the authors did not describe any systematic variation of feature spacings, it is likely that feature spacings of 2 μm are not ideal for the Sharklet topography or other topographies for bacteria on size scales similar to *S. aureus* (such as *P. aeruginosa*, and *E. coli*).

To test influences of feature spacings and also feature heights, 9 structural variations of Sharklet were fabricated from BSA onto coverglass (Figure 2.8). (*Note: there was no base layer of BSA for structures in this particular experiment). Feature spacings tested were 2 μm, 1 μm, and 0.5 μm, which are relevant to the size scale of many clinically-isolated bacteria, including *P. aeruginosa*.

Feature heights were 3 and 6 μm, since it was hypothesized that taller features might prohibit cell-cell mechanical contacts. Structures with features of alternating heights were fabricated, since it was hypothesized that *P. aeruginosa* would be unable to

attach across two features with height differences greater than the length of a single cell. In this instance, features differed in height by 3 μm, while *P. aeruginosa* cells are only 1 to 2 μm in length.

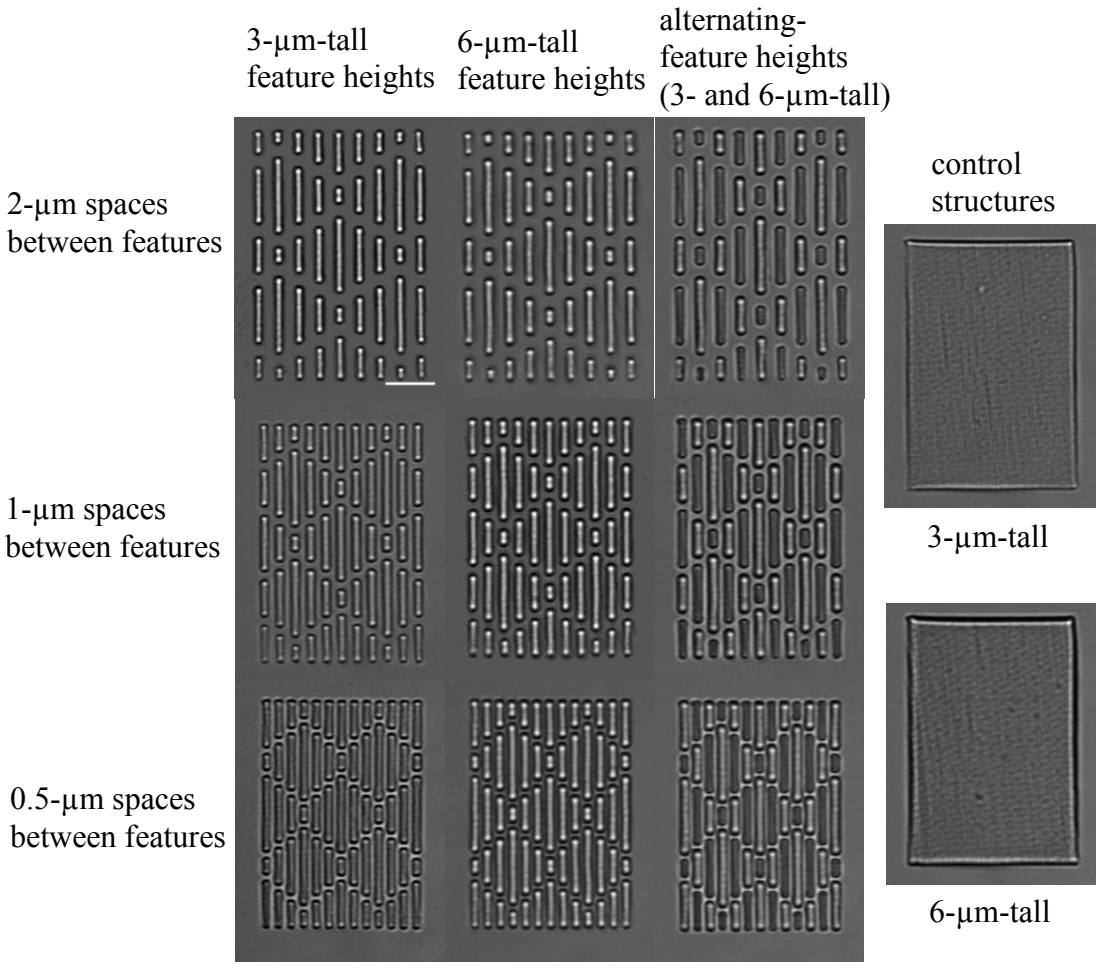


Figure 2.8: Sharklet structural variations tested in one particular experiment. Variations were made in spaces between features and feature heights, including alternating feature heights. Scale bar = 10 μm.

Figure 2.8 shows representative structures in cell media before inoculation with cells. For each of the 11 structure types (including control structures), 5 to 7 structures were fabricated in a flow cell with a total fabrication time of 2 hrs 10 min. Flow cells

containing structures were inoculated with PA14 cells expressing gfp at $OD_{600}$ = 0.4 in 1/3 TSB containing 1 mM glucose and 25 μg/mL nalidixic acid. Widefield and DIC images were acquired at several time points post-inoculation for each structure. Images were acquired on the coverglass surface and feature tops for all structure types and on top of 3-μm-tall features for structures with alternating feature heights.

One interesting result from this experiment was the observation of PA14 cell orientation between features with different spacings (Figure 2.9). For structures with features spaced 2-μm apart (the spacings used in Sharklet™ commercial topography) cells oriented in many directions between features. For structures with features spaced 1-μm apart, cells were confined to fewer orientations between features, with many cells oriented with their long axes parallel to the coverglass. For structures with 0.5-μm spaces, cells were largely constrained to attachment by their poles, frequently appearing as dots on the ends of the diamond patterns. These cell orientations are interesting in relation to PA14 attachment behaviors. PA14 have been shown to attach in two basic steps – first, "reversible" attachment by their poles followed by "irreversible" attachment with their long axes parallel to a surface [19]. The transition from reversible to irreversible attachment is associated with expression of specific proteins and has been shown to be critical for biofilm formation [19]. Structures that confine cells to specific orientations could be useful for understanding biofilm formation in relation to attachment behaviors of cells.

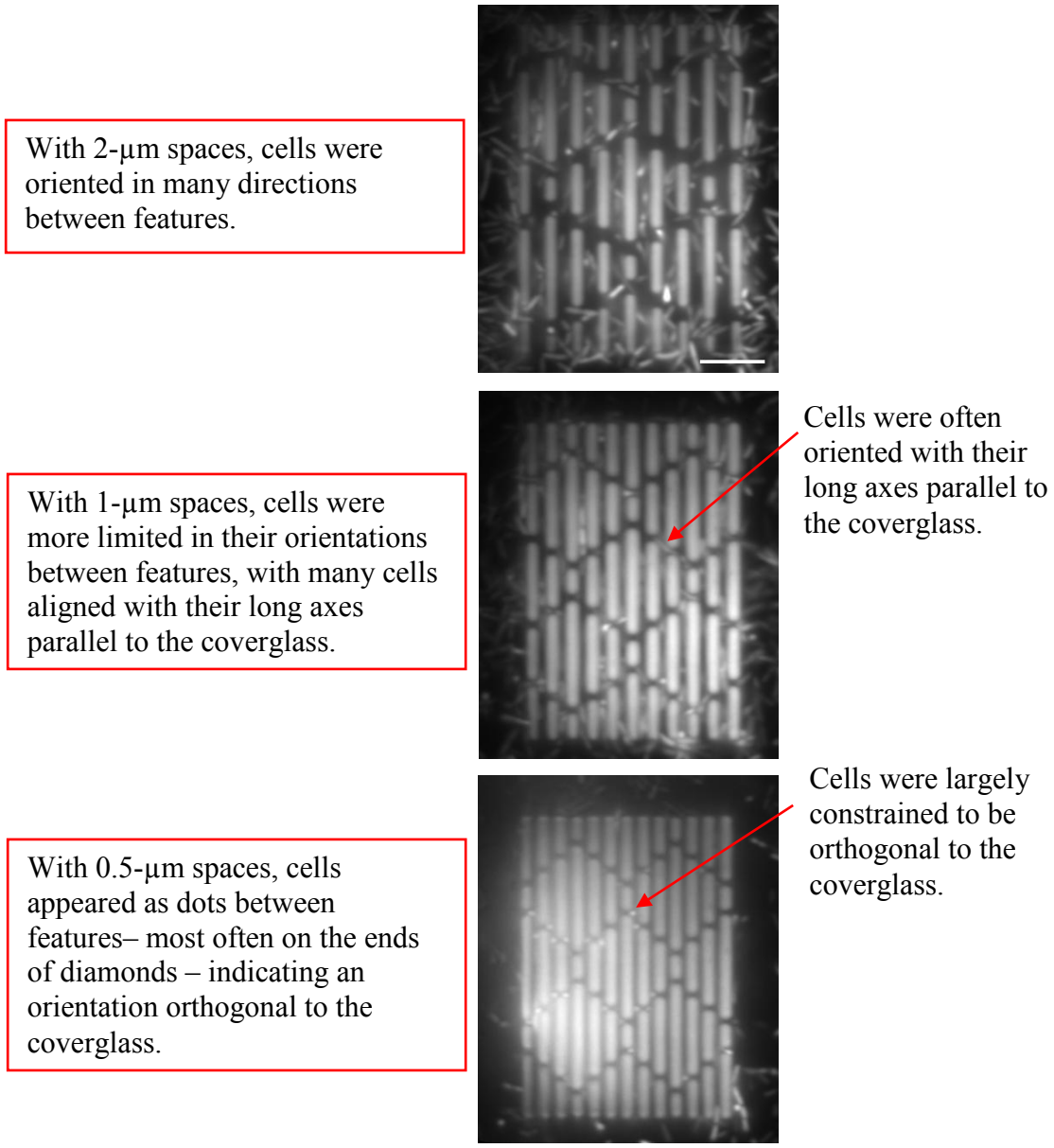


Figure 2.9: PA14 cell orientation within Sharklet structures having different spacings between features. Widefield fluorescence images of structures with gfp-expressing cells were acquired between 42.5 to 45 hrs post-inoculation under flow with the focus on the coverglass. Feature heights were 3 µm, but similar results were observed for structures with feature heights of 6 µm. Scale bar = 10 µm.

While cells were somewhat confined to certain orientations within features, it should be noted that cells attached across feature tops (from one feature to the next) for all three feature spacings and feature heights, including features with alternating heights. Attachment across features that were 3-μm-tall with spaces of 2 μm is shown in Figure 2.10. The observation that PA14 cells attach across features precludes the notion of preventing attachment of cells by simply placing features closer together. While placing features closer together reduces attachment between those features, attachment persists on the tops of features. The research question which is posed here and throughout this thesis is: how can attachment of motile cells, which can swim into small apertures, be prevented while simultaneously preventing attachment of the rod-shaped cells across feature tops?

Since *P. aeruginosa* cells are motile, they are able to swim into small apertures, such as those shown in Figure 2.7, and in Chapter 3, they are shown to attach within small vertically-oriented holes. An intriguing question to pose is how the motility of *P. aeruginosa* affects their attachment in relation to small apertures. Another question to ask is how the attachment of a nonmotile cell type, like *S. aureus*, differs in response to small apertures compared to motile cells. A likely hypothesis is that *P. aeruginosa* (and other motile bacteria) are able to attach within smaller apertures (relative to their diameters) than nonmotile cells.

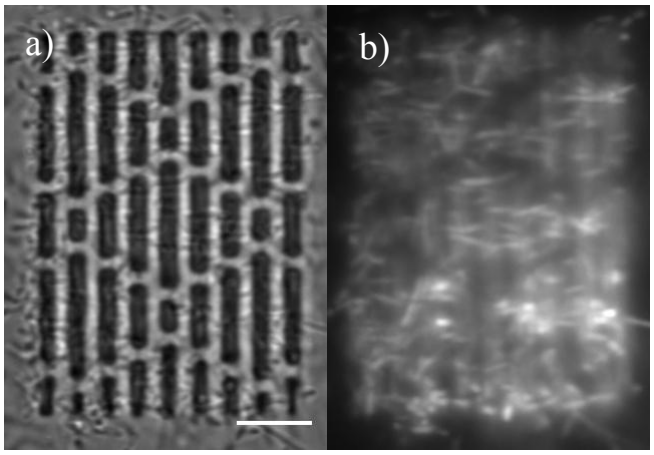


Figure 2.10: PA14 attachment to the tops of 3-µm-tall rectangular features. Differential interference contrast (DIC) (a) and widefield fluorescence (b) images show cell attachment after 42.5 hrs under flow. These features were spaced 2-µm apart, but cells attached across features for all structural variations tested in this experiment. *Note: the dark background around the structure of (b) is due to the focus being ~ 3 µm off the surface; that is, cells were also attached heavily to the glass. Scale bar = 10 µm.

Another observation made during this experiment was that cell attachment appeared to be lower on the tops of features with alternating heights than on the tops of features with the same heights (data not shown). This effect appeared to be more pronounced for features spaced 1- and 0.5-µm apart than for features spaced 2-µm apart. However, this result may originate from the way in which images were acquired – with images taken focused on the coverglass and on feature tops. Since the structures themselves had strong signals, images acquired on the top of structures with alternating feature heights had dark regions corresponding to 3-µm-tall feature heights. A better way to conduct this experiment would be to acquire image stacks by taking defined vertical steps throughout the structure. Methods to increase signal-to-noise of the cells, such as reducing structure fluorescence by photobleaching, would also be advantageous for

widefield fluorescence. Additionally, imaging of individual structures required several hours for each time point, during which attachment levels may have changed. Consequently, there were no quantitative analyses made of overall cell attachment levels to the various structures in this experiment.

One of the greatest limitations of this experiment was that topographical areas were limited to ~ 50 μm × 30 μm per structure. While multiple structures were fabricated and imaged, this was not an effective method for assessing biofilm development in response to topography. Although cell attachment occurs over areas corresponding to the dimensions of a single cell, biofilm formation occurs over areas with diameters of tens to hundreds of microns. For example, *P. aeruginosa* cells form tall mushroom-like biofilms (in some cases greater than 100 μm high) over extensive areas in flowing media [20, 21]. Additionally, statistical variations in cell numbers attached to surfaces require assessment of bacterial attachment over extended regions. Consequently, for much of the work in this thesis, individual protein-based structures were stitched together to form topographical surfaces over larger areas.

### 2.4.2 Large-Area (Stitched) Structures

To assess biofilm formation in response to variations of Sharklet topographies, structures were stitched together over areas up to ~ 0.15 $mm^2$ from single structures with areas of ~ 1500 $\mu m^2$. By moving a motorized stage with a joystick, structures were fabricated one at a time to create the desired topographical pattern over a relatively large surface area (Figure 2.11). Masks were designed to maximize fabrication in the optimal scan area (~ 35 μm × 48 μm for this experiment) while still maintaining robust features. Structures were fabricated with a 100×/1.3 NA objective rather than a 40×/1.3 NA

objective. The 40×/1.3 NA objective facilitated fabrication over larger areas but decreased radial (in plane) resolution.

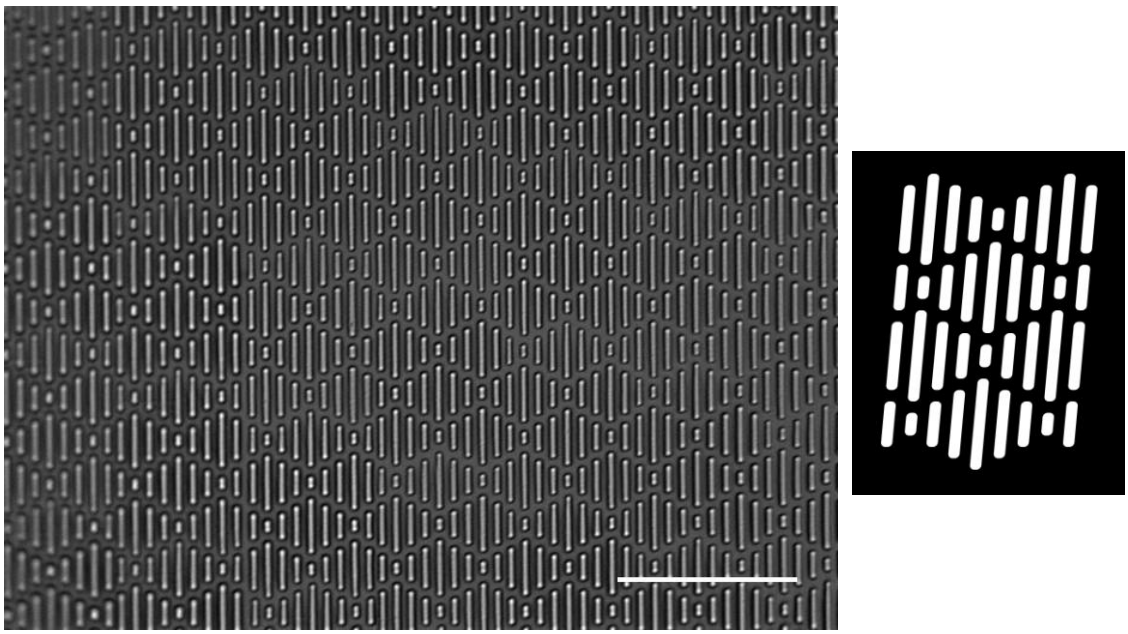

Figure 2.11: A stitched topographical surface. Structures were stitched into a larger topography by fabricating one structure, moving the stage with a joystick, and fabricating another structure in a position that maintained the desired topographical pattern. The stage position was located by placing a digital arrow within a live-image window on a computer monitor corresponding to a specific location on a fabricated structure. The black-and-white mask (right) was used to fabricate individual structures that were stitched together to form the Sharklet topography shown in the DIC image (left). The mask has a ~ 5° skew to correct for reflection geometries off the DMD mirrors. Scale bar = 50 μm.

In one particular experiment, four topographical surfaces were fabricated in two chambers of a flow cell (Figure 2.12). One surface was a smooth control structure, while the other three were Sharklet structures with different-sized spaces between features (2, 1, and 0.5 μm) (Figure 2.13). Commercial Sharklet has features spaced 2 μm apart, but feature spacings of 1 and 0.5 μm were also tested since these dimensions are relevant to

diameters of PA14 cells (~ 0.5 to 0.8 μm) and other clinically-isolated bacteria (e.g. *S. aureus* are spherical with diameters ~ 1 μm and under). Feature heights were ~ 3 μm.

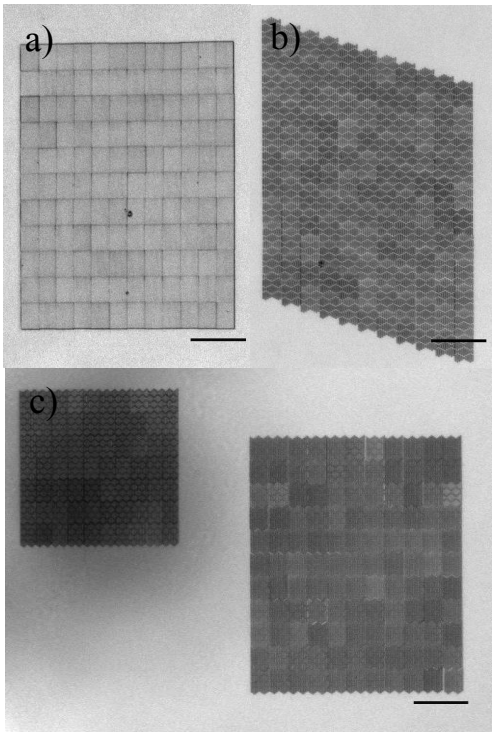


Figure 2.12: Stitched structures in a flow cell pre-inoculation with cells. Control (a) and Sharklet (b) topographies were in one flow cell chamber, while Sharklet topographies with 1-μm and 0.5-μm spaces between features (c, right and left, respectively) were fabricated in another flow cell chamber. Fabrication time for all 4 structures was greater than 12 hrs; the structures in the second flow cell (c) were not fabricated to full size due to human fatigue. Scale bars = 100 μm.

Structures were inoculated in a flow cell with mid-log phase PA14 gfp-expressing cells in 1/3 TSB with 1 mM glucose. Flow was started within 1 hr post-inoculation at a rate of 50 μL $min^{-1}$. Structures with cells were imaged by confocal microscopy 48 hrs

post-inoculation (Figure 2.14) and then dehydrated and fixed for imaging by SEM (Figure 2.15).

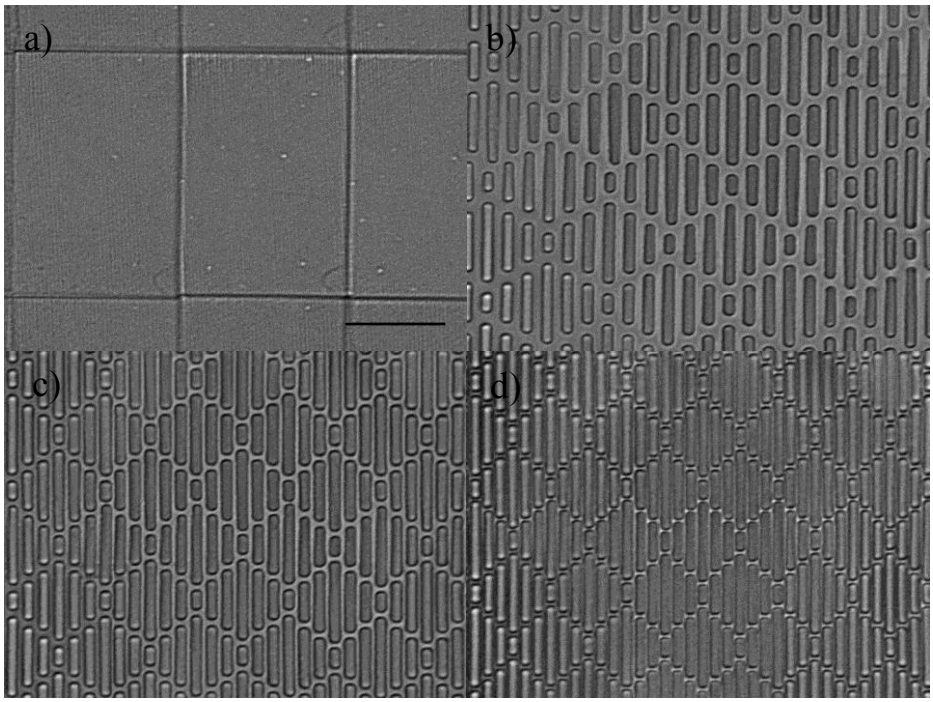


Figure 2.13: Higher-magnification DIC images of stitched structures. Topographical surfaces shown are control (a), Sharklet (b), Sharklet with 1-µm spaces between features (c), and Sharklet with 0.5-µm spaces between features (d). Scale bar = 20 µm.

After 48 hrs of incubation under flow with PA14, the levels of punctate fluorescence (on size scales of bacteria) were highest for the control surface, followed by Sharklet. The lowest level of punctate fluorescence (on size scales of bacteria) was on Sharklet with 0.5-µm spaces between features, with a slightly higher level on Sharklet with 1-µm spaces between features (Figure 2.14). The results seemed to indicate that the control surface had the highest level of PA14 cell attachment, followed by Sharklet. The lowest PA14 attachment levels seemed to be on Sharklet with features spaced apart by

0.5 μm, with slightly higher levels of attachment on features spaced apart by 1 μm. The arrangement of cells on the control surface was indicative of a large mushroom biofilm (Figure 2.14a). *P. aeruginosa* mushroom biofilms are complex communities of cells with nonmotile populations that form the "stalk" and motile populations that form the mushroom "cap" [20]. The three topographies with Sharklet features showed much smaller aggregations of cells relative to the large-area mushroom biofilm that covered a substantial region of the control surface.

The SEM data supported the results of the confocal microscopy images, with bacterial attachment levels highest on the control surface, followed by Sharklet, with the lowest attachment levels on Sharklet with 1-μm feature spaces and Sharklet with 0.5-μm feature spaces (Figure 2.15). Dehydration caused the mushroom biofilm to flatten on the control surface and Sharklet features to lose integrity.

While this experiment appeared to show differences in PA14 attachment levels for four different topographical surfaces, it was not repeated and there are questions regarding potential effects of light scattering produced during imaging by confocal microscopy. Future directions for this work would involve conducting reproducible experiments to test hypotheses based on using features (Sharklet and otherwise) with different spacings. One set of hypotheses might involve how cell orientation between topographical features influences biofilm formation. For example, some surfaces might promote "reversible" attachment orientations between features while others might promote "irreversible" attachment orientations between features. The heights of topographical features might also be interesting to vary, since these could potentially influence bacterial communication behaviors. Modulation of feature sizes, geometries, and spacings could produce an array of interesting studies on bacterial attachment behaviors.

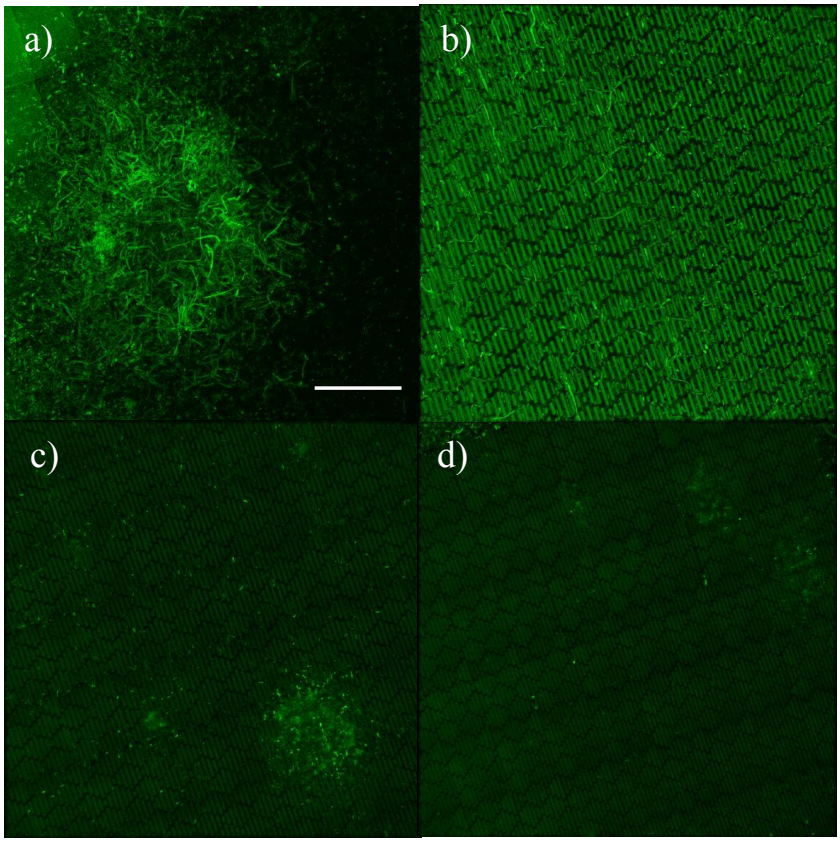


Figure 2.14: PA14 attachment on Sharklet topographies with spaces of different sizes between features. These are maximum intensity projection images of confocal microscopy image stacks acquired 48 hrs post-inoculation under flow. The levels of punctate fluorescence (on size scales of bacteria) seemed to indicate differential levels of PA14 attachment. The arrangement of cells on the control surface was indicative of a large mushroom biofilm (a). The data also seemed to indicate heavy PA14 attachment on the Sharklet topography (b), but there was no formation of a mushroom biofilm. The data seemed to indicate that the lowest level of PA14 attachment was on the Sharklet topography with feature spaces of 0.5-µm (d), with a slightly higher level for the surface with features spaced apart by 1-µm (c). Cells attached to the coverglass are visible in the upper left and right corners of (d), where the edge of the structure met the coverglass. Scale bar = 50 µm.

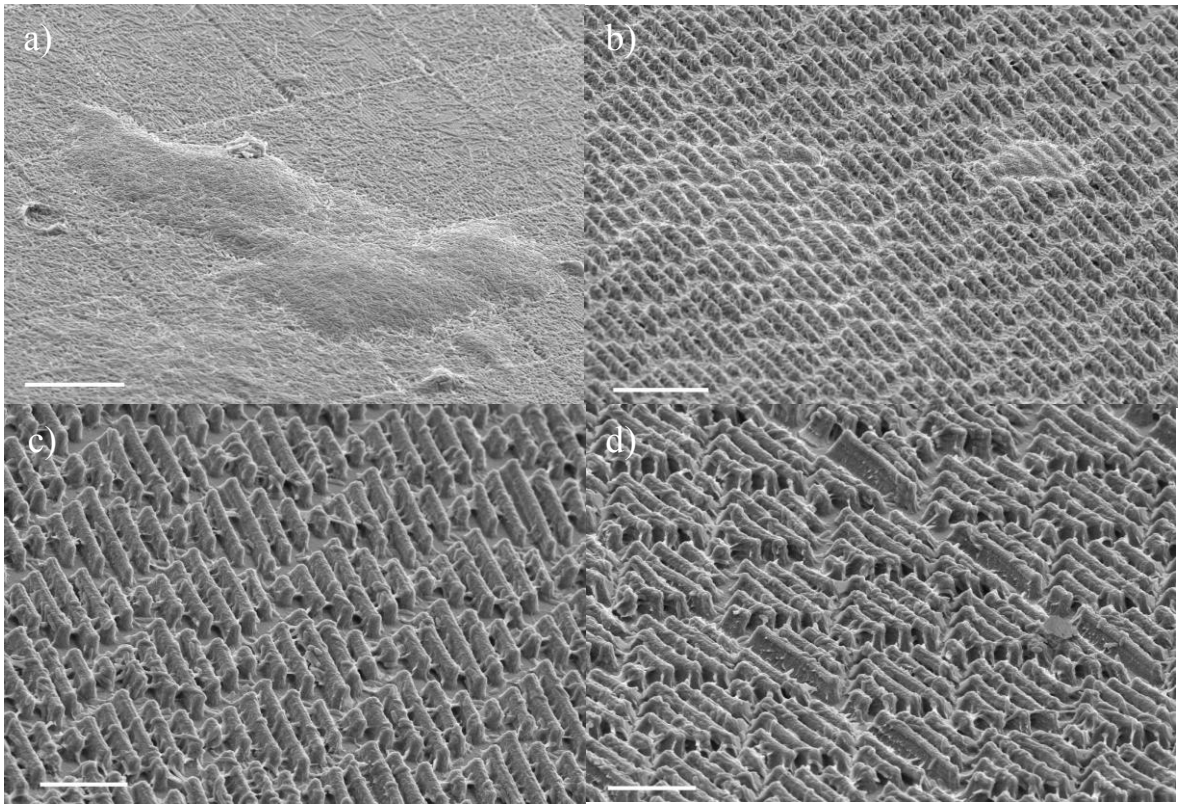


Figure 2.15: SEM images of PA14 cells on stitched structures. Structures with attached cells were dehydrated and fixed following confocal microscopy imaging 48 hrs post-inoculation in a flow cell (Figure 2.14). PA14 attachment was heaviest on the control structure (a), which had a large mushroom biofilm that was flattened by dehydration. The Sharklet structure also had a heavy level of attachment (b). Sharklet structures with 1-µm spaces between features (c) and 0.5-µm spaces between features (d) had the lowest attachment levels. Scale bars = 20 µm for (a) and (b) and 10 µm for (c) and (d).

One of the greatest challenges of this experiment was the amount of time required for fabrication of surfaces over such a large area – greater than 12 hrs for all 4 surfaces. Due to human fatigue, the Sharklet topographies with 1- and 0.5-µm spaces were not fabricated to sizes as large as the control and Sharklet structures. It is not known what, if

any, impact this inconsistency had on results. Automation of the stitching technology would greatly enhance experimental throughput and allow testing of a larger number of topographical surfaces. Finally, since this experiment, some topographical surfaces tested have been found to cause scattering of light during imaging by confocal microscopy that has made detection of bacteria difficult, a topic that will be discussed with the relevant topographies in Chapter 3. Future work based on the present topographical designs and all other designs requires an assessment of light scattering caused by the surfaces, especially if confocal microscopy or another technique highly-prone to scattering interferences is used to detect bacteria.

## 2.5 TOPOGRAPHIES BASED ON MATHEMATICAL FUNCTIONS

One way to systematically alter surface topographies for influencing bacterial attachment is by designing surfaces based on mathematical functions, such as sine waves. For a sine wave on the size scale of bacteria, it might be logical to start with a 1-μm-amplitude, which requires using vertical step sizes (e.g., 0.1 μm) much smaller than the fabrication voxel in the z-dimension (~ 1 μm). This limitation is somewhat overcome by using a motorized z-stepper to control the fine focus of the microscope in conjunction with a mask presentation program. In this configuration, successive layers are added to the top of the structure with z-dimensions corresponding to the specified step sizes. Examples of structures with step sizes of 0.1 through 0.5 μm are shown in Figure 2.16; structures were resolved with all 5 step sizes. Figure 2.16(b) shows a structure with a base layer having a larger z-dimension than the specified step size (0.3 μm). This likely occurred due to the focus being close to the coverglass at the start of fabrication so that the first layer was fabricated with a large portion of the fabrication voxel above the coverglass. The structures in 2.16(c) and (d) have base layers that appear to be more

similar to the other layers of the structure, so focus was likely below the coverglass at the start of fabrication of these structures.

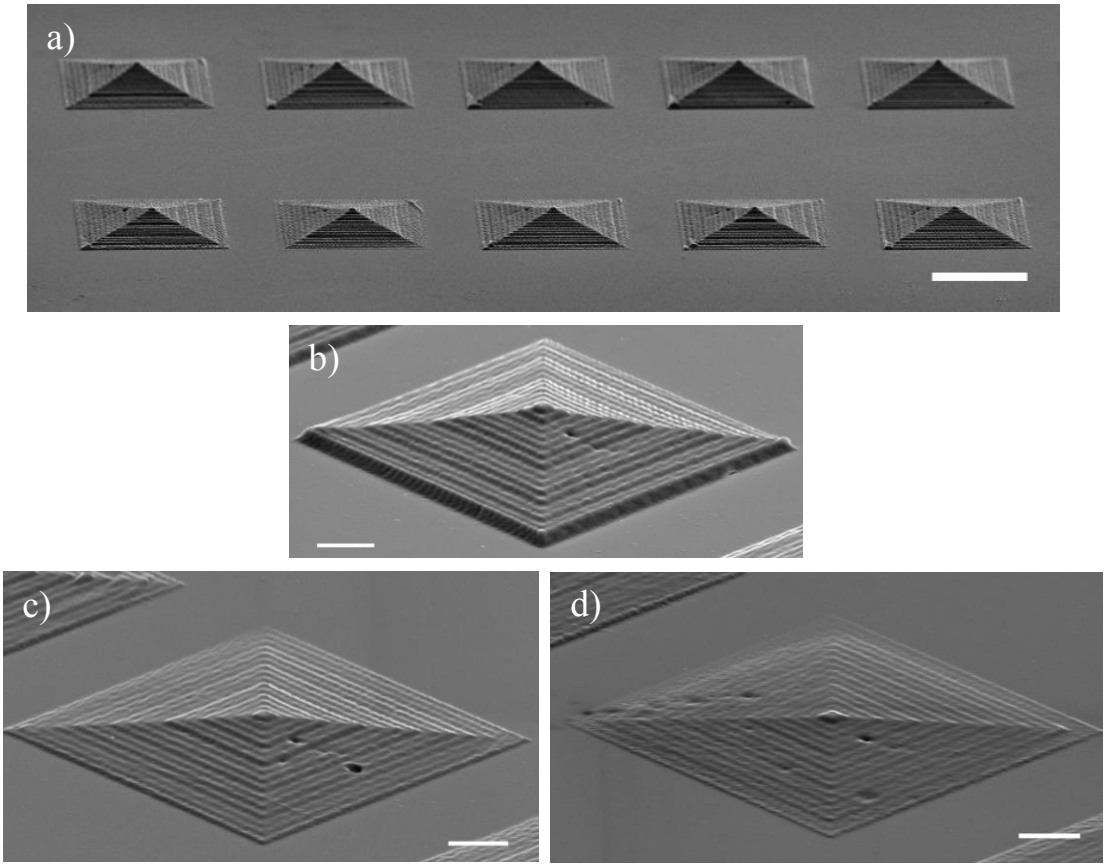


Figure 2.16: Square pyramids fabricated with a range of step sizes shown in SEM images. To illustrate fabrication with step sizes smaller than the axial resolution of the fabrication voxel (~ 1 μm), square pyramids were fabricated with step sizes of 0.5 μm (a) top row, 0.4 μm (a) bottom row, 0.3 μm (b), 0.2 μm (c), and 0.1 μm (d). Scale bars = 20 μm (a) and 5 μm (b) through (d).

Using 0.1-μm step sizes, several topographical surfaces based on mathematical functions, such as sine waves, were designed by using Powershape-e CAD software and Adobe Photoshop batch-processing for creating masks (Figure 2.17). Structures were qualitatively reproducible despite the element of human error involved in setting the fine

focus prior to fabrication of each structure (Figure 2.18). However, it was difficult to ascertain how closely structures were adhering to mask designs during the fabrication process, since BSA structures shrink during the dehydration step required for SEM preparation (Figure 2.19).

Topographies shown in Figure 2.17 were tested under flow with PA14 cells and imaged with widefield fluorescence over several time points (data not shown) However, even with replicates, total structure areas were too small to discern possible effects on attachment, given typical statistical variations in cell attachment over surfaces. To generate meaningful results, structures would need to be stitched together over larger areas.

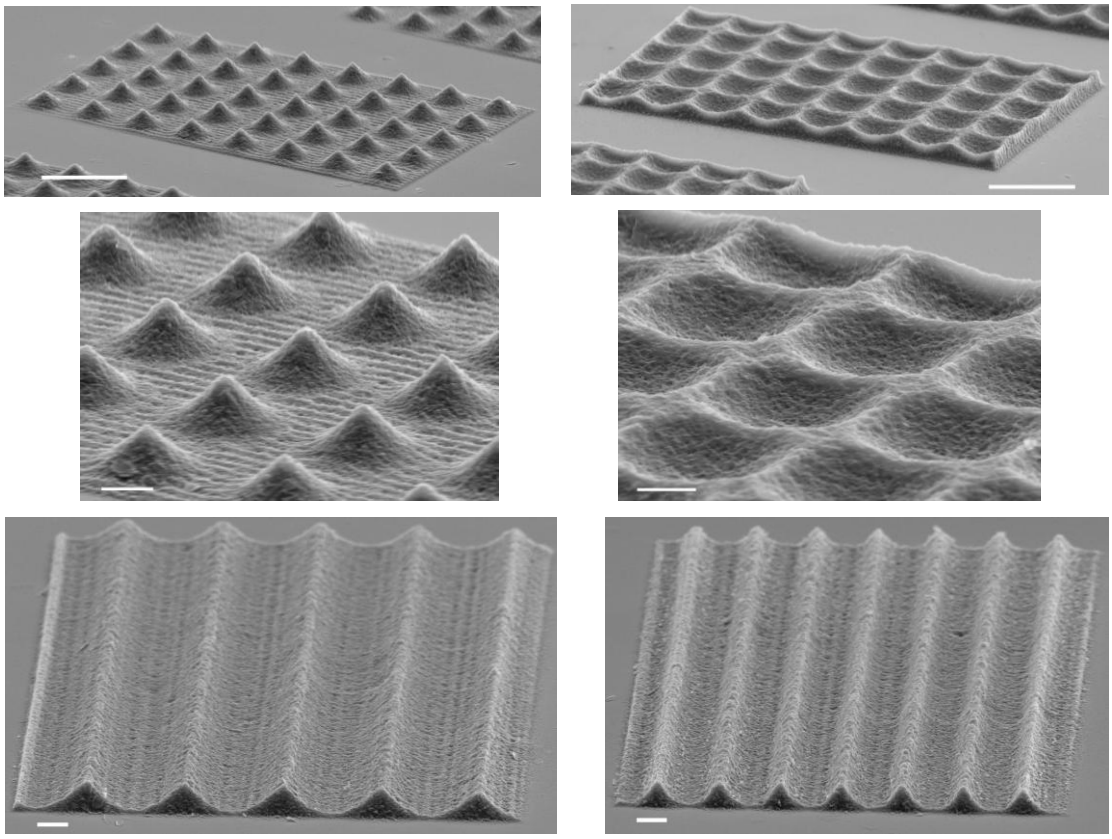

Figure 2.17: SEM images of topographical surfaces based on mathematical functions designed using CAD software. Scale bar = 10 μm (top row) and 2 μm (middle and bottom rows).

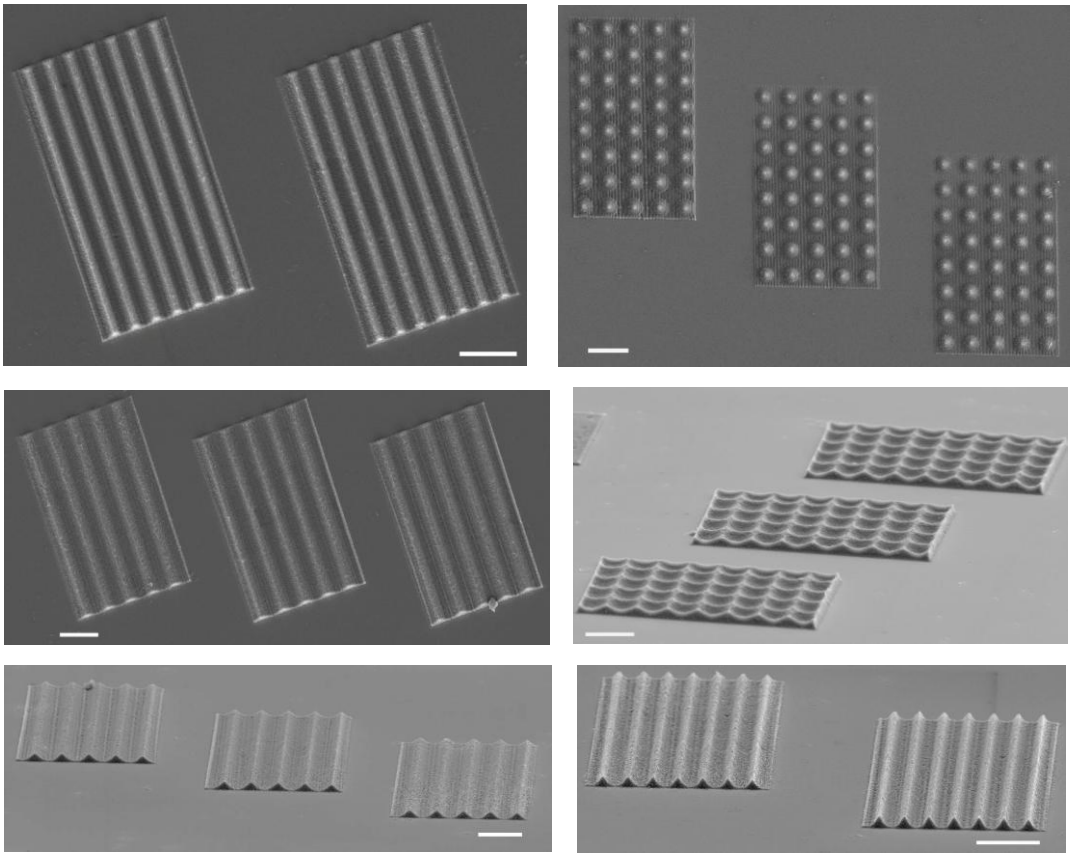

Figure 2.18: Replicates of surfaces. Scale bars = 10 μm.

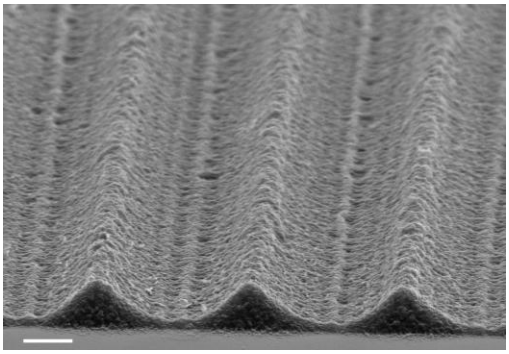

Figure 2.19: Magnified SEM image of a dehydrated sine wave surface. BSA structures are hydrogels, so they shrink considerably in the dehydration process necessary for SEM preparation. This made it difficult to determine how closely structures, immediately after fabrication, conformed to the mathematical functions used in mask designs. Scale bar = 2 μm.

## 2.6 PILLAR TOPOGRAPHIES

### 2.6.1 Experimental Methods

A simplified attachment assay was used for this set of experiments, since it was a more efficient method than the flow cell assays, which are time-consuming and prone to contamination. Furthermore, static assays are often used in bacterial attachment studies to complement flow cell assays. It should be noted that PA14 behaves differently in a static environment with one of the largest differences being that they do not develop the large mushroom biofilms that form under flow.

More detailed experimental methods for fabrication and cell growth were described in Chapter 1. For these experiments, structures were fabricated to dimensions of ~ 200 μm × 200 μm to 400 μm × 400 μm on No. 1 coverglass with an attached 8-chambered polystyrene well device (Lab-Tek). Following fabrication, structures were rinsed with copious amounts of buffer in a laminar flow hood followed by extended time in buffer (overnight and longer) to further rinse structures. For the experiment shown in Figure 2.23, structures were photobleached by reflecting the output of a mercury lamp off a 90/10 mirror into the back aperture of a 40×/0.75 NA objective (Zeiss). Prior to inoculation with cells, structures were pre-conditioned with media (1/3 TSB with 1 mM glucose) for 1 to 12 hours. Just prior to inoculation, PA14 cells were diluted from a mid-log phase culture to either 0.1 or 0.01 as specified in experimental discussions. Buffer was removed from structures and immediately replaced with 200 μL of cells. (The wells were able to hold between 200 μL and 600 μL). The solution volume was kept to a minimum to allow as much oxygen as possible to reach cells). The Lab-Tek device containing structures and cells was maintained at 28 to 30 °C for 24 hrs. After 24 hrs, structures were rinsed 5 times by successively adding and removing 400 μL of fresh

media to the 200 µL of media already in the well just prior to imaging with confocal scanning laser microscopy.

### 2.6.2 Basic Pillar Topographies

By reducing the sizes of spaces between Sharklet features, PA14 attachment appeared to be reduced relative to control and Sharklet surfaces. Based on these results, topographies were designed with pillars spaced < 0.5 µm apart (Figure 2.20). It was hypothesized that pillars spaced so closely together would reduce PA14 attachment between features relative to those spaced farther apart. Pillars were also fabricated with small dimensions of 2 µm × 4 µm since it was thought that this would reduce attachment to pillar tops relative to larger pillars. Pillars were offset, rather than aligned, since this configuration reduced interstitial space between features.

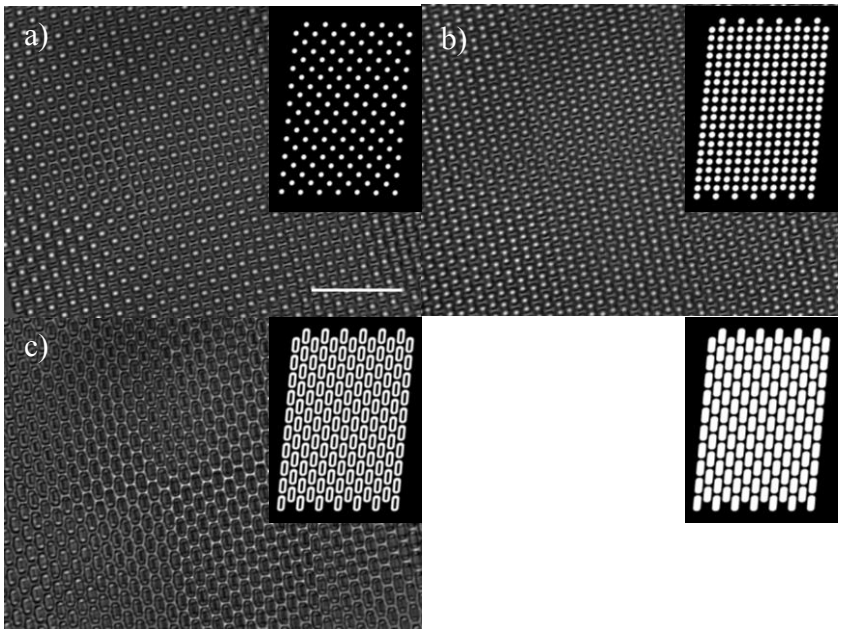


Figure 2.20: Three prototypes to reduce PA14 attachment. For all three prototypes, the mask on the bottom right was used to create a 3-µm-tall base of pillars with dimensions of 2 µm × 4 µm. The masks shown with the three images of structures were used to create 2-µm-tall features atop the pillars. Fabrication step sizes were 0.3 µm. Scale bar = 20 µm.

In initial experiments, small features, such as one or two cylinders (Figure 2.20a and 2.20b, respectively) or oval rings (Figure 2.20c) were placed atop pillars to try to hinder PA14 attachment to feature tops. The effects of these small features on PA14 attachment were never assessed, and the topography shown in Figure 2.20c was chosen arbitrarily for the experiment that generated the results shown in Figure 2.21.

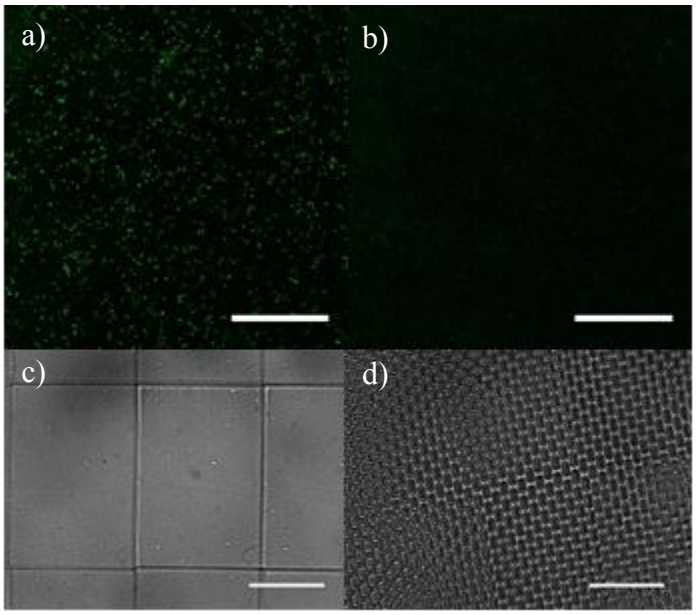


Figure 2.21: PA14 attachment on control and pillar topographies. Cells were inoculated at 0.1 $OD_{600}$ and rinsed frequently throughout the 24-hr attachment period. Confocal fluorescence images of gfp-expressing PA14 cells attached to surfaces showed much higher levels of punctate fluorescence on a control surface (a) relative to an experimental surface (b). This seemed to be indicative of higher levels of bacterial attachment to the control surface relative to the pillar surface. DIC images show control (c) and experimental (d) structures prior to inoculation. The experimental structure was the topography in the bottom row of Figure 2.20. Scale bars = 50 μm ((a) and (b)) and 20 μm ((c) and (d)).

Confocal images acquired 24 hrs post-inoculation showed much higher levels of punctate fluorescence on a control surface relative to a pillar surface (Figure 2.21a and

2.21b, respectively). This seemed to indicate that the control surface had a higher level of PA14 attachment relative to the pillar surface. The images shown are confocal slices atop the surfaces, so 2.21b does not show the cells that were attached between pillars. The sampling resolution (x-y voxel = 0.47 μm) was generally not high enough to resolve the short axis of PA14 cells, which have diameters of 0.5 to 0.8 μm. Since it was desired to observe attachment orientations of cells (e.g., those between pillars) in addition to detecting them, higher sampling resolutions (x-y = 0.23 μm) were used in subsequent experiments. This allowed for better resolution of cells while still imaging over areas large enough (~ 120 μm)$^2$ to assess overall attachment levels.

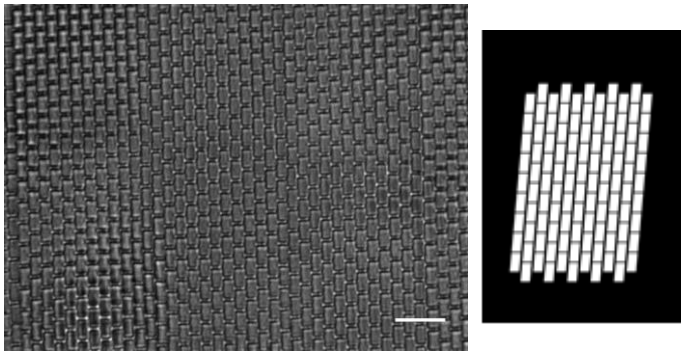

Figure 2.22: Mask and DIC image of modified pillar structure. Pillars were modified to have sharp, rather than rounded, rectangular edges (although the edges of the fabricated structures were not as sharp as those in the mask.) The modification was intended to reduce cell attachment between features. Scale bar = 20 μm.

Since the pillar topography seemed to cause such a large reduction in PA14 attachment relative to the control surface, it was hypothesized that the small features atop the pillars likely had comparatively small effects. Therefore, the small features were removed, and solid pillars were fabricated to a height of ~ 5 μm. Instead of rounded rectangular edges, edges were made to be sharp to reduce the interstitial space between

three adjacent pillars (Figure 2.22). It was hypothesized that this would also reduce PA14 attachment levels in the interstitial spaces. The final change made was to reduce the distance between pillars from ~ 0.5 μm to ~ 0.2 μm.

PA14 attachment to the modified pillars and a control surface is shown in Figure 2.23. By increasing the x-y voxel resolution during confocal imaging, there was much better resolution of bacterial cells relative to the images shown in Figure 2.21. As in the previous experiment, far higher levels of punctate fluorescence (on size scales of bacteria) were observed on the control surface relative to the top of the pillar surface (Figure 2.23 (a) and (c), respectively). This seemed to indicate much higher levels of PA14 attachment on the control surface relative to the top of the pillar surface. Within pillars, punctate fluorescent areas with dimensions corresponding to the short axis of a PA14 cell indicated that cells were oriented orthogonally to the coverglass (Figure 2.23b). Furthermore, the combined levels of punctate fluorescence (on size scales of bacteria) within and atop the pillars was much lower than the control surface, which seemed to indicate an overall level of PA14 attachment within and atop the pillar surface that was much lower than the control surface. One word of caution here is that there may have been some bacteria that were not detected due to light scattering caused by the topographical surface itself – a topic that was introduced in section 2.4.2 and will be addressed further in Chapter 3. The degree of scattering caused by the pillar topographies, if any, has not been assessed and should be for future work.

Within pillars, PA14 cells were confined to interstitial spaces bounded by three adjacent pillars (Figure 2.24). Their confinement seems to have been induced by the presence of crosslinked protein between pillars that resulted from incomplete resolution of pillars during fabrication. The crosslinked protein between pillars is shown in the DIC image in Figure 2.24 and the SEM images in Figure 2.27.

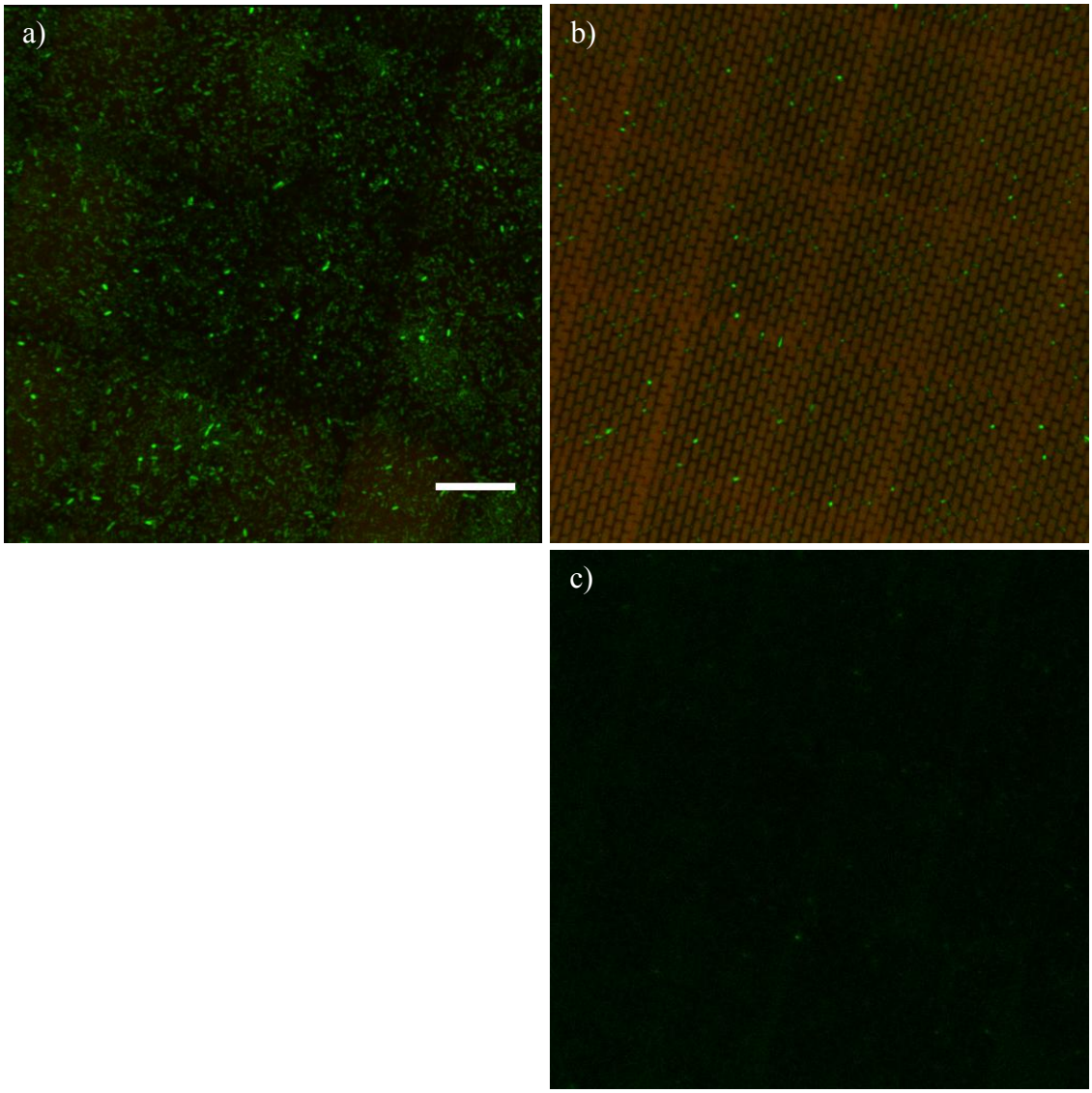


Figure 2.23: PA14 cells attached within and atop pillars and to a control surface. Confocal maximum intensity projection images show PA14 cells attached to a control surface (a) and within pillars (b). Cells appear green and structures reddish brown due to overlaying of the green and red channels. The image in (c) is a confocal slice acquired just above the pillars in the green channel. Scale bar = 20 μm.

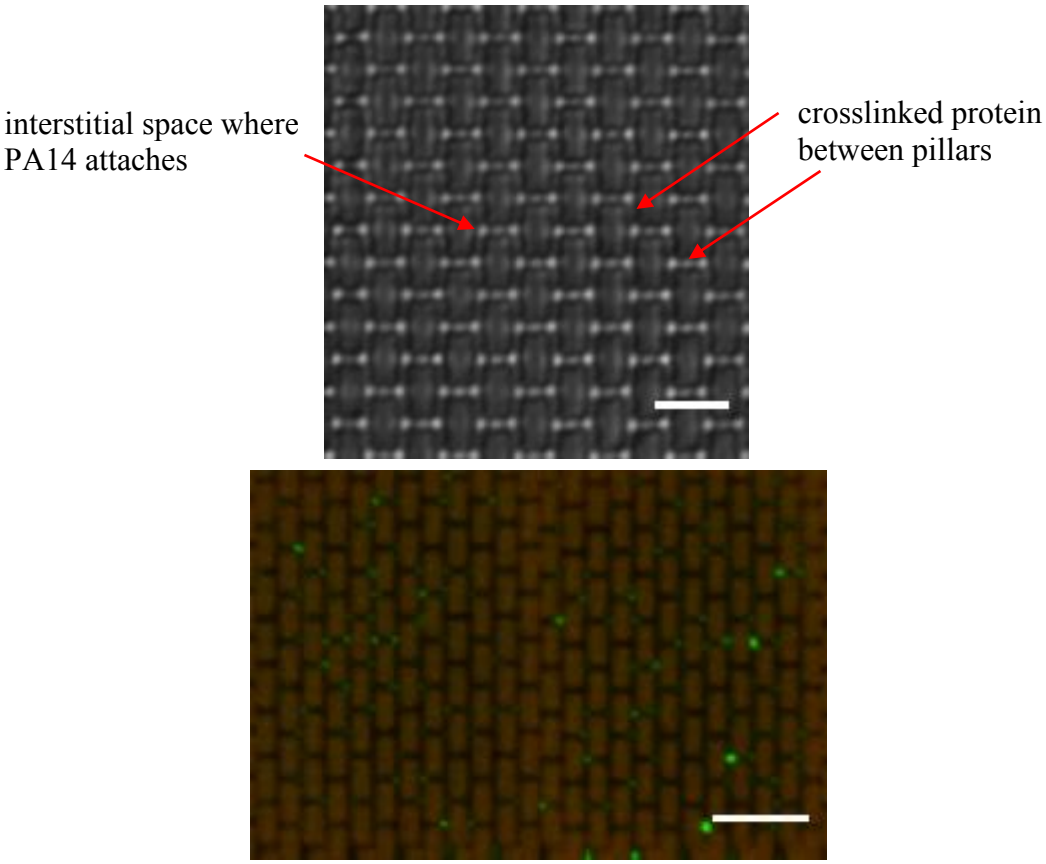


Figure 2.24: Interstitial spaces between pillars where PA14 attaches. The top image is a DIC image of a pillar surface without cells. It shows that there are 6 apertures around each pillar that can accommodate PA14 cells. All other regions around pillars are partially filled with crosslinked protein due to incomplete resolution of feature boundaries in the fabrication step. In the bottom image, PA14 cells are shown to be attached within the interstitial spaces between 3 adjacent pillars. The image is a confocal maximum intensity projection image in which cells appear green while structures appear reddish brown due to overlay of the green and red channels. The rounded appearance of the cells indicates attachment orientations that are orthogonal to the underlying coverglass (i.e., cells are attached by their poles). Scale bars = 5 μm.

To try to reduce PA14 attachment between pillars, pillars were redesigned to have different geometries (Figures 2.25 and 2.26). For the three topographies shown in Figure 2.25, PA14 attachment seemed to be slightly higher between features for the basic pillar design (2.24a) relative to the other two designs (data not shown). However, pillars with reduced attachment levels between features seemed to have higher attachment levels above features (e.g., Figure 2.26). In this experiment, PA14 attachment seemed to be much lower between pillar features modified by careful mask design (2.26b, left), but cells attached more heavily to pillar tops (2.26b, right). It should be noted that mask design required prototyping to achieve desired features – in this instance, those features that would reduce the interstitial space between three adjacent pillars.

SEM images were acquired of pillars without cells (Figure 2.27). The pillars used in the present studies partially collapsed and shifted during the dehydration process (Figure 2.27 a through d), so pillars spaced farther apart were also imaged (Figure 2.27 e through g). As shown in DIC imaging (Figure 2.24) and SEM images, pillars spaced closely together had crosslinked protein between them that caused them to lose structural integrity upon dehydration, while pillars spaced farther apart maintained structural integrity due to the absence of crosslinked protein between features.

It was found during the course of these experiments that it was difficult to prevent PA14 attachment between features. Since PA14 have small diameters (~ 0.5 to 0.8 μm), they are able to swim into submicron apertures, as discussed in section 2.3. In this set of experiments, one challenge was to reduce PA14 attachment between and atop features. More systematic studies and replicates are needed to address this issue, along with scattering and bacterial quantification challenges.

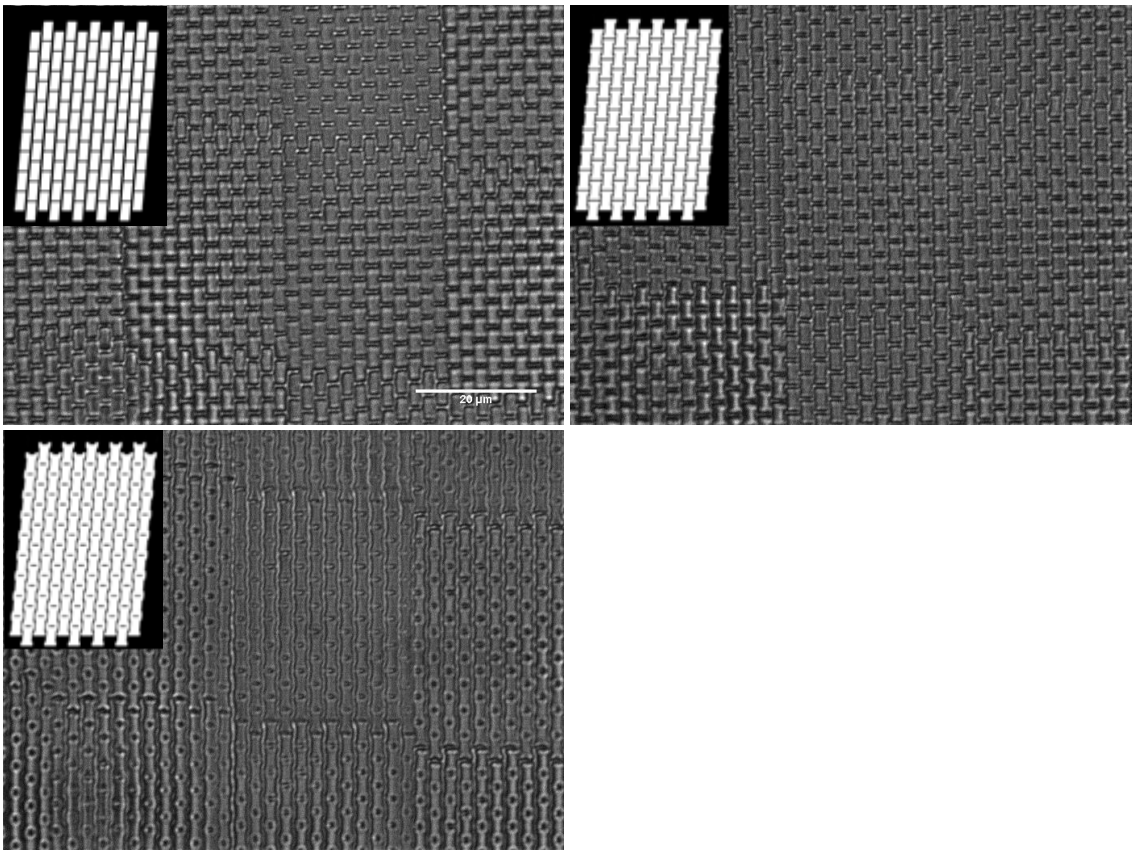


Figure 2.25: Pillar designs for reducing PA14 attachment between pillars. The upper left image shows basic pillars, while the upper right and lower left images show pillars modified to try to reduce PA14 attachment in the interstitial spaces within three adjacent pillars. Scale bar = 20 µm.

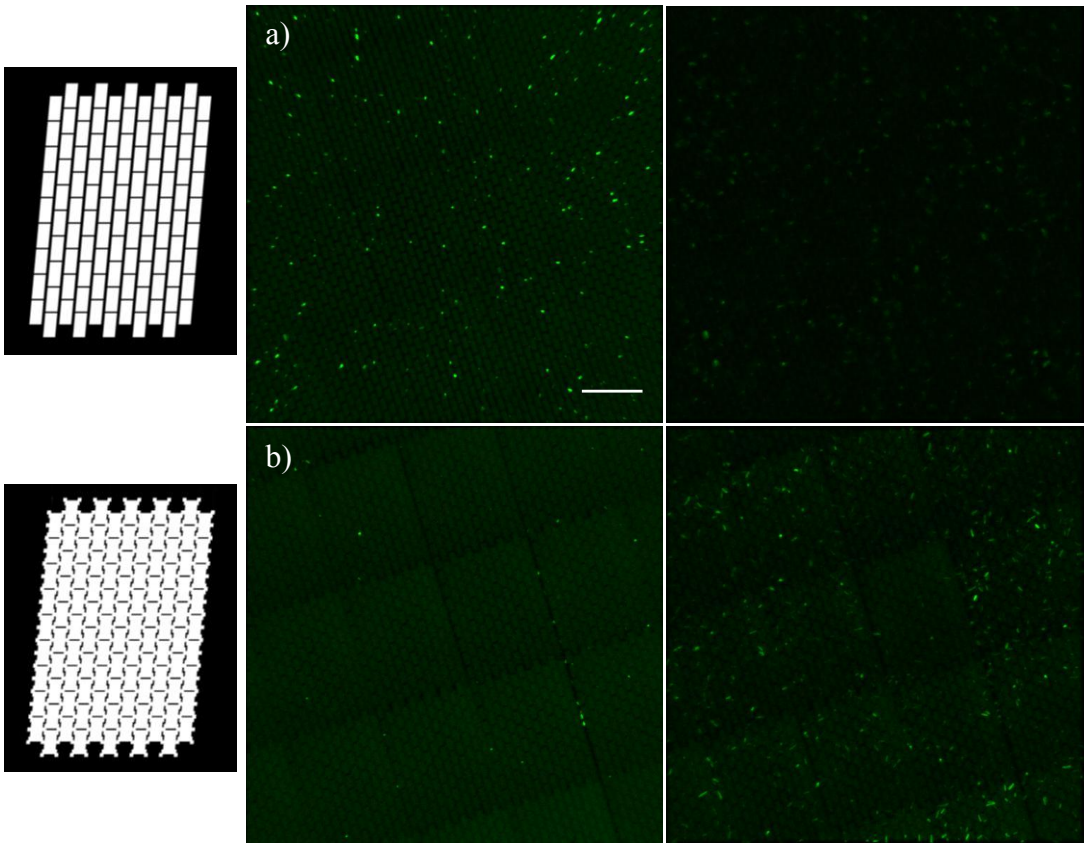


Figure 2.26: PA14 attachment on pillars with different shapes. The basic pillar design (a) was modified to reduce PA14 attachment between pillars (b). The black-and-white masks used to fabricate structures are shown to the left of the respective images. Confocal maximum intensity projection images are shown for PA14 attachment. The left-hand images show attachment between pillars, while the right-hand images show attachment atop pillars. The basic pillar topography (a) seemed to show higher levels of PA14 attachment within pillars (a, left) relative to the modified pillar topography (b, left). However, there seemed to be an increase in PA14 attachment to the tops of the modified pillars (b, right) relative to the basic pillars (a, right). The inoculation $OD_{600}$ was 0.01. Scale bar = 20 μm.

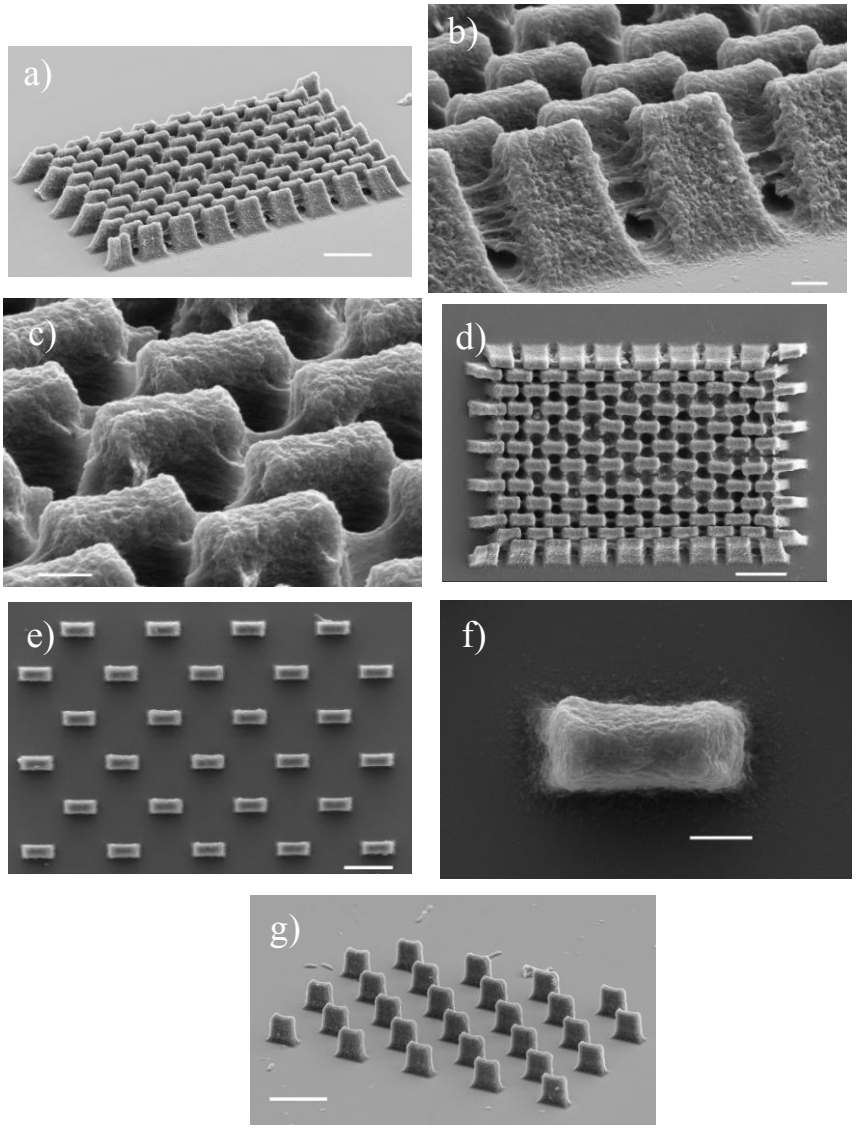


Figure 2.27: SEM images of pillar topographies. Images (a) through (d) show closely-spaced pillars (< 0.5 μm apart) used for bacterial attachment studies. In agreement with DIC images, pillars had crosslinked protein between them, indicating incomplete resolution of feature boundaries during fabrication that caused pillars to collapse and shift in the dehydration process. By contrast, pillars spaced farther apart ((e) through (f)) did not have crosslinked protein between them, so they maintained structural integrity. Scale bars = 10 μm ((a), (d), and (g)), 5 μm (e), and 1 μm ((b), (c), and (f)).

### 2.6.3 Area-Gradients of Pillars

The data seemed to indicate that PA14 attachment was minimal atop pillars with dimensions of 2 μm × 4 μm, so a logical step was to increase the surface area of pillars until attachment became heavy. For this study, pillars of various sizes were fabricated along with topographies in which alternating rows of pillars were connected (Figure 2.28). The idea behind connecting alternate rows of pillars was to determine if cells would attach to features with a small width in one dimension but a much longer length in the other dimension. A study like this could also be very interesting under flow to see how biofilm formation is influenced as the surface area of topographical features is progressively increased in various dimensions.

The results of this study showed increasing levels of punctate fluorescence to pillar tops as surface area of pillars increased (Figure 2.28). This seemed to indicate corresponding increases in PA14 attachment levels. Another trend seemed to be that PA14 attachment between pillars decreased when alternate rows of pillars were connected, a result that makes sense in relation to the available number of interstitial spaces. One observation that was particularly interesting was that punctate fluorescence levels seemed to increase to a greater extent in connecting pillars of dimensions of 4 μm × 4 μm relative to connecting pillars of dimensions 2 μm × 4 μm. This seemed to indicate a larger increase in PA14 attachment levels in connecting the larger pillars relative to the smaller pillars. One peculiar result was that there was a very low level of punctate fluorescence (indicative of cell attachment) between pillars with dimensions of 8 μm × 8 μm. No hypotheses have been developed at this time to explain this most unusual result, which did not occur in a separate replicate. All other attachment trends were similar to those shown in the present experiment.

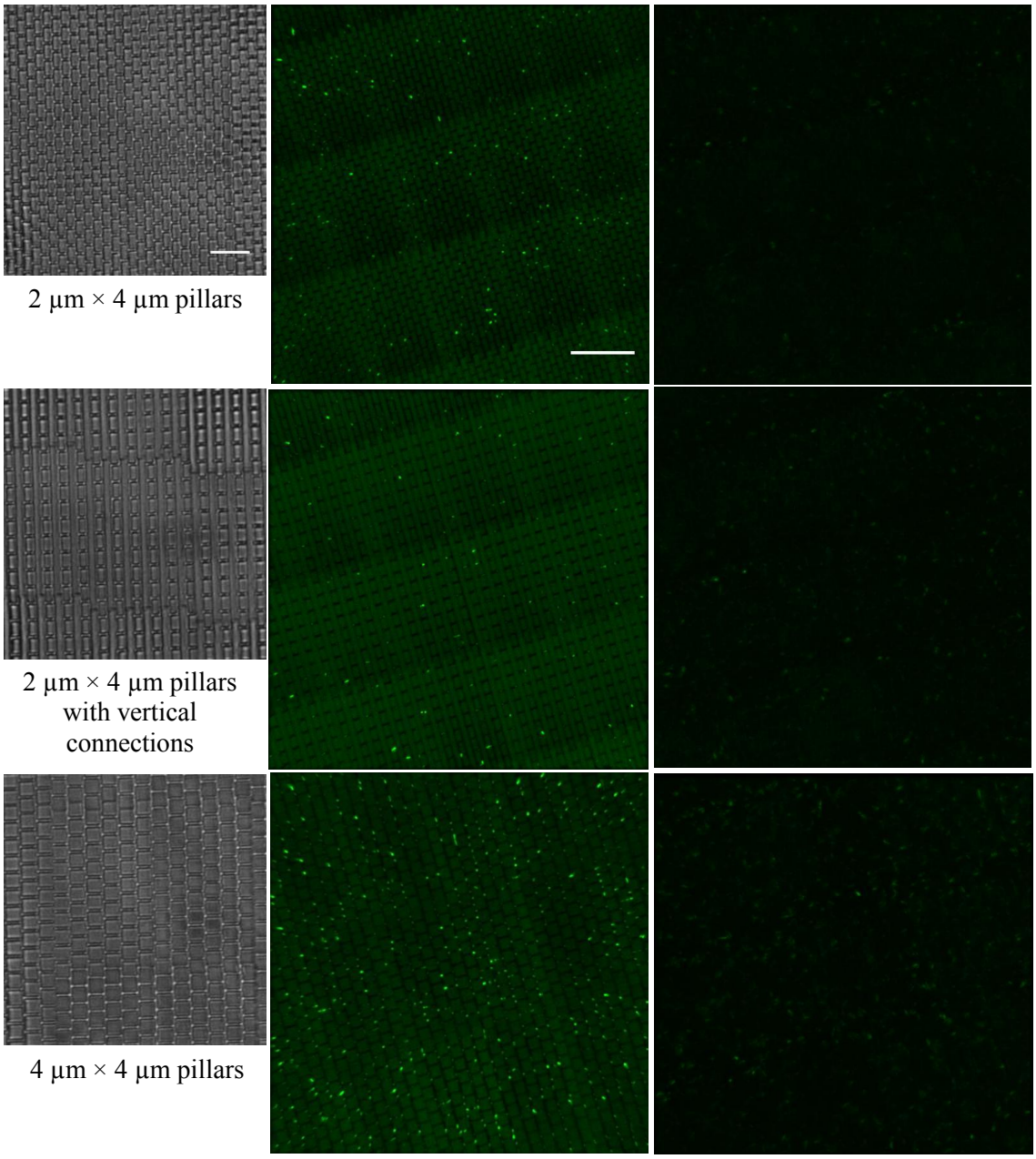


Figure 2.28: PA14 attachment to pillars with progressively increasing surface areas. *(cont. on the next page)*

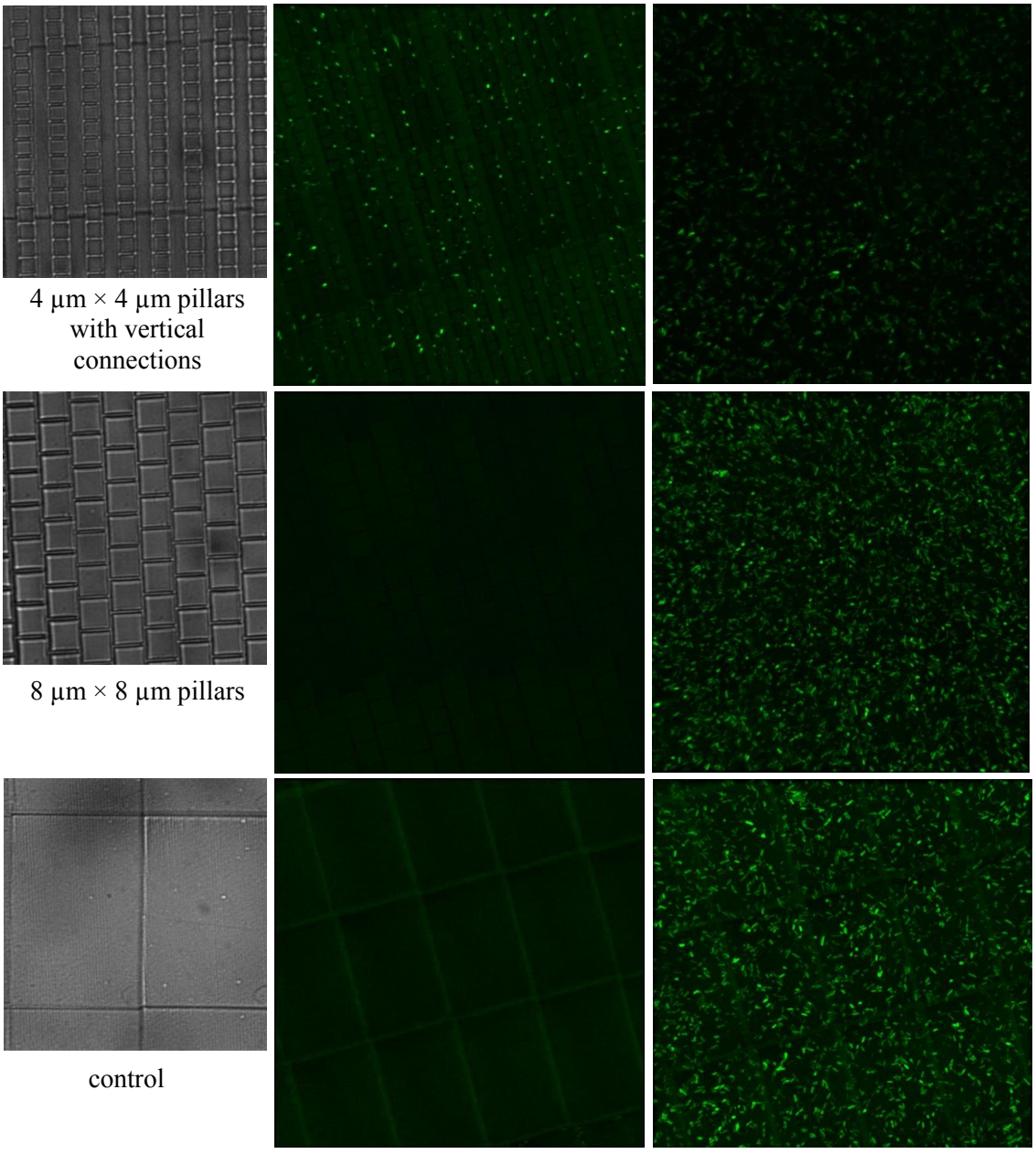


Figure 2.28: *(cont. from previous page)*. DIC images of topographical surfaces are shown respectively on the left. Confocal images show PA14 attachment between pillars (left) and atop pillars (right). Attachment atop pillars increased from the smallest pillars to the control surface, which was meant to represent an infinitely-large pillar. Scale bar = 10 μm (DIC images) and 20 μm (confocal images).

## 2.7 REFERENCES


[1] Š Petronis, K. Berntsson, J. Gold, and P. Gatenholm, "Design and Microstructuring of PDMS Surfaces for Improved Marine Biofouling Resistance," *Journal of Biomaterials Science, Polymer Edition* 11, no. 10 (2000): 1051-1072.

[2] C. Díaz, P. L. Schilardi, R. C. Salvarezza, and M. F. L. de Mele, "Nano/Microscale Order Affects the Early Stages of Biofilm Formation on Metal Surfaces," *Langmuir* 23 (2007): 11206-11210.

[3] J. M. Schumacher, C. J. Long, M. E. Callow, J. A. Finlay, J. A. Callow, and A. B. Brennan, "Engineered Nanoforce Gradients for Inhibition of Settlement (Attachment) of Swimming Algal Spores," *Langmuir* 24 (2008): 4931-4937.

[4] J. M. Willey, L. M. Sherwood, and C. J. Woolverton, *Microbiology*, 7th edition (New York: McGraw-Hill, 2008), 66-67.

[5] A. B. T. Semmler, C. B. Whitchurch, and J. S. Mattick, "A Re-Examination of Twitching Motility in *Pseudomonas aerugionsa*," *Microbiology* 145 (1999): 2863-2873.

[6] J. S. Mattick, "Type IV Pili and Twitching Motility," *Annual Reviews of Microbiology* 56 (2002): 289-314.

[7] D. Wall and D. Kaiser, "Type IV Pili and Cell Motility," *Molecular Microbiology* 32, no. 1 (1999): 1-10.

[8] A. J. Merz, M. So, and M. P. Sheetz, "Pilus Retraction Powers Bacterial Twitching Motility," *Nature* 407 (2000): 98-102.

[9] D. Kaiser, "Bacterial Motility: How Do Pili Pull?" *Current Biology* 10, no. 21 (2000): 777-780.

[10] G. A. O'Toole and R. Kolter, "Flagellar and Twitching Motility are Necessary for *Pseudomonas aeruginosa* Biofilm Development," *Molecular Microbiology* 30, no. 2 (1998): 295-304.

[11] R. M. Harshey, "Bacterial Motility on a Surface: Many Ways to a Common Goal," *Annual Reviews of Microbiology* 57 (2003): 249-273.

[12] D. Wall and D. Kaiser, "Alignment Enhances the Cell-to-Cell Transfer of Pilus Phenotype," *Proceedings of the National Academy of Sciences* 95 (1998): 3054-3058.

[13] M. Klausen, A. Heydorn, P. Ragas, L. Lambertsen, A. Aaes-Jørgensen, S. Molin, and T. Tolker-Nielsen, "Biofilm Formation by Pseudomonas aeruginosa Wild Type, Flagella and Type IV Pili Mutants," Molecular Microbiology 48, no. 6 (2003): 1511-1524.

[14] W. Barthlott and C. Neinhuis, "Purity of the Sacred Lotus, or Escape from Contamination in Biological Surfaces," *Planta* 202 (1997): 1-8.

[15] B. Bhushan and Y. C. Jung, "Micro- and Nanoscale Characterization of Hydrophobic and Hydrophilic Leaf Surfaces," *Nanotechnology* 17 (2006): 2758-2772.

[16] R. Blossey, "Self-Cleaning Surfaces – Virtual Realities," *Nature Materials* 2 (2003): 301-306.

[17] T. Sun, L. Feng, X. Gao, and L. Jiang, "Bioinspired Surfaces with Special Wettability," *Accounts of Chemical Research* 38 (2005): 644-652.

[18] K. K. Chung, J. F. Schumacher, E. M. Sampson, R. A. Burne, P. J. Antonelli, and A. B. Brennan, "Impact of Engineered Surface Microtopography on Biofilm Formation of Staphylococcus aureus," *Biointerphases* 2, no. 2 (2007): 89-94.

[19] N. C. Caiazza and G. A. O'Toole, "SadB is Required for the Transition from Reversible to Irreversible Attachment during Biofilm Formation by *Pseudomonas aeruginosa* PA14," *Journal of Bacteriology* 186, no. 14 (2004): 4476-4485.

[20] M. Klausen, A. Aeas-Jøregensen, S. Molin, and T. Tolker-Nielsen, "Involvement of Bacterial Migration in the Development of Complex Multicellular Structures in *Pseudomonas aeruginosa* Biofilms," *Molecular Microbiology* 50, no. 1 (2003): 61-68.

[21] M. M. Ramsey and M. Whiteley, "*Pseudomonas aeruginosa* Attachment and Biofilm Development in Dynamic Environments," *Molecular Microbiology* 53, no. 4 (2004): 1075-1087.

[22] B. Kaehr and J. B. Shear, "Mask-Directed Multiphoton Lithography," *Journal of the American Chemical Society* 129 (2007): 1904-1905.

[23] B. Kaehr and J. B. Shear, "Multiphoton Fabrication of Chemically Responsive Protein Hydrogels for Microactuation," *Proceedings of the National Academy of Sciences* 105, no. 26 (2008): 8850-8854.

[24] J. L. Connell, A. K. Wessel, M. R. Parsek, A. D. Ellington, M. Whiteley, and J. B. Shear, "Probing Prokaryotic Social Behaviors with Bacterial "Lobster Traps," mBio 1, no. 4 (2010): 202-210.

[25] S. Park, P. M. Wolanin, E. A. Yuzbashyan, P. Silberzan, J. B. Stock, and R. H. Austin, "Motion to Form a Quorum," *Science* 301 (2003): 188.

[26] B. Kaehr, *Defining Cellular Microenvironments using Multiphoton Lithography*, (The University of Texas at Austin, 2007): 130-140.

# Chapter 3: Towards the Design of Topographies for Preventing and Promoting Bacterial Attachment to Surfaces

## 3.1 INTRODUCTION

Topographical approaches for inhibiting cell-cell contacts, intercellular communication, and other events critical along the biofilm developmental pathway are likely powerful methods for creating an antifouling surface. These events, which might broadly be described as bacterial social behaviors, are often crucial to bacterial attachment to surfaces. Indeed, the most powerful approach is almost certainly one that disrupts biofilm formation at the level of bacterial attachment to a surface.

In Chapter 2, a variety of topographical surfaces were tested and shown to influence PA14 attachment orientations and to possibly induce differential levels of attachment and biofilm formation. In this chapter, ideas presented in Chapter 2 are extended into new directions, with topographical surfaces containing feature sizes on low to submicron scales. PA14 cells are shown to align within grooves of suitable dimensions and to attach with differential levels within holes of various sizes. One major focus of this chapter is on inhibiting attachment by subtracting surface areas of appropriate dimensions from positively-fabricated surfaces. During these experiments, it was found that while fabrication resolution of positively-fabricated features is limited to ~ 0.5 μm in the radial dimension, smaller resolutions can be obtained with negatively-fabricated features.

One special note needs to be made at this time. Observations within this chapter were based on detection of punctate fluorescence, and all statements in this chapter regarding PA14 attachment levels actually represent punctate fluorescence alone – not true attachment levels. In the body of this work, scattering effects caused by

topographical surfaces during confocal imaging are discussed. These effects limit confidence in what the true attachment levels are will require additional experiments.

## 3.2 GROOVED TOPOGRAPHIES

### 3.2.1 Experimental Methods

The static (no flow) assay used for this experiment was described with other relevant details in sections 1.3.4 and 2.6.1. Structures were fabricated with 0.3 μm step sizes to total heights of 3 μm, including a base layer of a solid protein surface with protein grooves fabricated atop the base of ~ 1 μm in height. Two topographical surfaces were tested with grooves – grooves with widths of 1 μm with walls between them of 1 μm and grooves with widths of 1.5 μm with walls between them of 1.5 μm. Several other surfaces were also tested in this experiment; the results of these are shown in Figures 2.23 and 3.3). The grooves were rectangular and might also be described as trenches. Structures were stitched together to produce topographical surfaces with dimensions of ~ 200 μm × 200 μm. Structures were pre-conditioned overnight with the inoculation media. To reduce autofluorescence of structures, structures were photobleached by reflecting the output of a mercury lamp off a 90/10 mirror into the back aperture of a 40×/0.75 NA objective (Zeiss) for 10 minutes. PA14 inoculation $OD_{600}$ was 0.01. Confocal imaging was acquired with nominal voxel dimensions of 0.23 μm (x-y) and vertical step sizes of 0.2 μm in two channels. The "green" channel used an excitation wavelength of 488 nm (Ar+ laser) with an emission bandwidth of 495 to 520 nm, while the "red" channel used an excitation wavelength of 543 nm (HeNe Laser) with an emission bandwidth of 570 to 620 nm. The green channel imaged gfp-expressing cells and structures, while the red channel imaged structures only.

### 3.2.2 Results

Grooved topographies were fabricated and tested with PA14 cells for several reasons. First, this set of structures was developed along with surfaces containing holes (Figure 3.3) for testing features on size scales similar to or smaller than the lengths and/or diameters of PA14 cells. Second, throughout many previous experiments, it was observed that cells attached heavily along the outside walls of structures. Since it appeared that walls promoted PA14 attachment, it was hypothesized that an aligned sequence of walls might also promote attachment behaviors. Finally, there are instances in the literature in which trenches have been tested with nonmotile spores [4] and motile bacterial cells [5].

The dimensions tested were 1-μm-wide grooves separated by 1-μm-thick walls and 1.5-μm-wide grooves separated by 1.5-μm-thick walls. Within grooves of both sizes, PA14 cells were frequently aligned with their long axes parallel to groove walls, especially for the 1-μm grooves (Figure 3.1). Furthermore, cells had more degrees of freedom in their orientations within 1.5-μm grooves relative to 1-μm grooves. The organization induced for surface-attached cells within the grooves was apparently lost above the grooves (Figure 3.2). Groove depths were ~ 1 μm, a dimension that would be interesting to modulate in the context of cell-cell communications. For example, deeper grooves might isolate cells further from those above the grooves, which in turn might reduce biofilm formation. Alternatively, grooves of appropriate dimensions might enhance biofilm formation by producing favorable cell-cell and cell-wall interactions.

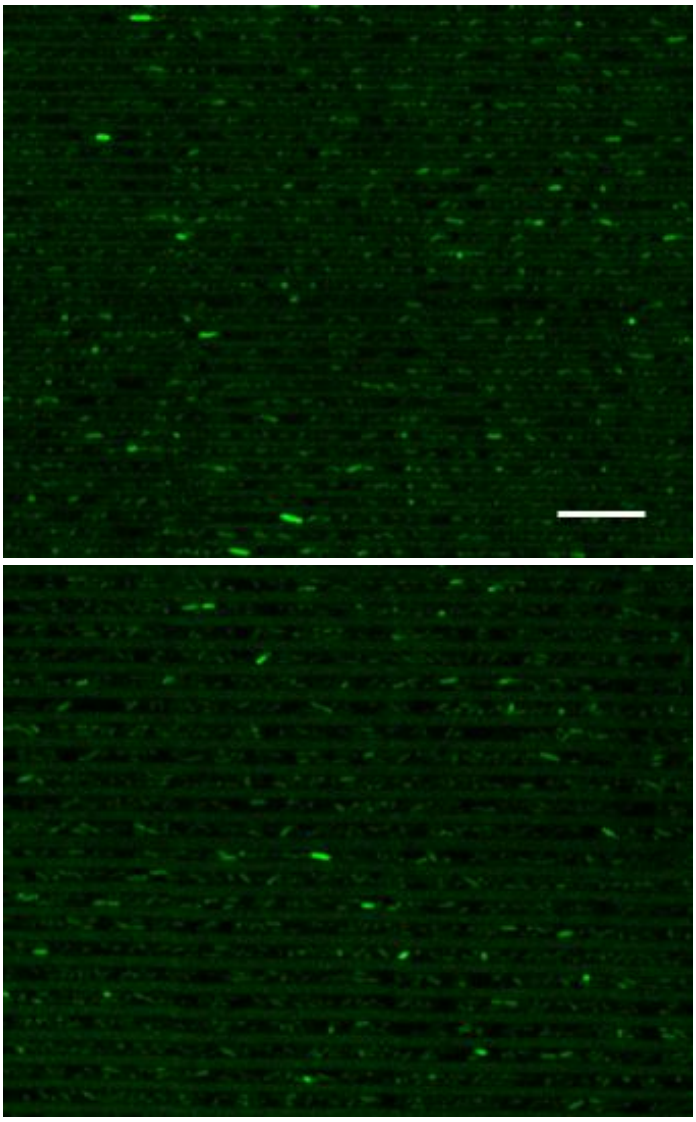

Figure 3.1: PA14 attachment within grooves. Grooves were 1-µm-wide and separated by 1-µm-thick walls (top) and 1.5-µm-wide and separated by 1.5-µm-thick walls (bottom). Images show confocal slices in the green channel under static (no flow) conditions 24 hrs post-inoculation. Cells were expressing gfp and can be seen between groove walls. There was a tendency for cells to align their long axes parallel with groove walls, particularly for the 1-µm grooves (top). Within 1.5-µm grooves, cells had more degrees of freedom in their orientations. Scale bar = 10 µm.

These surfaces may be particularly interesting to test under flow conditions for experiments involving spatial organization within biofilms. For example, *P. aeruginosa* cells are sometimes aligned with their long axes parallel within certain regions of biofilms [1]. In the formation of extracellular polymeric matrix, cell-cell interactions may be promoted by alignment of cell surfaces with helical expression patterns of polysaccharides [2]. In the formation of mushroom biofilms, aligned base layers of cells might affect the formation of the stalk (made of nonmotile cells) and subsequent formation of the cap (made of motile cells) [3]. It would also be interesting to test the effects of mechanical cell-wall and cell-cell interactions on irreversible attachment. (Irreversible attachment is physically-defined as attachment of PA14 cells along their long axes and has been associated with expression of a SadB protein [3]).

These particular groove/wall sizes facilitated heavy PA14 attachment both within and above grooves. The control surface tested with these structures (Figure 2.23a) also showed heavy PA14 attachment. By contrast, PA14 attachment levels were much lower on other topographical surfaces tested with these structures (e.g., pillars shown in Figure 2.23 (b) and (c) and on surfaces with 1-μm-wide and 1.5-μm-wide holes in Figure 3.3).

It would be informative to see if PA14 attachment could be reduced either within or above the grooves by modulating groove/wall dimensions. To decrease PA14 attachment above the grooves, for example, the depths of the grooves might be increased while decreasing the wall thicknesses. As the thicknesses of the walls decreased, the probability that a given cell could attach longitudinally to the top of the wall would also decrease. Indeed, even with the wall sizes in this experiment, cells had a relatively low probability for attaching with their long axes fully along the top surface of a wall. If the walls were spaced far enough apart, then cells would not be able to attach from one wall to the next wall. However, this would necessarily increase attachment of cells between

the walls. Ignoring attachment between the walls, a question to be asked is: can the width of the wall be decreased to the point that cell attachment is greatly reduced to its top surface. Then, if cells are unable to attach atop the wall, how can the walls be arranged or assembled to reduce bacterial attachment?

The resolution within the current fabrication configuration used in this work is limited to features of ~ 0.5 μm. Since this is a size that is as large as the dimensions in the short axis of PA14, much better ratios of fabrication resolution to bacterial size could be achieved by testing surfaces with a larger, rod-shaped motile cell, such as *Bacillus subtilis*.

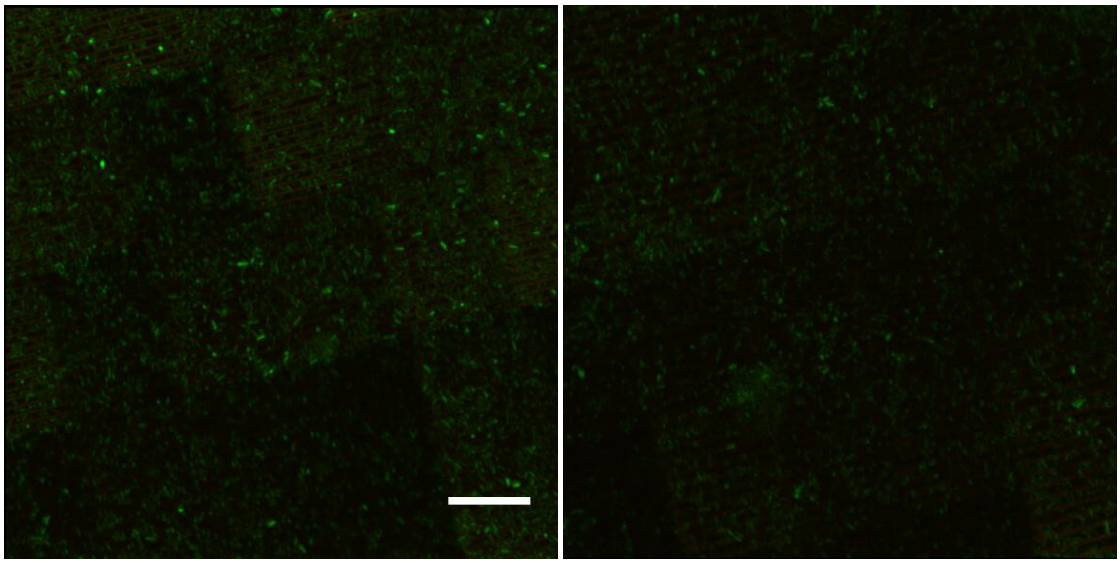

Figure 3.2: PA14 attachment above grooved surfaces. Maximum projection intensity confocal volume images show heavy attachment above the 1-μm (left) and 1.5-μm (right) groove surfaces. Cells are shown in green and structures in reddish brown due to autofluorescence of structures in the overlaid green and red channels. Organization induced by the grooves appeared to be lost above the surfaces. Scale bar = 20 μm.

## 3.3 Removal of Surface Area to Influence Bacterial Attachment

### 3.3.1 Experimental Methods

Further experimental details were given in sections 1.3.4 and 2.6.1. Briefly, fabrication solutions were filtered with a 0.2-μm filter next to a flame just prior to use and were made of 400 mg $mL^{-1}$ BSA diluted into a solution of 7.5 to 10 mM methylene blue in 20 mM HEPES (pH = 7.4). In this section, topographies were fabricated containing submicron holes within surfaces. It should be noted that all dimensions given in this section are estimates only. They have been estimated by a conversion factor between the length of a fabricated structure, such as a simple 10 μm by 10 μm box, and the number of pixels required in a mask to fabricate that structure. The conversion factor was found to be 12.5 pixels per 1-μm fabrication length for the x-y dimension given the resolution of the monitor (1280 × 1024). However, this conversion factor is based on positively-fabricated features, which swell upon rinsing out the fabrication solution with buffer. Therefore, negatively- fabricated features will actually have smaller dimensions than predicted by the conversion factor. For example, the 1-μm-diameter holes are likely smaller than that, especially because they were fabricated with 12 pixel-diameters, rather than 12.5-pixel diameters.

For the 24 hrs assays, structures were fabricated to heights of 5 μm with step sizes of 0.3 μm. Surfaces were pre-conditioned with cell media for at least 1 hr prior to inoculation and photobleached as described in section 3.2.1 (except for structures shown in Figure 3.9). Inoculation densities of PA14 cells were 0.01 $OD_{600}$. Post-inoculation, structures were incubated with cells at 28 to 30 °C and kept at this temperature until they were transferred to a confocal microscope in a separate building for imaging. Just prior to imaging, structures were rinsed by adding and removing 5 successive rinses of 400 μL

of fresh media. On the first rinse, a volume of 400 μL of media was pipetted up and down 3 times. Confocal image settings were described in section 3.2.1.

For the 1 hr static assays, structures were fabricated to heights of 2 μm with step sizes of 0.3 μm. Structures were not photobleached, but surfaces were placed at 37 °C overnight prior to inoculation. This was done to allow structures to attain equilibrium for any possible thermal-induced swelling, which is expected to be minimal for structures fabricated with methylene blue as the photosensitizer. They were also preconditioned with inoculation media for at least 1 hr prior to inoculation. Inoculation densities of PA14 cells were 0.1 $OD_{600}$. Structures were incubated with cells at 37 °C and kept at this temperature until they were transferred to a confocal microscope in a separate building for imaging. Just prior to imaging, structures were rinsed by adding and removing 4 successive rinses of 400 μL of fresh media. Pipette agitation was not used since this caused removal of a large fraction of cells at this time point. Confocal image settings were the same as described in section 3.2.1, except that the red channel was excited with a 594-nm HeNe laser line with emission collected at 620 to 670 nm.

For the assay with fluorescent beads, structures were treated in the same manner as for the 1 hr cell attachment assays, except that structures were not rinsed prior to imaging. Polystyrene fluorescent beads (Bangs Laboratories) were "Dragon Green" (excitation maximum 480 nm, emission maximum 520 nm) with diameters of 0.5 μm. Beads were 1% by weight in deionized water with 0.1% Tween. For experiments, beads were diluted 1:100 in 1/3 TSB with 1 mM glucose. Confocal image settings were those used for the green channel in section 5.2.1.

The flow cell setup was described in section 1.3.4. Structures were fabricated to heights of 3 μm with step sizes of 0.3 μm. Following fabrication, structures were rinsed with 4 volumes of 20 mL of 20 mM HEPES buffer (pH = 7.4) and stored at 4 °C.

Structures were inoculated with PA14 densities of 0.1 $OD_{600}$ and taken directly to a 37 °C walk-in room. Structures with cells were incubated for ~ 1 hr without flow. After 1 hr, flow was initiated at 50 µL per minute, and the flow cell setup was kept in the 37 °C walk-in except for imaging in the confocal microscopy room at time points of 24 and 48 hrs. Confocal image settings were those used for the 1 hr assay.

### 3.3.2 Surfaces with Holes of Various Sizes

In conjunction with the grooved topographies, one of the main goals of placing closely-spaced holes together was simply to test small features with dimensions of 0.5, 1, and 1.5 µm – scales that were relevant to the dimensions of rod-shaped PA14 cells. It was hypothesized that such features might either promote or inhibit PA14 attachment. This experiment was also derived from the microchamber array studies in which cells descended beneath a surface through small entrance apertures.

In one of the earliest experiments with small, closely-spaced cylindrical holes, diameters were ~ 1 µm and 1.5 µm with wall thicknesses between the holes of ~ 0.5 µm (Figure 3.3). The wall thicknesses were selected to be on a size-scale similar to PA14 diameters. In Figure 3.3 (a) and (c), PA14 cells appear as dots within holes, indicating orthogonal orientation relative to the coverglass, with overall low levels of attachment within the small apertures. On the surfaces above the holes (Figure 3.3 (b) and (d)), there were much lower levels of punctate fluorescence relative to the control surface tested on that day (Figure 2.23a). This seemed to be indicative of a surface that inhibited PA14 attachment – a result that was unexpected.

Since there were some PA14 cells attached within the holes (Figure 3.3 (a) and (c)), surfaces containing holes with smaller diameters were tested while maintaining wall thicknesses of ~ 0.5 µm (Figures 3.4 and 3.5). The results of these experiments appeared

in indicate heavier levels of PA14 attachment to surfaces with holes of ~ 300 nm relative to surfaces with holes of ~ 600 nm in diameter. Control surfaces also had heavy levels of attachment that were similar to surfaces with holes of ~ 300 nm.

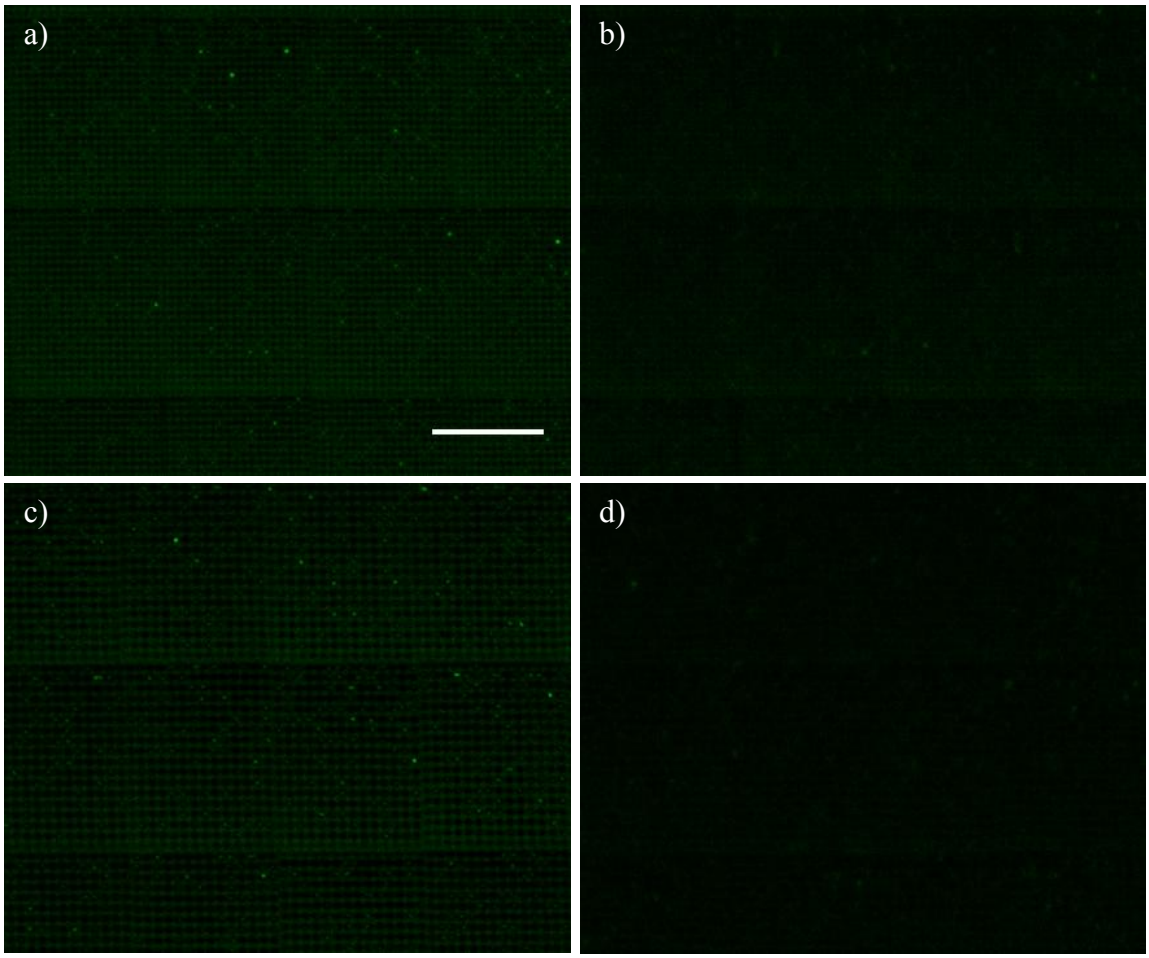


Figure 3.3: PA14 attachment to surfaces with cylindrical holes. Confocal image slices show attachment of cells to surfaces 24 hrs post-inoculation under static (no flow) conditions. Structures had small holes that extended all the way through the structure to the coverglass with heights greater than 3 μm. Holes were ~ 1-μm in diameter (a) and ~ 1.5-μm in diameter (c) with walls between holes of ~ 0.5 μm in thickness. Attachment appeared to be low both within the holes ((a) and c)), as well as on surfaces above the holes ((b) and (d)). Scale bar = 20 μm.

s

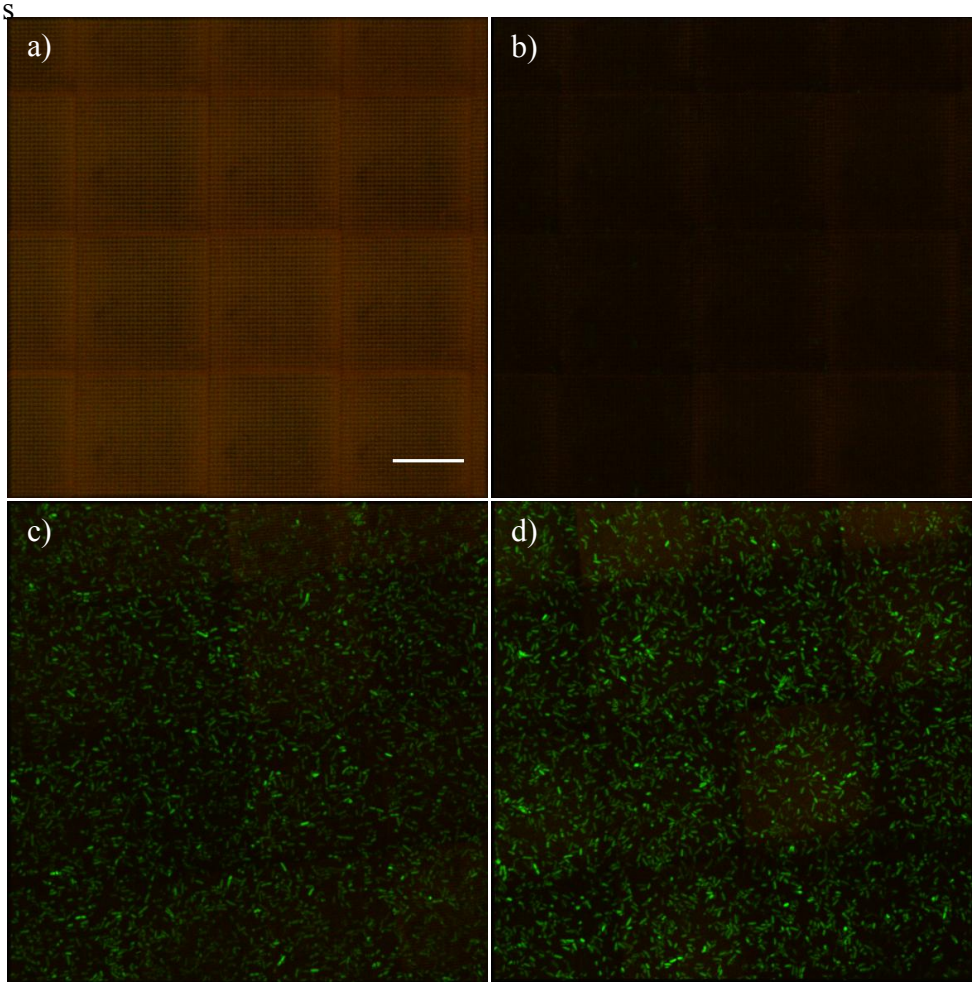


Figure 3.4: PA14 attachment to surfaces with holes that enable and inhibit attachment. Confocal maximum intensity projection images acquired 24 hrs post-inoculation under static (no flow) conditions show cells in green and structures in reddish brown due to overlaid green and red channels. PA14 cell attachment was extremely low within holes of diameters ~ 600 nm (a) and absent within holes of diameters ~ 300 nm (not shown). On the surfaces above holes, cell attachment appeared to be very low above the 600 nm holes (b) relative to above the 300 nm holes (c), which had a level of attachment similar to the control surface (d). Scale bar = 20 μm.

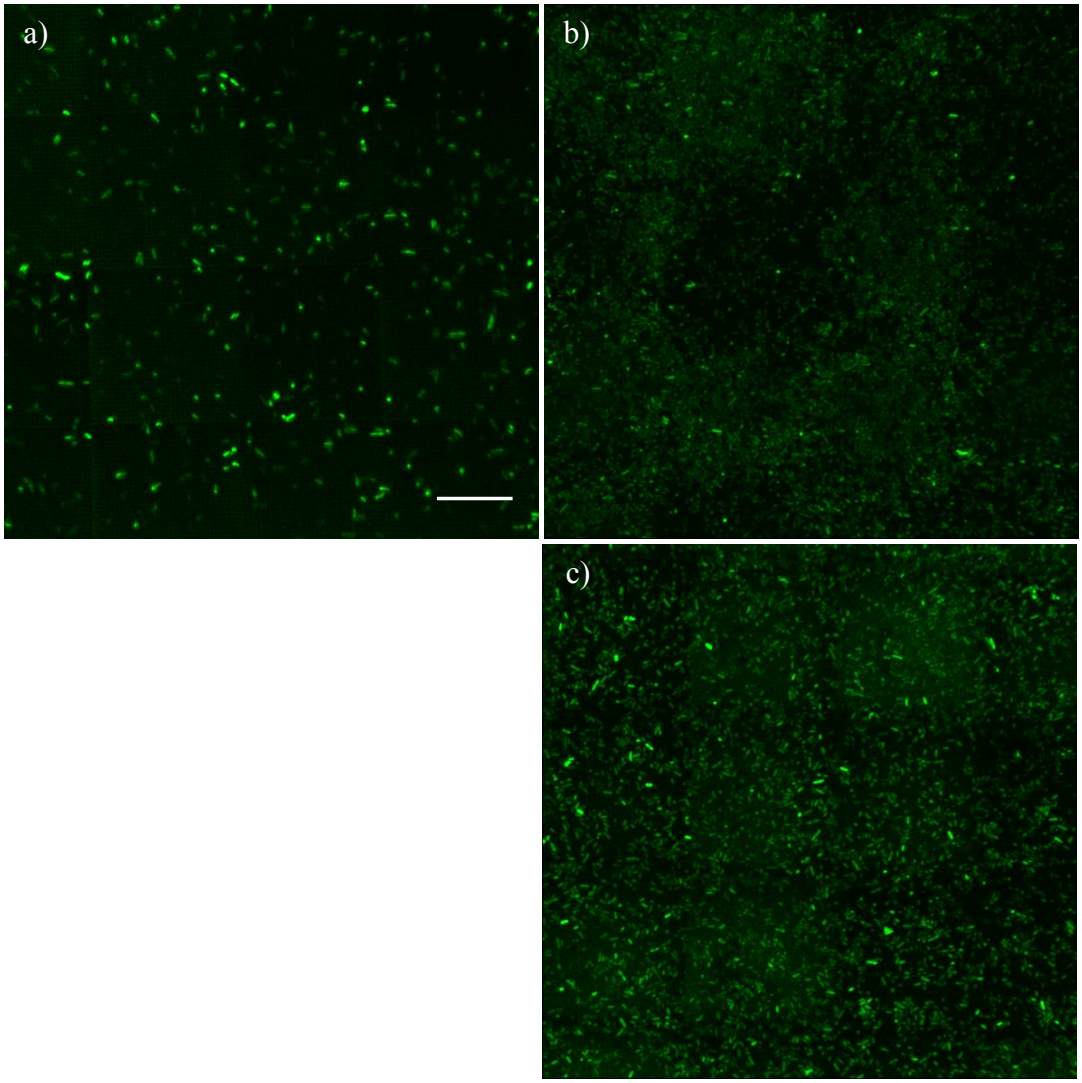


Figure 3.5: A replicate with particularly dense attachment on the surface containing 300-nm-diameter holes. PA14 attachment appeared to be the heaviest on the surface containing 300-nm-diameter holes (b), with attachment also heavy on the control surface (c). By contrast, the two surfaces showed relatively similar levels of attachment in Figure 3.4 (c) and (d). As with the replicate shown in Figure 3.4 and all other replicates, the surface containing 600-nm-diameter holes (a) showed a much lower level of attachment, although it was higher in this replicate than the one shown in Figure 3.4. Confocal maximum intensity projection, with contrast adjusted to the same levels for all images, show the green channel only. Scale bar = 20 μm.

In Figure 3.5, PA14 attachment levels were similar for the control surface (d) and the surface containing 300-nm-diameter holes (c), while the surface with 600-nm-diameter holes showed very low levels of attachment both within (a) and above (b) the surface. By contrast, the replicate in Figure 3.4 showed levels of PA14 attachment that were heavier, with denser clusters of cells, on the surface with 300-nm-diameter holes (b) relative to the control surface (c). The surface with 600-nm-diameter holes in Figure 3.4a had a much lower level of PA14 attachment relative to the control surface and surface containing 300-nm-diameter holes, as with the replicate shown in Figure 3.4. There may be multiple reasons for this effect. First, surfaces containing larger holes (e.g., diameters of 600 nm and 1 μm) have less surface area. Second, the larger holes may inhibit cell attachment, particularly "irreversible" attachment, over the lengths of the holes.

The topographical surface with 600-nm-diameter holes could be placed contiguously with control surfaces to produce boundaries between enhanced and decreased punctate fluorescence, in which punctate fluorescence seemed to be indicative of increased PA14 attachment levels (Figure 3.6). One of the goals of these experiments was to progressively decrease the dimensional areas of the alternating surfaces until the control surface itself had reduced levels of PA14 attachment. In many respects, this idea was the reverse of the pillar gradient experiments (section 2.6.3). An experiment in which control surfaces and surfaces with holes were alternated with progressively smaller widths appeared to show decreasing attachment levels of PA14 cells on control surfaces as the widths were decreased (data not shown).

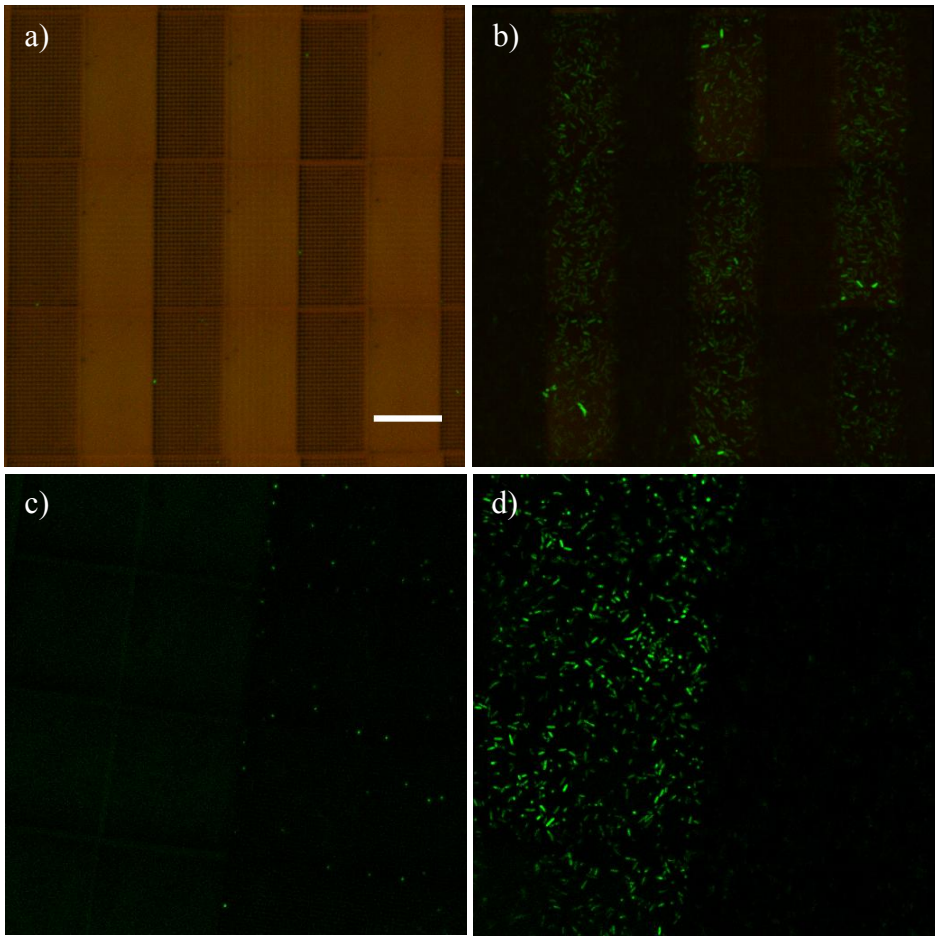


Figure 3.6: Surfaces with alternating control topographies and topographies containing holes with diameters of ~ 600 nm. Confocal maximum intensity projection images show PA14 attachment within (a) and above (b) alternating control surfaces and surfaces with holes. Cells appeared to attach in higher numbers to the control surfaces. While cell attachment within the holes was very low in image (a), it was higher within the holes in image (c) (right-side of the image). Image (c) shows a confocal image slice of PA14 attachment within a surface that was partly control (left side) and partly a surface with holes (right side). In image (d), the confocal slice shows heavier PA14 attachment on the control surface (left side) relative to the surface with holes (right side). Scale bar = 20 μm.

The submicron feature dimensions within topographies containing holes were difficult to resolve with light microscopy, particularly for diameters of holes ~ 300 nm.

However, dehydration and fixation of structures showed that holes were indeed resolved for the 300-nm-diameter (Figure 3.7 (b) and (d)). SEM images showed irregular holes for all diameters fabricated. These diameters included sizes of roughly 0.3 to 1 μm, with estimated dimensions being most likely larger than the actual dimensions, as discussed in the experimental methods section. SEM dehydration caused BSA structures to shrink, which made the holes appear larger and walls thinner than hydrated structures. Atomic force microscopy images (Figure 3.8) show structures under hydrated conditions with apparent dimensions conforming more closely to those expected under hydrated conditions. As detected by punctate fluorescence within structures, bacteria showed increasing attachment levels within structures of progressively larger sizes.

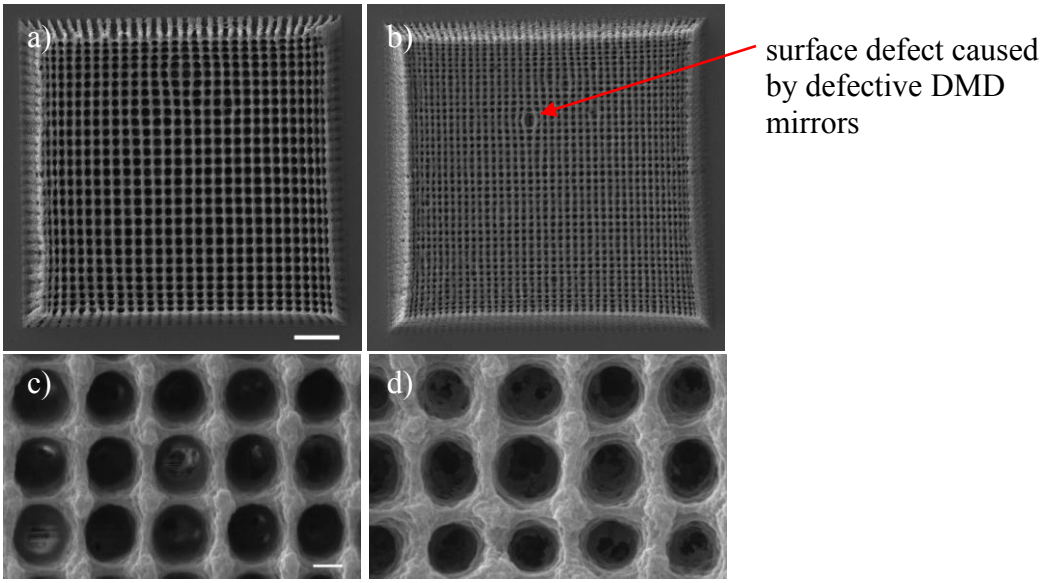


Figure 3.7: SEM images of surfaces with cylindrical holes. The images on the left show surfaces containing holes of diameters (prior to dehydration) of ~ 600 nm, while the images on the right show surfaces containing holes of diameters (prior to dehydration) of ~ 300 nm. BSA structures shrink considerably during the dehydration step, so the diameters of the holes were made larger and the walls thinner due to this process. Scale bar = 5 μm (a) and (b) and 500 nm (c) and (d).

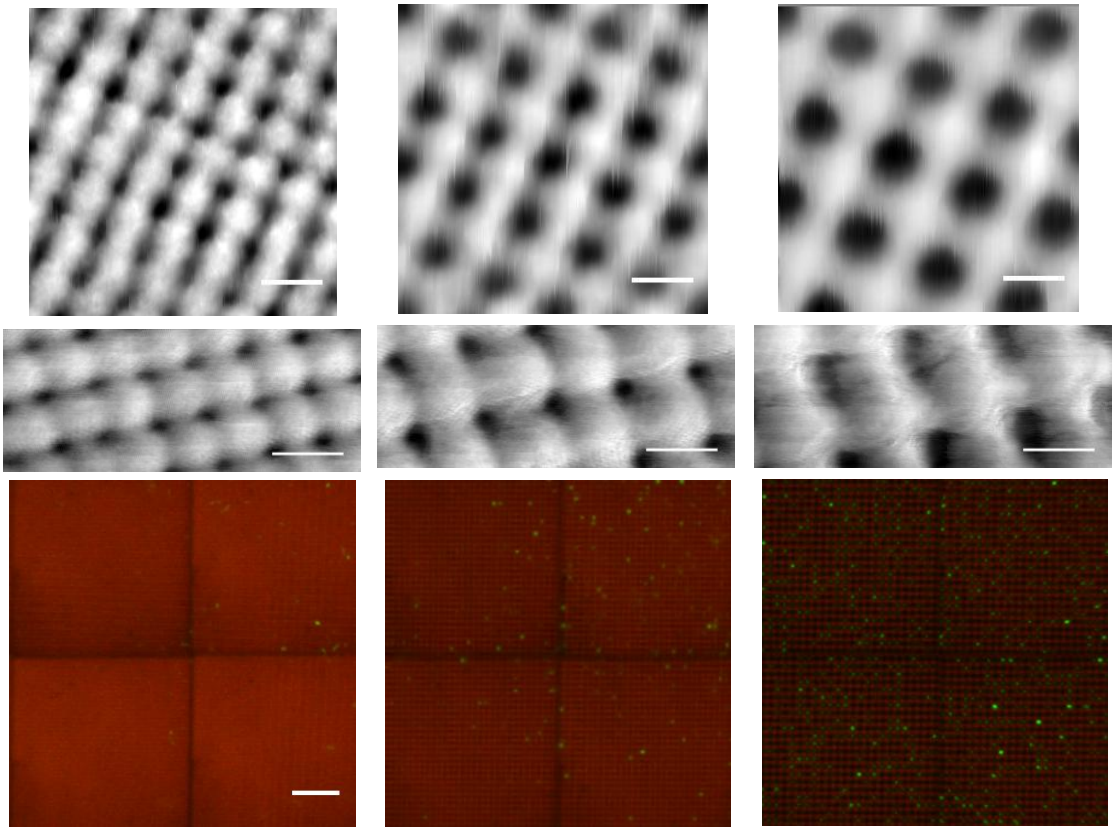

Figure 3.8: Atomic force microscopy images of hydrated surfaces containing holes of various sizes. Images are shown for theoretical sizes of holes of ~ 300 nm, ~ 600 nm, and ~ 1 μm with most images conforming roughly to these sizes. Figure adapted from the work of Eric Spivey. Scale bars = 1 μm.

Atomic force microscopy images (Figure 3.8) show structures under hydrated conditions with apparent dimensions conforming more closely to those expected under hydrated conditions. As indicated by punctate fluorescence levels within structures, attachment seemed to increase with the sizes of holes, with bacteria being largely excluded from holes with dimensions of 300 nm in diameter. In fact, cells shown in this image may have been above the surface since this is a confocal maximum intensity projection image and some planes may have been included above surfaces. The structure

with sizes of holes that are ~ 1 μm in diameter show cells oriented and arrayed within the holes orthogonal to the coverglass.

One original goal was to test PA14 attachment on surfaces with submicron holes of incremental diameters. However, due to time constraints, initial studies in this area were redirected towards testing attachment on surfaces with only a few sizes of holes. In several experiments, surfaces with 600 nm holes had much lower levels of attachment than surfaces with 300 nm holes, which generally had similar levels of attachment to control surfaces (e.g., Figures 3.4 and 3.5). However, in one experiment, both 300-nm-diameter and 600-nm-diameter had much lower levels of PA14 attachment relative to the control surface (Figure 3.9). In this particular experiment, PA14 attachment levels were unusually heavy, with dense clusters of cells covering a very high percentage of the control surface (Figure 3.9d). By contrast, much lower levels of attachment were observed on surfaces with holes, with cells covering a much smaller fraction of surface area relative to the control surface (Figure 3.9 (a), (b), and (c)). Cells also attached heavily within 1-μm-diameter holes (shown in Figure 3.8), but the level of attachment to the top of this surface appeared to be lower than the other surfaces as indicated by punctate levels of fluorescence (Figure 3.9c). PA14 cells attached within a much smaller fraction of 600-nm-diameter holes (Figure 3.8) relative to the 1-μm-diameter holes. While the trend between the surfaces with 300 nm and 600 nm holes was reversed in this experiment, the general trend of lower attachment levels on surfaces with relatively larger diameters of holes (~ 600 nm and ~ 1 μm) was maintained. Replicates with quantitative analysis are needed to further identify trends and attachment levels for 24 hrs static assays.

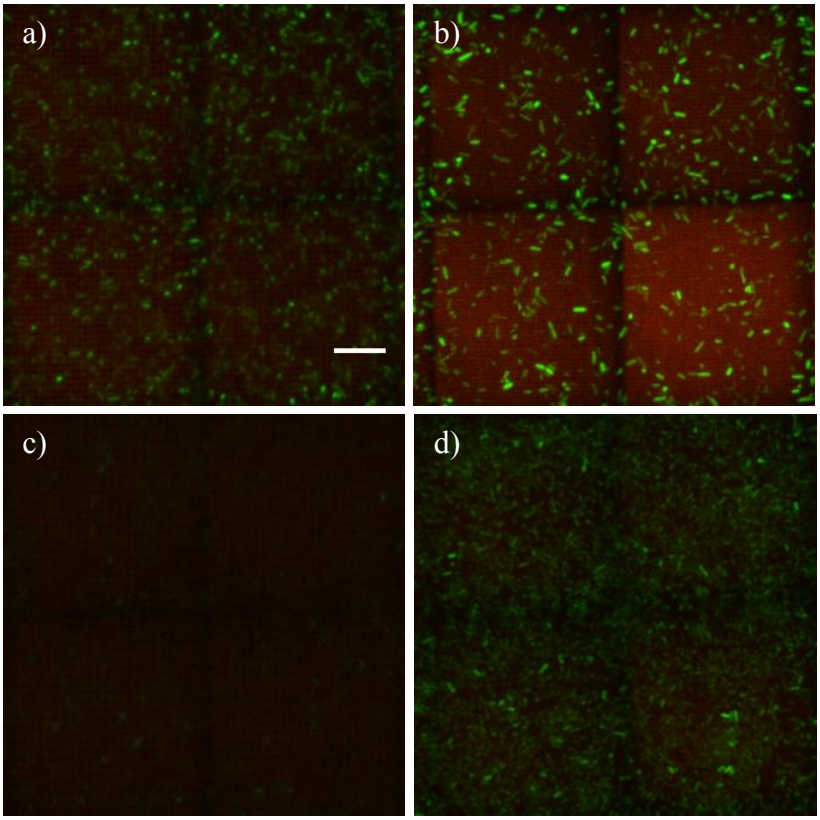


Figure 3.9: Surfaces with several sizes of holes on a day with particularly heavy PA14 attachment. PA14 attachment was especially heavy on surfaces for this particular experiment shown as maximum intensity projection confocal images 24 hrs post-inoculation under static (no flow) conditions. For example, the control surface (d) showed dense clusters of cells with relatively little of the reddish brown structure surface showing between the green cells. By contrast, PA14 attachment was much lower on surfaces with holes ((a), (b), and (c)). Contrary to several other experiments, this was the only one in which PA14 attachment was higher on a surface with 600 nm holes (a) relative to a surface with 300 nm holes (b). In (c), PA14 attachment atop surfaces with holes of ~ 1-μm diameter appears to be much lower than the other surfaces. Scale bar = 10 μm.

One of the greatest challenges for quantifying PA14 attachment to topographical surfaces containing submicron holes is the scattering of light by the surfaces. Confocal microscopy can be particularly challenging when examining samples that scatter light since it relies on precise re-focusing of light, originating from a specific focal region, at a

spatial filter. The topographical surfaces in these studies caused light scattering that reduced the signal-to-noise of cells. For surfaces containing holes of diameters 0.3, 0.6, and 1 μm, scattering increased as the diameters of the holes increased, a result obtained by measuring the fluorescence intensity of 0.5-μm polystyrene fluorescent beads imaged on the surfaces (Figure 3.10). Scattering was likely particularly problematic since the diameters of the holes were similar to the emission wavelengths. Consequently, there were most likely some bacteria that were not detected in these experiments. Future experiments should focus on challenges related to detecting the bacteria. Two-photon scanning microscopy is likely a better method for detection on surfaces that scatter. Widefield fluorescence microscopy is another option, but autofluorescence of structures is problematic, as well as out-of-plane fluorescence and decreased light collection away from the coverglass.

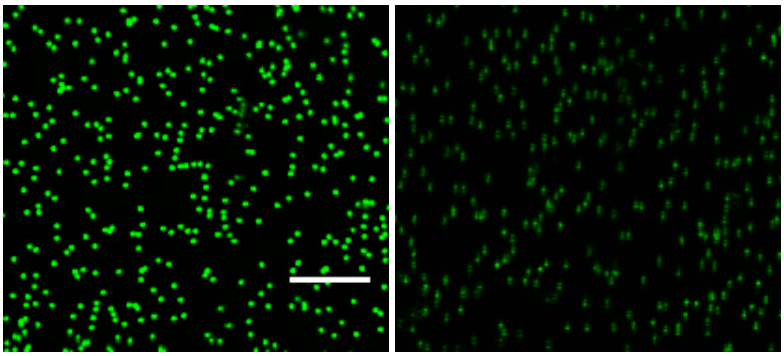

Figure 3.10: Fluorescent beads on surfaces with holes. The image on the left shows beads on a control surface, while the image on the right shows beads on a surface with 1-μm-diameter holes. The reduction in signal-to-noise of the beads on the surface with 1-μm holes was caused by scattering. Beads were also imaged on surfaces with 300 nm and 600 nm diameters of holes. Signal intensities of beads decreased as the diameters of the holes increased. Structure heights were ~ 6 μm. Scale bar = 10 μm.

The 24 hrs static assays showed variations between structures in punctate fluorescence that may be indicative of differential attachment levels between structures. Therefore, a 1 hr static attachment assay was developed to test PA14 attachment levels after short time scales. The assay was conducted at 37 °C, rather than 28 to 30 °C as used in the 24 hrs assays. Inoculation $OD_{600}$ was also increased to 0.1 (from 0.01 for 24 hrs assays) to obtain higher levels of attachment over the shorter time scale. Another difference was that structures were fabricated to only 2 μm in height to reduce scattering effects, since signals were higher on shorter structures. After 1 hr, PA14 attachment levels appeared to be similar for four structure types – a control surface and surfaces containing 300-nm-diameter, 600-nm-diameter, and 1-μm-diameter holes (Figure 3.11).

Although the temperature was higher in these experiments, one experiment was conducted at ambient temperature by observing PA14 attachment over the course of 1 hr with confocal microscopy. During this time period, PA14 attachment levels appeared to be similar on a control surface and a surface containing 600-nm-diameter holes. It is also not known what effects, if any, structure height had on these experiments. A further observation was made that it was relatively easy to rinse cells from the surfaces of these structures at this time point relative to rinsing of cells after 24 hrs. At this point, a tentative conclusion might be made that structures showed differential levels of attachment 24 hrs post-inoculation under the conditions specified in the experimental methods, but no differences were observed 1 hr post-inoculation. However, scattering effects must still be assessed at both time points and methods developed for detecting cells on surfaces that cause light scattering, such as the use of two-photon fluorescence microscopy.

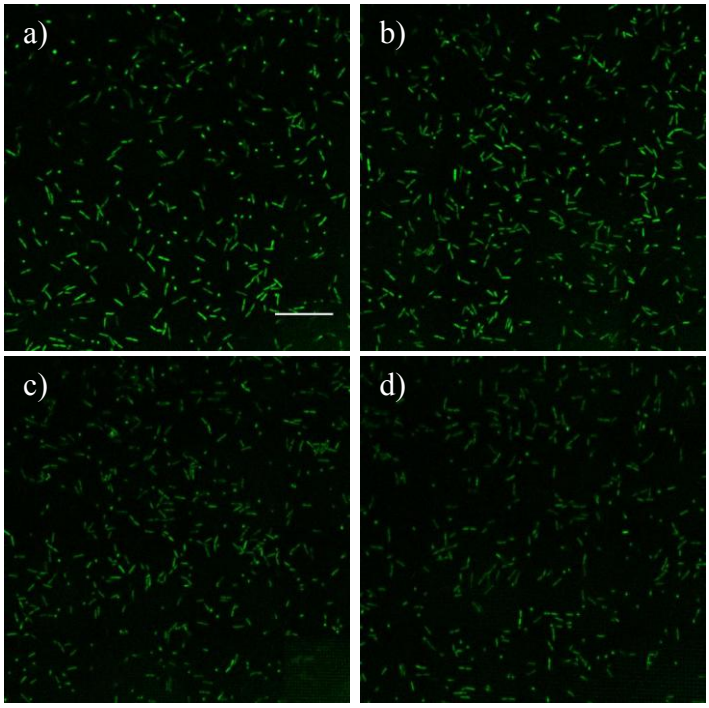


Figure 3.11: 1-hr PA14 attachment assay on topographies containing holes. These are confocal slices showing attachment on a control surface (a), a surface with 300-nm-diameter holes (b), a surface with 600-nm-diameter holes (c), and a surface containing 1-μm-diameter holes (d). Structures were fabricated to 2 μm in height, and structures and cells were incubated for 1 hr at 37 °C. Scale bar = 20 μm.

Structures containing holes were also tested under flow and imaged 24 hrs post-inoculation (Figure 3.12). There did not appear to be any significant differences in PA14 attachment levels on structures for this experiment, which was the only replicate conducted. Structures were only ~ 3-μm-tall, which is a height that is not much taller than the length of PA14 cells. It is possible that taller structures with generally larger sizes of holes (e.g., 1-μm-diameter) would reduce attachment by isolating cells between surface features, thereby inhibiting bacterial communication behaviors associated with biofilm formation. As the sizes of holes increased, it would also be more difficult for cells to attach across the holes, but this would increase attachment within the holes.

Attachment might also be reduced by modulating wall dimensions along with the diameters of cylindrical holes, or holes with other geometries (e.g., see Figure 3.13). Unfortunately, the resolution of DMD multiphoton lithography as configured within these experiments was limited to positive fabrication features of ~ 0.5 μm, although higher resolutions were obtained for negatively-fabricated features.

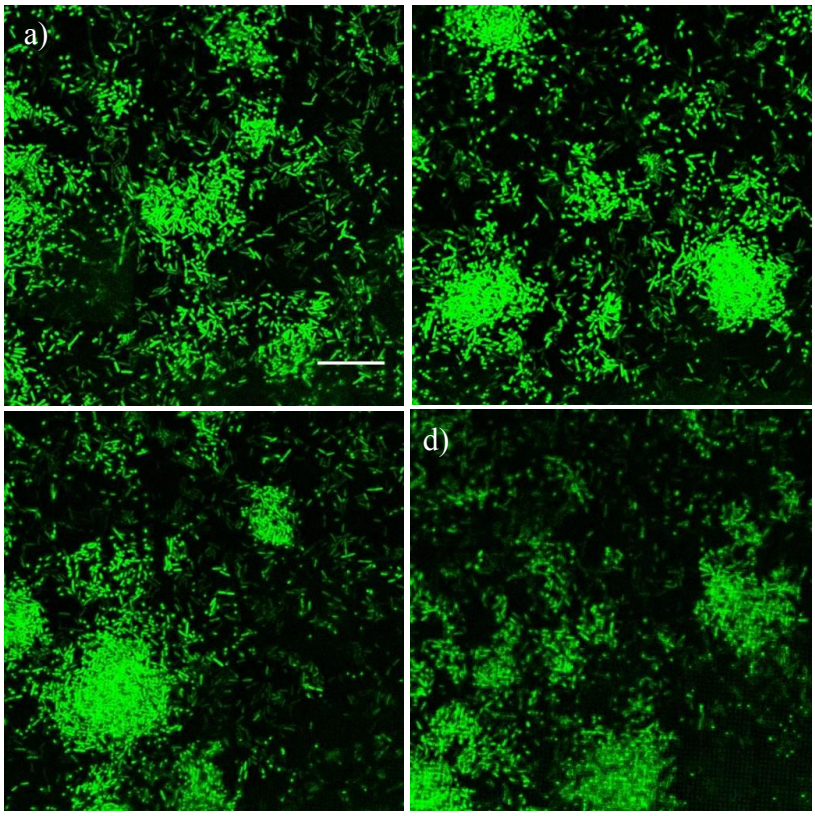


Figure 3.12: PA14 attachment under flow to topographies containing holes. Confocal image slices show attachment 24 hrs post-inoculation to a control surface (a), a surface containing 300-nm-diameter holes (b), a surface containing 600-nm-diameter holes (c), and a surface containing 1-μm-diameter holes (d). Structures were fabricated to heights of 3 μm and incubated under flow with cells at 37 °C. Scale bar = 20 μm.

Several alternative topographical surfaces created by removing surface area were prototyped and tested with cells. For example, structures with patterns such as the one

shown in Figure 3.13 were designed with rectangular holes intended to inhibit attachment across the length of the holes while preventing attachment within the holes.

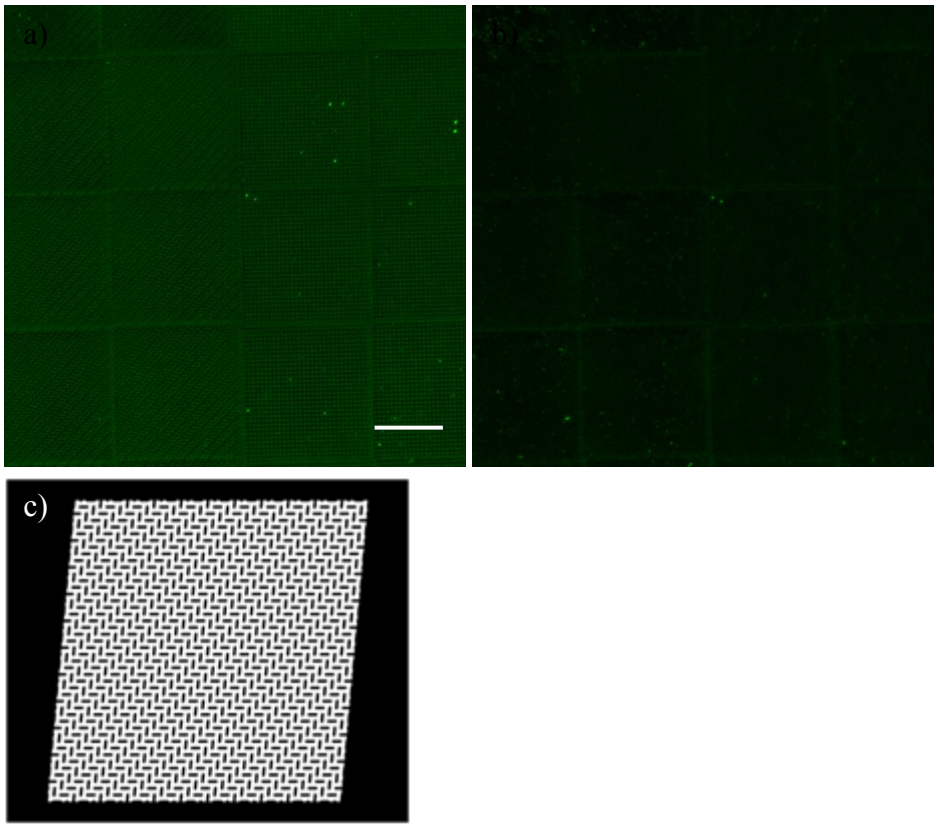


Figure 3.13: An alternative design for surface removal to reduce PA14 attachment. The structure shown in (a) was fabricated with half of the surface using the mask in (c) and half of the surface with 600-nm-diameter holes. Attachment levels appeared to be similar for the two surfaces both within the surface (a) and atop the surface (b) for a 24 hr attachment assay. The alternative surface was designed with rectangular holes with dimensions of ~ 0.3 μm × 1 μm with walls between holes of ~ 0.5 μm in thickness. The rectangular holes were meant to deter cells from attaching across the 1-μm chasms while preventing attachment within the holes due to the narrower widths. Scale bar = 20 μm.

### 3.3.3 Experiments Concerning PA14 Doublets

One interesting observation made during the 1 hr attachment assays was that the vast majority of PA14 cells attached as "doublets" – cells that appeared to have completed cell division but were not detached. By contrast, cells observed under static conditions at later time points, beyond a couple of hours post-inoculation, were observed to exist with the vast majority of cells as "singlets." At 1 hr time points, PA14 cells attached with the majority of cells as doublets across 2-μm-tall surfaces containing holes of sizes 400 nm, 600 nm, and 1 μm in diameter. By changing the sizes and geometrical arrangement of holes within surfaces, PA14 cells were largely prevented from attaching with their long axes parallel to the surface, even though the diameters of the holes were smaller than doublet lengths (Figure 3.14). Within the holes, PA14 cells attached with orientations that were almost exclusively orthogonal to the coverglass.

Topographical surfaces tested contained holes with diameters of ~ 1.4 μm, 1.6 μm, and 2 μm, which were larger than those tested for the 1 hr assay in Figure 3.11. Again, diameters were likely smaller than these estimates. The holes were geometrically arranged to have offset centers to reduce wall thicknesses, which were ~ 0.5 μm. These were intended to be thinner than those fabricated within surfaces in section 5.3.2 by changing the geometrical arrangement of holes and also reducing the number of white pixels between holes within the masks.

Although this experiment needs to be repeated, the results suggest that PA14 cells attach across holes as singlets, rather than doublets. This phenomenon could be useful for further topographical designs that influence PA14 attachment. It would also be interesting to test other *P. aeruginosa* strains, such as PA01, to see if these strains show similar behaviors. Since these structures were only 2-μm-tall, it may be that different results would be obtained with taller structures.

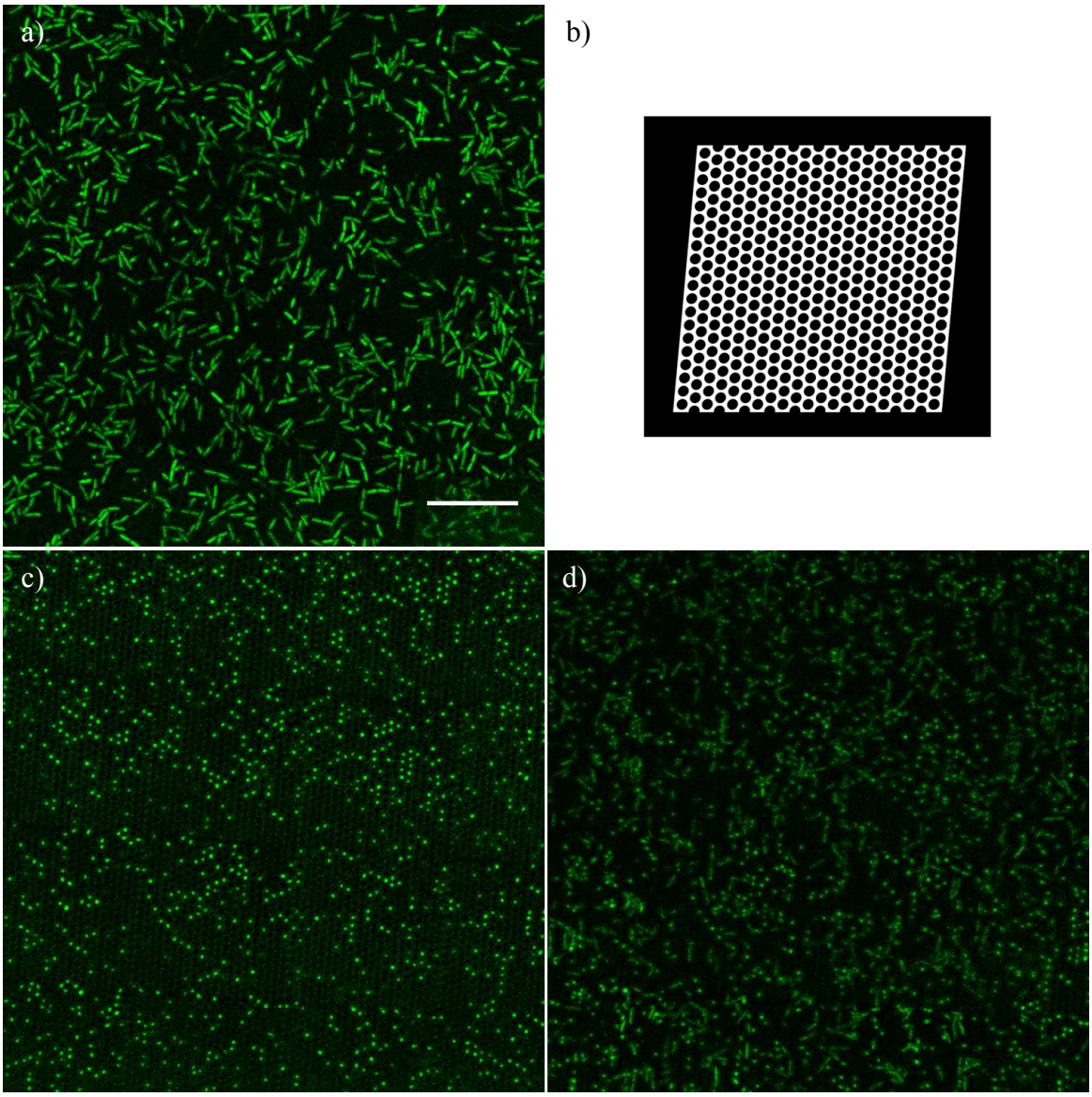


Figure 3.14: Attachment behavior of PA14 doublets. a) PA14 cells attached with the vast majority as doublets on a control surface. b) Mask used to fabricate the structure shown in (c) and (d). c) PA14 cells were confined to orthogonal attachment within holes of diameters ~ 1.4 μm. d) In contrast to the control surface, PA14 cells showed relatively low numbers of cells attached with their long axes parallel to the surface. This may be due to most singlet cells (~ 1.5 μm in length) being too short to attach across the holes. However, doublet cells are long enough (typically ~ 3 μm) to attach across the holes, but it appears that the vast majority did not attach across holes. Scale bar = 20 μm.

## 3.4 Conclusions and Future Directions

Exploration of topographical effects on bacteria and other microbes is still in the early stages of development in this work and throughout the scientific literature. This thesis work focused on microscale topographical influences on *P. aeruginosa*, but many of the ideas considered might be explored with other types of bacteria and microbes. For example, hierarchical surface topographies might be designed to influence attachment of microbes of various sizes. Regarding the specific work in this thesis, some directions seem to be promising but require more replicates and quantification of bacteria. It may also be that some of the ideas in this thesis will not work with the exact dimensions and/or geometries specified here, but the general concept might work by varying dimensions and/or geometries. One important point raised within this work is the critical need to consider the effects of scattering for topographical surfaces designed to influence bacterial attachment. These effects are likely problematic for a variety of microscale topographies.

While microscale topographies seem promising for influencing bacterial communication behaviors that are in turn important for bacterial attachment and biofilm formation, another concerted effort to study the effects of much smaller size scales seems like a prudent and critical approach to take. It is also an approach that may enable more fundamental questions about bacterial attachment to be answered. One of the most fascinating questions that can be asked for studies concerning topographical influences on bacterial attachment to surfaces is: what is required of a surface to make it amenable to attachment of a single bacterial cell or microbe?

To give a concrete example of how such a question might begin to be answered, a line of thought will be followed with *P. aeruginosa* PA14, just to make the following argument easier to read. However, it is of course obvious that the question posed above

is of interest for all bacterial cells and other microbes. As mentioned several times, PA14 cells are rod-shaped and have dimensions of ~ 0.5 to 0.8 μm × 1 to 2, with 2 μm in length being a high estimate. To conduct these experiments, careful measurements of cells would be requisite experiments.

Then, initial features to test might include rectangular pillars and posts, although on much smaller size scales than those explored in this thesis work, and much lower resolutions than can be achieved with the present fabrication configuration. Experiments would involve features that are placed far enough apart that cells would be unable to attach across the features. In fact, the features could be quite far apart from each other, since the idea would be to study PA14 attachment on isolated features. The heights of these features would also have to be tall enough that cells were unable to attach from the surface over the top of the features. In fact, a feature such as a rectangular pillar, parallel or otherwise to a surface, might even be suspended above the surface.

Through modulation of feature sizes and geometries, observations would be made as to how, if, and at what levels PA14 cells attached to these features. An example of a topographical feature might be a circular post that would not allow PA14 cells to attach atop the post. The intriguing question with these experiments would be: is there a feature that can be made that would prevent cells from attaching to all parts of the feature? If so, on what size scale is this feature – e.g., 100 nm (being a dimension several times smaller than the diameter of the short axis of the cell), 40 nm or lower (relating to the sizes of surface organelles)? It might only be necessary to find features that would prevent attachment of cells along one dimension. Then, identical surfaces associated with that dimension might possibly be configured in an arrangement that would prevent PA14 attachment nearly entirely. A caveat must be made here – there may likely be a small number of cells that would be resistant to such topographical influences,

as with chemical influences. The challenge of assembling the features into an arrangement that would almost exclusively prevent PA14 attachment would likely be a formidable one. For this task, automated high-throughput systems for assessing large numbers of topographical configurations would be most beneficial. This would be especially critical for conducting these experiments over a range of microbes. Critical microbes to test would include *S. aureus*, *E. coli*, *P. aeruginosa*, and other bacteria, fungi, and microbes associated with implant device failure.

If it is possible for PA14 cells to be prevented from attaching to features of specific sizes and geometries, then further experiments could probe the mechanisms for this result. Potential mechanisms would likely involve cell surface organelles associated with attachment and motility. It may be that topographical features on the size scales of pili and flagella might be strong candidates for preventing PA14 attachment. Or, another possibility may be that cells require some critical surface area to attach to that is related to the density of their surface receptors.

Uncovering the mechanisms involved in topographical influences for various bacteria and other microbes would likely uncover fascinating differences between microbial species and strains. Considering the variability in microbial cells, such as surface organelles, cell dimensions, and motility, it seems most improbable that one uniform set of principles governing topography would apply to all microbes. After all, these organisms have persisted for billions of years and adapted to a myriad of environments. Consequently, applications of topographical surfaces on implant devices, as with chemical methods, may require specialization depending on the types of microbes likely to infect that particular device in a specific location within the body. Beyond implant devices, surfaces that prevent bacterial attachment may have nearly limitless applications. However, similar to chemical methods for preventing bacterial attachment

to surfaces, overuse of these methods may likely cause resistant strains to develop. This is a rather fascinating and also disturbing idea to consider, and it is difficult to predict if such a result will actually come to pass and if so, it cannot be known how far into the future this would be.

## 3.5 REFERENCES


[1] R. C. Hunter and T. J. Beveridge, "High-Resolution Visualization of *Pseudomonas aeruginosa* PAO1 Biofilms by Freeze-Substitution Transmission Electron Microscopy," *Journal of Bacteriology* 187, no. 22 (2005): 7619-7630.

[2] L. Ma, M. Conover, H. Lu, M. R. Parsek, K. Bayles, and D. J. Wozniak, "Assembly and Development of the *Pseudomonas aerugionsa* Biofilm Matrix," PLoS Pathogens 5, issue 3 (2009): 1-11.

[3] M. R. Parsek and T. Tolker-Nielsen, "Pattern Formation in *Pseudomonas aeruginosa* Biofilms," Current Opinion in Microbiology 11 (2008): 560-566.

[4] N. C. Caiazza and G. A. O'Toole, "SadB is Required for the Transition from Reversible to Irreversible Attachment during Biofilm Formation by *Pseudomonas aeruginosa* PA14," *Journal of Bacteriology* 186, no. 14 (2004): 4476-4485.

[5] M. Callow, A. Jennings, A. B. Brennan, C. Seegert, A. Gibson, L. Wilson, A. Feinberg, R. Baney, and J. Callow," *Biofouling* 18 (2002): 229-236.

[6] C. Díaz, P. L. Schilardi, R. C. Salvarezza, and M. F. L. de Mele, "Nano/Microscale Order Affects the Early Stages of Biofilm Formation on Metal Surfaces," *Langmuir* 23 (2007): 11206-11210.

# Bibliography


R. Allen, R. Nielson, D. D. Wise, and J. B. Shear, "Catalytic Three-Dimensional Protein Architectures," *Analytical Chemistry* 77 (2005): 5089-5095.

W. Barthlott and C. Neinhuis, "Purity of the Sacred Lotus, or Escape from Contamination in Biological Surfaces," *Planta* 202 (1997): 1-8.

B. Bhushan and Y. C. Jung, "Micro- and Nanoscale Characterization of Hydrophobic and Hydrophilic Leaf Surfaces," *Nanotechnology* 17 (2006): 2758-2772

R. Blossey, "Self-Cleaning Surfaces – Virtual Realities," *Nature Materials* 2 (2003): 301-306.

N. C. Caiazza and G. A. O'Toole, "SadB is Required for the Transition for Reversible to Irreversible Attachment during Biofilm Formation by Pseudomonas aeruginosa PA14," *Journal of Bacteriology* 186, no. 14 (2004): 4476-4485.

P. R. Callis, "The Theory of Two-Photon-Induced Fluorescence Anisotropy," in *Topics in Fluorescence Spectrscopy: Nonlinear and Two-Photon Induced Fluorescence*, vol. 5, ed. J. R. Lakowicz (New York: Plenum Press, 1997), 1-

M. Callow, A. Jennings, A. B. Brennan, C. Seegert, A. Gibson, L. Wilson, A. Feinberg, R. Baney, and J. Callow," *Biofouling* 18 (2002): 229-236.

R. T. Carson, E. Larson, S. B. Levy, B. M. Marshall, and A. E. Aiello, "Use of Antibacterial Consumer Products Containing Quaternary Ammonium Compounds and Drug Resistance in the Community," *Journal of Antimicrobial Therapy* (2008): 1160-1162.

G. Cheng, H. Xue, Z. Zhang, S. Chen, S. Jiang, "A Switchable Biocompatible Polymer Surface with Self-Sterilizing and Nonfouling Capabilities," *Angewandte Chemie International Edition* 47 (2008): 8831-8834.

K. K. Chung, J. F. Schumacher, E. M. Sampson, R. A. Burne, P. J. Antonelli, and A. B. Brennan, "Impact of Engineered Surface Microtopography on Biofilm Formation of Staphylococcus aureus," *Biointerphases* 2, no. 2 (2007): 89-94.

J. L. Connell, A. K. Wessel, M. R. Parsek, A. D. Ellington, M. Whiteley, and J. B. Shear, "Probing Prokaryotic Social Behaviors with Bacterial "Lobster Traps," *mBio* 1, no. 4 (2010): 202-210.

J. W. Costerton, P. S. Stewart, and E. P. Greenberg, "Bacterial Biofilms: A Common Cause of Persistent Infections," *Science* 284: 1318-1322.

D. de Beer, P. Stoodley, F. Roe, and Z. Lewandowski, "Effects of Biofilm Structures on Oxygen Distribution and Mass Transport," *Biotechnology and Bioengineering* 43 (1994): 1131-1138.

C. Díaz, P. L. Schilardi, R. C. Salvarezza, and M. F. L. de Mele, "Nano/Microscale Order Affects the Early Stages of Biofilm Formation on Metal Surfaces," *Langmuir* 23 (2007): 11206-11210.

G. Drews, "The Roots of Microbiology and the Influence of Ferdinand Cohn on Microbiology of the 19th Century," *FEMS Microbiology Reviews* 24 (2000): 225-249.

T. S. J. Elliott, H. A. Moss, S. E. Tebbs, I. C. Wilson, R. S. Bosner, T. R. Graham, L. P. Burke, and M. H. Faroqui, "Novel Approach to Investigate a Source of Microbial Contamination of Central Venous Catheters," *European Journal of Clinical Microbiology and Infectious Diseases* 16 (1997): 210-213.

S. H. Flint, J. D. Brooks, and P. J. Bremer, "Properties of the Stainless Steel Substrate, Influencing the Adhesion of Thermo-Resistant Streptococci," *Journal of Food Engineering* 43 (2000): 235-242.

F. Furno, K. S. Morley, B. Wong, B. L. Sharp, P. L. Arnold, S. M. Howdle, R. Bayston, P. D. Brown, P. D. Winship,, and H. J. Reid, "Silver Nanoparticles and Polymeric Devices: A New Approach to Prevention of Infection?" *Journal of Antimicrobial Therapy* 54 (2004): 1019-1024.

M. Göppert-Mayer 1931, "Über Elementarakte mit zwei Quantensprüngen," *Annalen der Physik* 9 (1995): 273-295.

C. Gradmann, "Heinrich Hermann Robert Koch," *Encyclopedia of Life Sciences,* John Wiley & Sons (2001).

C. Haefeli, C. Franklin, and K. Hardy, "Plasmid-Determined Silver Resistance in Pseudomonas stutzeri Isolated from a Silver Mine," *Journal of Bacteriology* 158, no. 1 (1984): 389-392.

L. Hall-Stoodley, J. W. Costeron, and P. Stoodley, "Bacterial Biofilms: From the Natural Environment to Infectious Diseases," *Nature Reviews* 2 (2004): 95-108.

R. E. W. Hancock, "Cationic Peptides: Effectors in Innate Immunity and Novel Antimicrobials," Lancet 1 (2001): 156-164.

R. E. W. Hancock and H. Sahl, "Antimicrobial and Host Defense Peptides as New Anti-Infective Therapeutic Strategies," *Nature Biotechnology* 24, no. 12 (2006): 1551-1557.

R. M. Harshey, "Bacterial Motility on a Surface: Many Ways to a Common Goal," *Annual Reviews of Microbiology* 57 (2003): 249-273.

A. T. Heinrici, "Studies of Freshwater Bacteria: I. A Direct Microscopic Technique," *Journal of Bacteriology* 25 (1933): 277-286.

E. M. Hetrick and M. H. Schoenfisch, "Reducing Implant-Related Infections: Active Release Strategies," *Chemical Society Reviews* 35 (2006): 780-789.

R. T. Hill and J. B. Shear, "Enzyme-Nanoparticle Functionalization of Three-Dimensional Protein Scaffolds," *Analytical Chemistry* 78, 19 (2006): 7022-7026.

A. I. Hochbaum and J. Aizenberg, "Bacteria Pattern Spontaneously on Periodic Nanostructure Arrays," *Nano Letters* 10 (2010): 3717-3721.

R. C. Hunter and T. J. Beveridge, "High-Resolution Visualization of Pseudomonas aeruginosa PAO1 Biofilms by Freeze-Substitution Transmission Electron Microscopy," *Journal of Bacteriology* 187, no. 22 (2005): 7619-7630.

B. Kaehr, R. Allen, D. J. Javier, J. Currie, and J. B. Shear, "Guiding Neuronal Development with in situ Microfabrication," *Proceedings of the National Academy of Sciences* 101, no. 46 (2004): 16104-16108.

B. Kaehr and J. B. Shear, "Mask-Directed Multiphoton Lithography," *Journal of the American Chemical Society* 129 (2007): 1904-1905.

B. Kaehr, *Defining Cellular Microenvironments using Multiphoton Lithography*, (The University of Texas at Austin, 2007): 130-140.

B. Kaehr and J. B. Shear, "Multiphoton Fabrication of Chemically Responsive Protein Hydrogels for Microactuation," *Proceedings of the National Academy of Sciences* 105, no. 26 (2008): 8850-8854.

B. Kaehr and J. B. Shear, "High-Throughput Design of Microfluidics Based on Directed Bacterial Motility," *Lab on a Chip* 9 (2009): 2632-2637.

D. Kaiser, "Bacterial Motility: How Do Pili Pull?" *Current Biology* 10, no. 21 (2000): 777-780.

E. Kenawy, S. D. Worley, and R. Broughton, "The Chemistry and Application of Antimicrobial Polymers: A State-of-the-Art Review," *Biomacromolecules* 8, no. 5 (2007): 1359-1384.

M. Klausen, A. Heydorn, P. Ragas, L. Lambertsen, A. Aaes-Jørgensen, S. Molin, and T. Tolker-Nielsen, "Biofilm Formation by Pseudomonas aeruginosa Wild Type, Flagella and Type IV Pili Mutants," *Molecular Microbiology* 48, no. 6 (2003): 1511-1524.

M. Klausen, A. Aeas-Jøregensen, S. Molin, and T. Tolker-Nielsen, "Involvement of Bacterial Migration in the Development of Complex Multicellular Structures in Pseudomonas aeruginosa Biofilms," *Molecular Microbiology* 50, no. 1 (2003): 61-68.

R. Kügler, O. Bouloussa, and F. Rondelez, "Evidence of a Charge-Density Threshold for Optimum Efficiency of Biocidal Cationic Surfaces," *Microbiology* 151 (2005): 1341-1348.

R. Kumar and H. Münstedt, "Silver Ion Release from Antimicrobial Polyamide/Silver Composites," *Biomaterials* 26 (2005): 2081-2088.

C. N. LaFratta, J. T. Fourkas, T. Baldacchini, and R. A. Farrar, "Multiphoton Fabrication," *Angewandte Chemie International Edition* 46 (2007): 6238-6258.

J. Lam, R. Chan, K. Lam, and J. W. Costerton, "Production of Mucoid Microcolonies by Pseudomonas aeruginosa within Infected Lungs in Cystic Fibrosis," *Infection and Immunity* 28, no. 2 (1980): 546-556.

K. Lewis, "Persistor Cells, Dormancy and Infectious Disease," *Nature Reviews* 5 (2007): 48-56.

J. L. Lyon, R. T. Hill, J. B. Shear, and K. J. Stevenson, "Direct Electrochemical and Spectroscopic Assessment of Heme Integrity in Multiphoton Photo-Cross-Linked Cytochrome c Structures," *Analytical Chemistry* 79 (2007): 2303-2311.

L. Ma, M. Conover, H. Lu, M. R. Parsek, K. Bayles, and D. J. Wozniak, "Assembly and Development of the Pseudomonas aerugionsa Biofilm Matrix," *PLoS Pathogens* 5, issue 3 (2009): 1-11.

T. C. Mah and G. A. O'Toole, "Mechanisms of Biofilm Resistance to Antimicrobial Agents," *Trends in Microbiology* 9, no. 1 (2001): 34-39.

S. M. Marxer, A. R. Rothrock, B. J. Nablo, M. E. Robbins, and M. H. Schoenfisch, "Preparation of Nitric Oxide (NO)-Releasing Sol-Gels for Biomaterial Applications," *Chemistry of Materials* 15 (2003): 4193-4199.

J. S. Mattick, "Type IV Pili and Twitching Motility," *Annual Reviews of Microbiology* 56 (2002): 289-314.

A. J. Merz, M. So, and M. P. Sheetz, "Pilus Retraction Powers Bacterial Twitching Motility," *Nature* 407 (2000): 98-102.

N. Mitik-Dineva, J. Wang, V. K. Truong, P. Stoddart, F. Malherbe, R. J. Crawford, and E. P. Ivanova, "Esherichia coli, Pseudomonas aeruginosa, and Staphylococcus aureus Attachment Patterns on Glass Surfaces with Nanoscale Roughness," *Current Microbiology* 58 (2009): 268-273.

R. Nielson, B. Kaehr, and J. B. Shear, "Microreplication and Design of Biological Architectures using Dynamic-Mask Multiphoton Lithography," *Small* 5, no. 1 (2008): 120-125.

G. A. O'Toole and R. Kolter, "Flagellar and Twitching Motility are Necessary for Pseudomonas aeruginosa Biofilm Development," *Molecular Microbiology* 30, no. 2 (1998): 295-304.

S. Park, P. M. Wolanin, E. A. Yuzbashyan, P. Silberzan, J. B. Stock, and R. H. Austin, "Motion to Form a Quorum," *Science* 301 (2003): 188.

M. R. Parsek and T. Tolker-Nielsen, "Pattern Formation in Pseudomonas aerugionsa Biofilms," *Current Opinion in Microbiology* 11 (2008): 560-566.

S. Petronis, K. Berntsson, J. Gold, and P. Gatenholm, "Design and Microstructuring of PDMS Surfaces for Improved Marine Biofouling Resistance," *Journal of Biomaterials Science, Polymer Edition* 11, no. 10 (2000): 1051-1072.

S. D. Puckett, E. Taylor, T. Raimondo, and T. J. Webster, "The Relationship Between the Nanostructure of Titanium Surfaces and Bacterial Attachment," *Biomaterials* 31 (2010): 706-713.

M. Rai, A. Yadav, and A. Gade, "Silver Nanoparticles as a New Generation of Antimicrobials," *Biotechnology Advances* 27 (2009): 76-83.

P. Ramritu, K. Halton, P. Collignon, D. Cook, D. Fraenkel, D. Battistutta, M. Whitby, and N. Graves, "A Systematic Review Comparing the Relative Effectiveness of Antimicrobial-Catheters in Intensive Care Units," *American Journal of Infection Control* 36, no. 2 (2008): 104-117.

M. M. Ramsey and M. Whiteley, "Pseudomonas aeruginosa Attachment and Biofilm Development in Dynamic Environments," *Molecular Microbiology* 53, no. 4 (2004): 1075-1087.

E. T. Ritschdorff, M. L. Plenert, and J. B. Shear, "Microsecond Analysis of Transient Molecules using Bi-Directional Capillary Electrophoresis," *Analytical Chemistry* 81, 21 (2009): 8790-8796.

E. T. Ritschdorff and J. B. Shear, "Multiphoton Lithography using a High-Repetition Rate Microchip Laser," *Analytical Chemistry* 82 (2010: 8733-8737.

L. Rizzello, B. Sorce, S. Sabella, G. Vecchio, A. Galeone, V. Brunetti, R. Cingolani, and P. P. Pompa, "Impact of Nanoscale Topography on Genomics and Proteomics of Adherent Bacteria," *ACS Nano* 5, no 3 (2011): 1865-1876.

J. M. Schumacher, C. J. Long, M. E. Callow, J. A. Finlay, J. A. Callow, and A. B. Brennan, "Engineered Nanoforce Gradients for Inhibition of Settlement (Attachment) of Swimming Algal Spores," *Langmuir* 24 (2008): 4931-4937.

M. Schwartz, "The Life and Works of Louis Pasteur," *Journal of Applied Microbiology* 91 (2001): 597-601.

S. K. Seidlits, C. E. Schmidt, and J. B. Shear, "High-Resolution Patterning of Hydrogels in Three Dimensions using Direct-Write Photofabrication for Cell Guidance," *Advanced Functional Materials* 19 (2009): 3543-3551.

A. B. T. Semmler, C. B. Whitchurch, and J. S. Mattick, "A Re-Examination of Twitching Motility in Pseudomonas aerugionsa," *Microbiology* 145 (1999): 2863-2873.

J. B. Shear, "Multiphoton-Excited Fluorescence in Bioanalytical Chemistry," *Analytical Chemistry* 71, no. 17 (1999): 598A-605A.

P. K. Singh, A. L. Schaefer, M. R. Parsek, T. O. Moninger, M. J. Walsh, and E. P. Greenberg, "Quorum-Sensing Signals Indicate that Cystic Fibrosis Lungs are Infected with Bacterial Biofilms," *Nature* 407 (2000): 762-764.

J. D. Spikes, H. Shen, P. Kopecková, and J. Kopecek, "Photodynamic Crosslinking of Proteins. III. Kinectics of the FMN- and Rose Bengal-Sensitized Photooxidation and Intermolecular Crosslinking of Model Tyrosine-Containing N-(2-Hydroxypropyl)methacrylamide Copolymers," *Photochemistry and Photobiology* 70, 2 (1999): 130-137.

P. Stoodley, K. Sauer, D. G. Davies, and J. W. Costerton, "Biofilms as Complex Differentiated Communities," *The Annual Review of Microbiology* 56 (2002): 187-209.

H. Sun and S. Kawata, "Two-Photon Photopolymerization and 3D Lithographic Microfabrication," *Advances in Polymer Science* 170 (2004): 169-273.

T. Sun, L. Feng, X. Gao, and L. Jiang, "Bioinspired Surfaces with Special Wettability," *Accounts of Chemical* Research 38 (2005): 644-652.

R. L. Taylor, J. Verran, G. C. Lees, and A. J. P. Ward, "The Influence of Substratum Topography on Bacterial Adhesion to Polymethyl Methacrylate," *Journal of Materials Science: Materials in Medicine* 9 (1998): 17-22.

S. E. Tebbs, A. Sawyer, T. S. J. Elliott, M. R. C. Path, "Influence of Surface Morphology on In Vitro Bacterial Adherence to Central Venous Catheters," *British Journal of Anesthesia* 72, no 5 (1994): 587-591.

J. C. Tiller, C. Liao, K. Lewis, and A. M. Klibanov, "Designing Surfaces that Kill Bacteria on Contact," *Proceedings of the National Academy of Sciences* 98, no 11 (5981-5985).

K. Vasilev, J. Cook, and H. J. Greisser, "Antibacterial Surfaces for Biomedical Devices," *Expert Reviews of Medical Devices* 6, no. 5 (2009): 553-567.

W. Vongpatanasin, L. D. Hillis, and R. A. Lange, "Prosthetic Heart Valves," *The New England Journal of Medicine* 335, no. 6 (1996): 407-416.

J. M. Vroom, K. J. DeGrauw, H. C. Gerritsen, D. J. Bradshaw, P. D. Marsh, G. K. Watson, J. J. Birmingham, and C. Allison, "Depth Penetration and Detection of pH Gradients in Biofilms by Two-Photon Excitation Microscopy," *Applied and Environmental Microbiology* 65, no. 8 (1999): 3502-3511.

D. Wall and D. Kaiser, "Type IV Pili and Cell Motility," *Molecular Microbiology* 32, no. 1 (1999): 1-10.

D. Wall and D. Kaiser, "Alignment Enhances the Cell-to-Cell Transfer of Pilus Phenotype," *Proceedings of the National Academy of Sciences* 95 (1998): 3054-3058

R. A. Weiss, "The Leeuwenhoek Lecture 2001. Animal Origins of Human Infectious Disease," Philosophical Transactions: *Biological Sciences* 356, no. 1410, Origins of HIV and the AIDS Epidemic (2001): 955 + 957-977.

J. M. Willey, L. M. Sherwood, and C. J. Woolverton, *Microbiology*, 7th edition (New York: McGraw-Hill, 2008), 66-67.

P. Wu and D. W. Grainger, "Drug/Device Combinations for Local Drug Therapies and Infection Prophylaxis," *Biomaterials* 27 (2006): 2450-2467.

C. Xu and W. W. Webb, "Multiphoton Excitation of Molecular Fluorophores and Nonlinear Laser Microscopy," in *Topics in Fluorescence Spectroscopy: Nonlinear and Two-Photon Induced Fluorescence*, vol. 5, ed. J. R. Lakowicz (New York: Plenum Press, 1997), 471-540.

M. Zilberman and J. J. Elsner, "Antibiotic-Eluting Medical Devices for Various Applications," *Journal of Controlled Release* 130 (2008): 202-215.

W. R. Zipfel, R. M. Williams, and W. W. Webb, "Nonlinear Magic: Multiphoton Microscopy in the Biosciences," *Nature Biotechnology* 21, no. 11 (2003): 1369-1377

"Technology" *Sharklet Technologies, Inc*. published 2010. retrieved April 4, 2011. http://www.sharklet.com/technology/.